THE UNIVERSITY OF CALGARY

OPTICAL FIBRE CIRCUIT SWITCHING USING GLASS THERMO-OPTIC BULK DEFLECTOR

by

Anjali Agarwal

A THESIS

SUBMITTED TO THE FACULTY OF GRADUATE STUDIES

IN PARTIAL FULFILLMENT OF THE REQUIREMENTS FOR THE

DEGREE OF MASTER OF SCIENCE

DEPARTMENT OF ELECTRICAL ENGINEERING

CALGARY, ALBERTA

JUNE, 1986

ISBN 0-315-32670-0

THE UNIVERSITY OF CALGARY

FACULTY OF GRADUATE STUDIES

The undersigned certify that they have read, and recommended to the Faculty of Graduate Studies for acceptance, a thesis entitled, "*Optical Fibre Circuit Switching using Glass Thermo-optic Bulk Deflector*" submitted by Anjali Agarwal in partial fulfillment of the requirements for the degree of Master of Science.

David Irvine - Halliday

Dr. D. Irvine-Halliday - Chairman
Department of Electrical Engineering

Ronald H. Johnston

Dr. R.H. Johnston
Department of Electrical Engineering

B. Nowrouzian

Dr. B. Nowrouzian
Department of Electrical Engineering

Richard D. Rowe

Dr. R.D. Rowe
Department of Mechanical Engineering

Date: 3 July 86

ABSTRACT

The thermo-optic effect originating from the temperature dependence of the refractive index has been utilised to obtain light beam deflection and switching in glass. One-dimensional 1×2 thermo-optic bulk deflector devices have been successfully fabricated and tested. Thermally induced index changes are effected by applying an appropriate voltage to a small film heater deposited on the glass surface.

The optical fibre circuit switch is discussed experimentally and theoretically. Four Schott glasses are considered for optical switching and their performances are evaluated in terms of light beam deflection and transient response. The results for the deflection angle and the switch response times are presented. The theoretical analysis of the physical property temperature gradient of the glass is reported to correspond very closely with the optical behaviour of the switch in terms of its deflection angle and transient response.

A two-dimensional 1×4 thermo-optic device utilising the optical isotropy of glass, achieving enhanced switching capabilities, has also been successfully fabricated and tested.

ACKNOWLEDGEMENTS

It is my great pleasure to express sincere gratitude to others who have contributed immensely to the successful completion of this work.

I have a deep feeling of indebtness to my Supervisor, Dr. Dave Irvine-Halliday for his constant confidence, support, encouragement and guidance. His suggestions and criticisms from time to time are appreciated, and more importantly, his invaluable friendship will never be forgotten.

I am indebted to Garry Harrington for his invaluable technical assistance in preparing the experimental equipment.

Many thanks are due to all my friends to help establish a convivial environment in which to work and to provide the needed moral support during the difficult stages of this work.

The financial assistance received from the Department of Electrical Engineering in the form of graduate assistantships is greatly acknowledged.

Finally, I thank Ambrish, my husband, to whom I owe much for his unending patience, encouragement, guidance and understanding without which I could hardly have completed this work.

To my parents

TABLE OF CONTENTS

LIST OF TABLES

LIST OF FIGURES

LIST OF SYMBOLS

A	cross sectional area
A_l	amplitude of light
b	laser beam width
c	specific heat of material
CRO	cathode ray oscilloscope
d	maximum deflection
$\frac{dn}{dT}$	temperature coefficient of refractive index
$\frac{dn}{dx}$	refractive index gradient
$\frac{dn[T(x)]}{dx}$	refractive index gradient due to the thermo-optic effect
$\frac{dT}{dx}$	temperature gradient in x-direction
$\frac{dT}{dy}$	temperature gradient in y-direction
$\frac{d\theta_D}{dP_H}$	figure of merit
E/O	electrical to optical
ER	extinction ratio
h	convection heat-transfer coefficient
h_V	heat-transfer coefficient for a vertical boundary
h_H	heat-transfer coefficient for a horizontal boundary
h_{Hh}	heat-transfer coefficient for a heated horizontal surface
h_{Hc}	heat-transfer coefficient for a cooled horizontal surface
J_1	first order Bessel function
k	thermal conductivity

K_{Al}	coefficient which takes care of conduction in aluminium
l_g	glass length
L	mean of the two dimensions for a rectangular surface
L_h	horizontal dimension of the rectangular surface
L_v	vertical dimension of the rectangular surface
m,n	node location indicating the y and x increments respectively
n	refractive index
$n(x)$	refractive index as a function of x-ordinate
n_{air}	refractive index of air
O/E	optical to electrical
P	centre of the diffraction pattern with a linear refractive index gradient in the glass
P_H	heater power
Q	centre of the diffraction pattern with a uniform refractive index in the glass
q	heat-transfer rate (heater power)
q''	surface heat flux (heater power density)
s	distance at which the fibre is placed at the output end
TO	thermo-optic
T	temperature
T_∞	temperature of air
$T^p_{m,n}$	temperature at any particular time at node m,n
$T^{p+1}_{m,n}$	temperature after a time increment Δt at node m,n
t_r	rise time
t_d	delay time
t_f	fall time
V	voltage applied to the heater

x_d	deflection in the x-axis
α	thermal diffusivity
δ	phase difference
Δn	change in refractive index
Δn_E	refractive index change due to electro-optic effect
Δn_T	refractive index change due to thermo-optic effect
Δn_e	refractive index change for the extraordinary wave
Δn_o	refractive index change for the ordinary wave
$\Delta n_{relative}$	refractive index change relative to standard air
Δt	time increment
Δx	space increment in x-axis
Δy	space increment in y-axis
ΔT	temperature difference between surface and surroundings
θ	angle between the light ray and the horizontal plane in air
θ_0	entrance angle between the light ray and the horizontal plane in air
θ_{l_g}	exit angle between the light ray and the horizontal plane in air
θ_D	deflection angle
θ_s	beam spread angle
λ	wavelength
ρ	density
ρc	thermal heat capacity
ϕ	angle between the light ray and the horizontal plane in glass
$\phi(x)$	angle between the light ray and the horizontal plane as a function of x-ordinate
ϕ_0	entrance angle between the light ray and the horizontal plane in glass
ϕ_{l_g}	exit angle between the light ray and the horizontal plane in glass

1-D	one-dimensional
2-D	two-dimensional
$1 \times n$	1 input and n outputs

CHAPTER 1

INTRODUCTION

In recent years, optical fibre technology, with all its major features and benefits, has developed to an extent where it is definitely a prime candidate for replacing both coaxial cable and twisted wire pairs. The growing interest in optical fibre communications system as well as the prospect of fabricating efficient inexpensive devices have stimulated activity in integrated optics. The importance of modulators, switches and deflectors for these applications has led to the investigations of methods for their production. To a certain extent, optical switching has predated the advent of optical communications systems because optical switching techniques developed in parallel with the development of the laser. An optical switch is defined as a device for diverting the flow of power from one optical waveguide to any one of a number of adjacent optical waveguides.

1.1. Basic Optical Switching Techniques

Although there are variations in each category, there are three basic methods by which optical signals may be switched from one optical channel to another [1].

(1) **Mechanical Switching.** This is the simplest and perhaps the least useful method. Examples include the mechanical movement of a fibre or optical lens. A beam-diverting mirror, prism, or other mechanical device may be

physically placed in the path of the beam to be deflected. The presence of moving parts implies that switching speeds are very slow and that reliability may be a concern. This method of switching, therefore, has limited applications.

(2) **Electrical Switching.** In this method of switching the optical signal has to be first converted into an electrical signal. The optical/electrical transformation may be carried out by a p-intrinsic-n (PIN) diode or avalanche photodiode (APD). The electrical signal can then be switched by transistor to another communications channel. The switched electrical signal then modulates another laser to reconvert it into an optical signal. This switching option may be viable but will probably not remain competitive if efficient methods of switching light itself are developed since with O/E and E/O conversions, the optical signal frequency is limited by the electric circuit high-frequency cut off.

(3) **Optical Switching.** Switches that utilise the deflection of the optical power itself represent the third basic type of optical waveguide switch. In systems using such switches, conversion of optical power to electrical power or vice versa is accomplished only at the system input and output. An optical switch can be formed by using techniques for deflecting a narrow beam where a gradient of refractive index should exist in the propagation media perpendicular to the wavefront normal, or by using the principle of total internal reflection when the light beam is incident at an angle less than the

complimentary critical angle formed due to the differences in the refractive index of the adjacent layers of the material used for the switch. In both of the above cases, the effectiveness of switching depends on the refractive index n, and the change in refractive index Δn.

An optical fibre communication system using an electrical switch and an optical switch is shown in Figure 1.1. An electrical switch has a greater volume and size and uses a larger number of components than an optical switch.

1.2. Classification of Optical Switches

Optical switches are classified on the basis of the methods used for inducing the change of refractive index, Δn, in the material used for the switch. They are:

(1) **Electro-optic:** The refractive index of the medium is changed anisotropically by applying an electric field across an optical medium [2-4].

(2) **Magneto-optic:** The presence of magnetic fields may also effect the optical properties of some substances by changing the refractive index of the material [5-7]. In general, however, as electric fields are easier to generate than magnetic fields, electro-optic devices are usually preferred to magneto-optic devices.

(3) **Acousto-optic:** It is the change in the refractive index of a medium caused by the mechanical strains accompanying the passage of an acoustic (strain) wave through the medium [8].

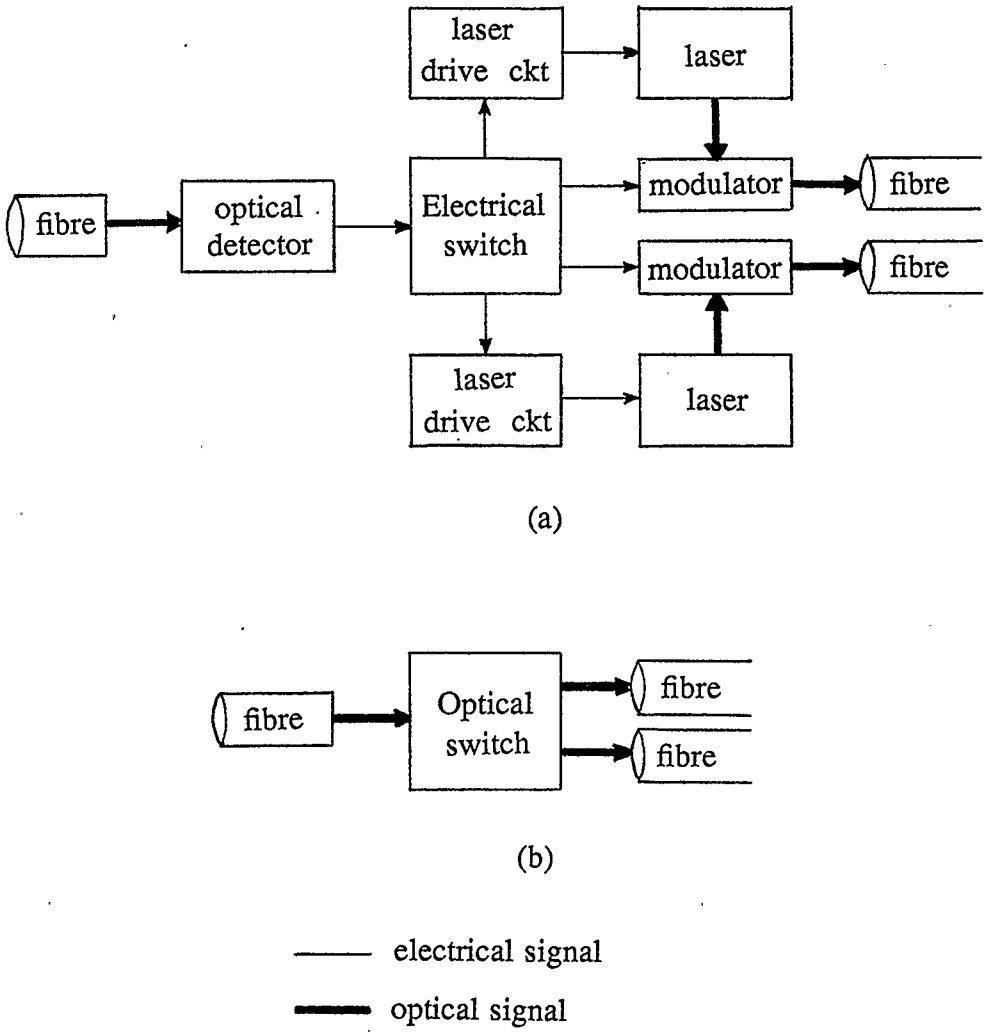

Figure 1.1 Optical Fibre Communication System using

(a) an electrical switch

(b) an optical switch

(4) **Thermo-optic:** The refractive index of the medium is changed by varying the temperature of the medium [9-11].

The electro-optic effect is shown only by piezo-electric crystals, such as $NaClO_3$, quartz, ammonium dihydrogen phosphate (ADP), $LiNbO_3$, potassium dihydrogen phosphate (KDP) and Rochelle salt, and that too only for some specific orientations. This effect may introduce new optic axes into naturally doubly refracting crystals, or make naturally isotropic crystals doubly refracting. To be useful, however, such crystals must have a sizable electro-optic coefficient and be available in reasonably sized, good quality crystals at modest cost. KDP and ADP are available in large sizes at relatively low cost but are soluble in water and fragile. Other favoured materials such as lithium tantalate and lithium niobate ($LiTaO_3$ and $LiNbO_3$) have relatively much larger linear electro-optic coefficients but reasonably sized crystals are rather expensive [12]. The largest electro-optic coefficient is observed when the field is applied parallel and the wave normal is perpendicular to the optic axis [13]. For small angular variations between the wave normal and optic axis, the effective voltage for switching increases rapidly [14]. The maximum value of the index change Δn_E for $LiNbO_3$ due to the electro-optic effect is 1.6×10^{-3}, determined by the breakdown electric field of 10 $V/\mu m^2$ [9]. In electro-optic devices, the temperature dependence of the refractive index is, in general, an undesirable property for the stable device operation. The temperature-dependent index change Δn_T of $LiNbO_3$, however, is expected to be at least 3×10^{-3} when the crystal temperature changes from room temperature to

100^oC [15]. This amount of Δn_T is found to be large enough to control the light beam, and efficient light deflection can be performed. The deflection characteristics are, however, strongly dependent on the polarisation of the incident beam. The deflection angle for the extraordinary wave is much larger than that for the ordinary wave, due to the fact that Δn_e is greater than Δn_o for $LiNbO_3$ [9]. The thermo-optic effect can also be found in other dielectric materials possessing a temperature dependent refractive index, and for example in glass, Δn_T can be approximately 10^{-3} for a temperature rise of 100^oC [16]. The TO effect, therefore, makes it possible to realise active optical devices in glass such as deflectors and modulators/switches. The light deflection characteristics are independent of the polarization of the incident beam because of the optical isotropy of glass [10]. This feature makes glass suitable for use with fibre optic transmission lines which feeds into the switch an optical beam with unpredictably fluctuating polarization.

1.3. Objective of the Thesis

Since glass is an important and widely used material in fibre optics, and is inexpensive and readily available, the main objectives of this thesis are

(1) to obtain light deflection and switching using the thermo-optic effect originating from the temperature dependence of the refractive index of glass, and

(2) to relate the physical properties of the glass samples with their optical properties.

The performance of the four commercial glass samples chosen from the Schott catalog [17] and shown in Table 1.1 with their temperature coefficients of refractive index, are investigated. Figure 1.2 gives the change in refractive index Δn with respect to the temperature for these glasses.

1.4. Outline of the Thesis

In order to accomplish the objectives of the thesis, the following work is performed:

(1) The behaviour of the light beam is examined when a linear refractive index gradient exists in the propagation media, the glass. Fraunhofer diffraction effects due to the finite width of the input laser beam are also studied. To examine the physical properties of the glass samples the two-dimensional equations of heat conduction, using numerical method of analysis based on finite difference techniques, are analysed [Chapter 2].

(2) The device structures for 1-dimensional 1×2, and 2-dimensional 1×4 TO bulk deflectors are fabricated. The glass samples are prepared by vacuum deposition of heating strips on the upper surface. The experimental setup for determining the optical properties of the glass samples is developed [Chapter 3].

(3) The performance of the Schott glass samples considered in this thesis are investigated with respect to the refractive index gradient due to the thermo-optic effect, Fraunhofer diffraction effect, and the physical properties for

[^oC]	Relative dn/dT [$10^{-6}/K$] Schott glass name			
	SF13	SF11	SF57	SF59
0/20	--	11.1	--	11.7
20/40	7.9	11.3	10.9	12.1
40/60	8.1	11.6	11.0	12.6
60/80	8.3	11.8	11.2	12.9

Table 1.1 Temperature coefficients of refractive index of the four Schott glasses at $\lambda = 643.8$nm

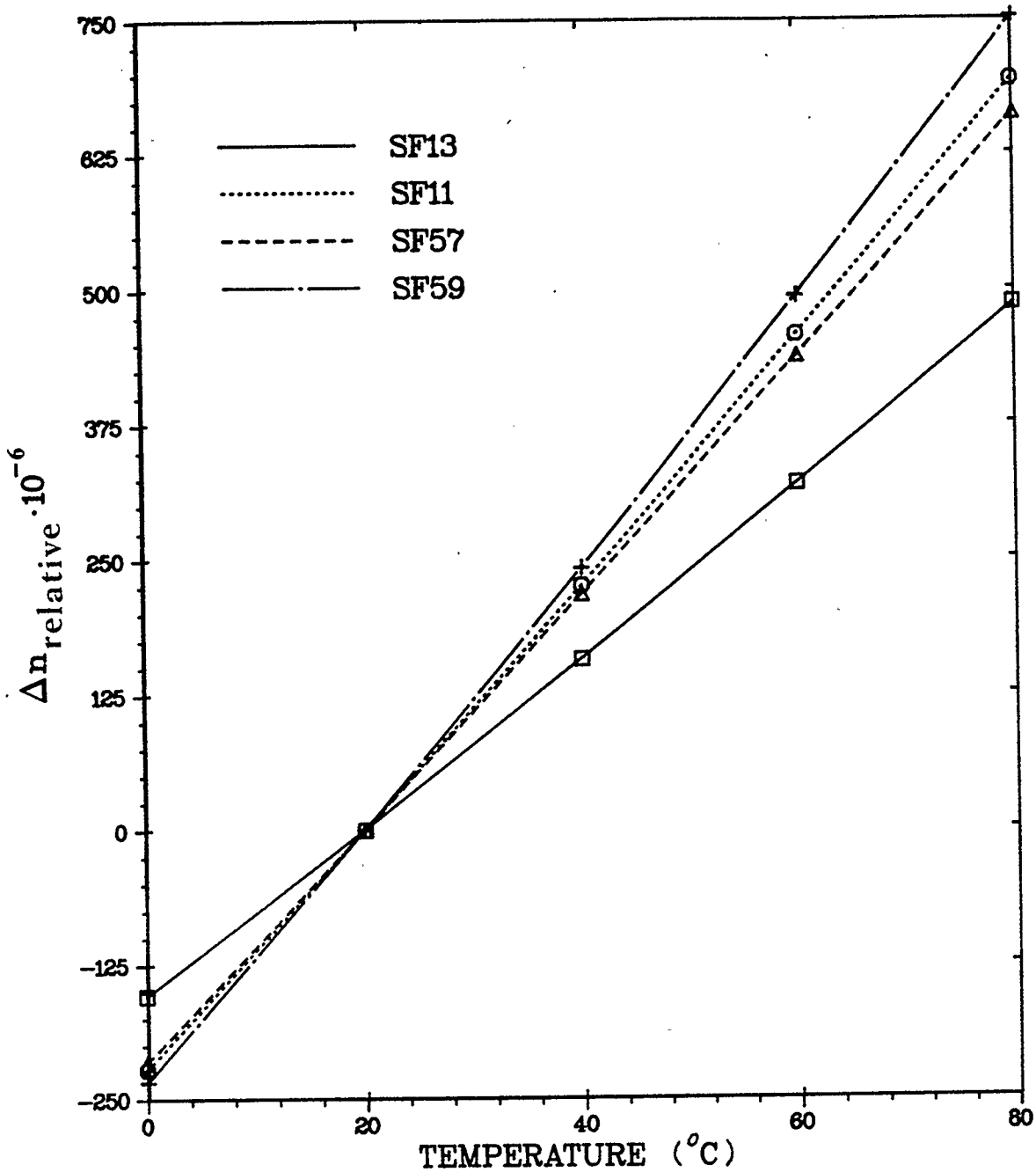

FIGURE 1.2 CHANGE IN REFRACTIVE INDEX

Δn vs TEMPERATURE

different heater powers applied on the surface of the samples [Chapter 4].

(4) The optical properties of the glass samples are investigated with respect to the deflection of the input laser beam, extinction ratios in the output power and transient response of the switch for different heater powers. The switching pattern of a 2-dimensional 1×4 TO bulk deflector is also obtained [Chapter 5].

CHAPTER 2

THEORY

2.1. Introduction

The basic refraction phenomenon, refraction by an index gradient, has been employed in light deflection for this study. In the present chapter, the optical theory of this light refraction phenomenon is briefly reviewed. Fraunhofer diffraction effects due to the wave nature of light, that are ignored in geometric optics, are examined. The thermo-optic effect originating from the temperature dependence of the refractive index is considered. A gradient of refractive index normal to the incident beam is obtained when the temperature gradient normal to the incident beam is present. The analysis of the temperature gradient is done by solving the two-dimensional heat flow equation when an appropriate power is applied to a film heater on the glass surface.

2.2. Optical Theory

The effect of gradient upon a plane wavefront is illustrated in Figure 2.1 [18]. A plane wavefront of light incident normally on a medium of uniform refractive index is not refracted. The form of wavefront, and the path of light, that is, the direction of energy transfer by the wavefront are unaffected by passage through a homogeneous medium of constant thickness. If, however, an index gradient exists

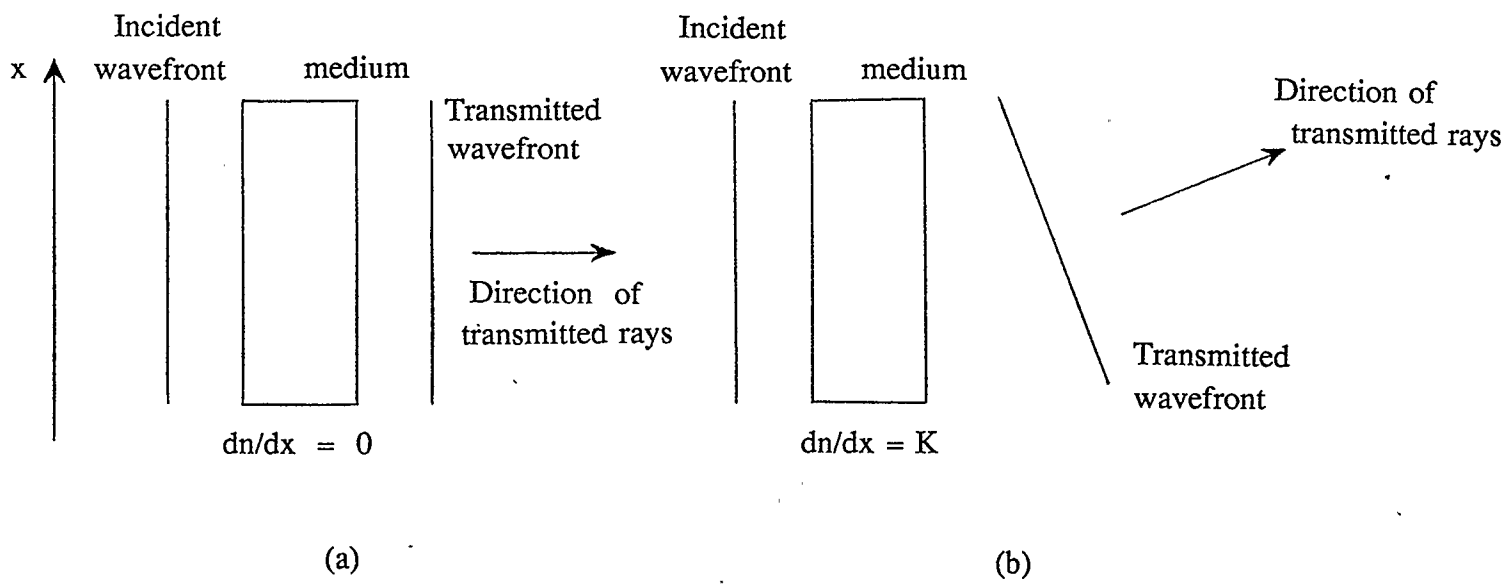

Figure 2.1 Transmission of a plane wavefront :

(a) by a uniform medium,

(b) by a refractive index gradient

with respect to the x-direction, the axis perpendicular to the light beam as shown in Figure 2.1, each portion of the wavefront is transmitted through the medium with a different velocity. If the refractive index gradient is uniform, a uniformly inclined wavefront is produced. Since the refractive index is inversely proportional to the velocity of transmission, the wavefront is most retarded by the region of highest refractive index. The direction of the light beam is that of the normal to the wavefront, thus the light transmitted through a medium with an index gradient is refracted towards the direction of highest refractive index.

The optical inhomogeneity of the medium, glass, is restricted to the vertical direction, that is, the gradient of the refractive index is a function of x-ordinate only. The refractive index is denoted with $n(x)$ and the gradient of refractive index due to the thermo-optic effect as $\frac{dn[T(x)]}{dx}$ with $n(x)$ increasing in the direction of increasing (positive) values of x.

The degree of refraction of the incident light beam in a medium is governed by Snell's law. The angle ϕ subtended between the light ray and the horizontal plane as shown in Figure 2.2, and the refractive index of the medium are related by

$$n \cos\phi = constant \tag{2.1}$$

for each Δx of the medium traversed. When the refractive index of the medium changes continuously in the direction normal to the wavefront, Equation (2.1) may be written as

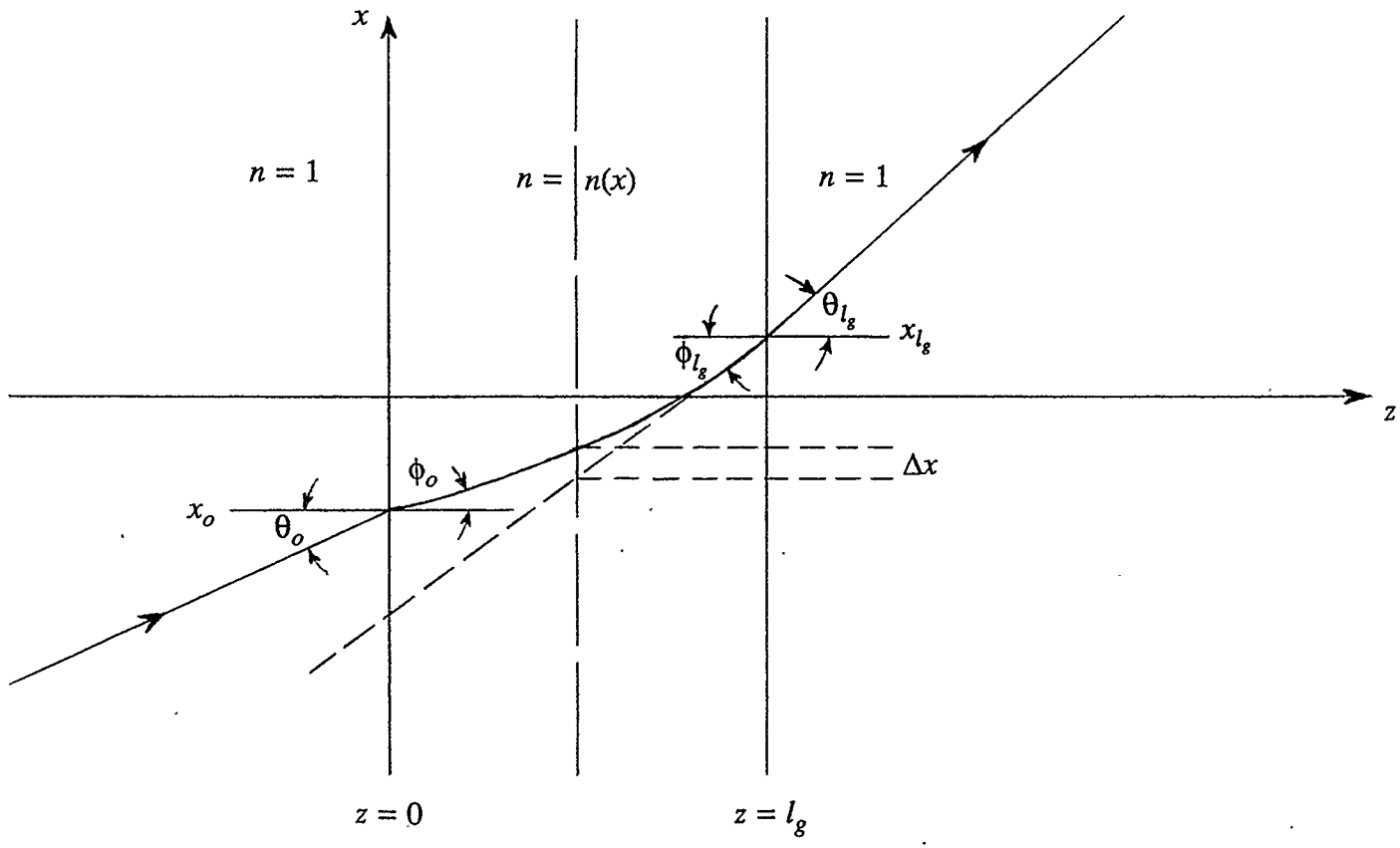

Figure 2.2 Refraction of light due to the presence of refractive index gradient in a medium

$$n(x)\cos\phi(x) = constant \tag{2.2}$$

The incident light path is coincident with the horizontal optical axis (z-axis). The length of the medium ranges from z = 0 to z = l_g, where l_g is the glass length.

Equation (2.2) is differentiated with respect to z to give

$$n(-sin\phi)\frac{d\phi}{dz} + \cos\phi\frac{dn}{dx}\frac{dx}{dz} = 0 \tag{2.3}$$

where the angle ϕ is related to the trajectory of the light ray by

$$\frac{dx}{dz} = \tan\phi \tag{2.4}$$

On combining Equations (2.3) and (2.4)

$$\frac{d\phi}{dz} = \frac{1}{n}\frac{dn}{dx} \tag{2.5}$$

This equation relates the local deflection (deflection within the medium) of the light ray to the gradient of the refraction and the local refractive index of the medium. The total deflection angle in the medium of finite length is obtained by integrating Equation (2.5) within the limits 0 and l_g:

$$\phi_{l_g} - \phi_0 = \int_0^{l_g} \frac{n'(x)}{n(x)}\, dz \tag{2.6}$$

where $n'(x)$ is the refractive index gradient $\frac{dn}{dx}$.

Since both $n'(x)$ and $n(x)$ are unknown functions of z along the trajectory, this integration cannot be carried out by analytical means without simplifying

assumptions. For weak gradients and/or short optical path length, Equation (2.6) can be written simply as [19]

$$\phi_{l_g} - \phi_0 = l_g \frac{n'(x)}{n(x)} \tag{2.7}$$

The refraction of light at the glass boundaries must be considered finally. The angle θ is defined as the angle between the light ray and the horizontal axis in air outside the glass, as shown in Figure 2.2. From Snell's law, the following relation applies at both boundaries:

$$\sin\theta = n \sin\phi \tag{2.8}$$

where $n_{air} \approx 1$

or for small angles

$$\theta = n\phi \tag{2.9}$$

Equation (2.7) can then be written in terms of external entrance and exit angles. Therefore, the overall deflection angle is given by

$$\theta_D = \theta_{l_g} - \theta_0 = l_g n'(x) \tag{2.10}$$

The deflection angle from the glass is thus the product of the glass length and the local value of the refractive index gradient. As can be seen from Equation (2.10), the deflection angle θ_D is maximum when the entrance angle θ_0 is zero, that is, when the incident beam is along the horizontal axis and perpendicular to the direction of the refractive index gradient. Therefore, the deflection angle, θ_D, as

denoted in the following sections is given by

$$\theta_D \simeq l_g \frac{dn[T(x)]}{dx} \tag{2.11}$$

In view of the fundamental importance of Equation (2.10) in the present analysis, it is essential to re-state the assumptions made. The applicability of the equation is subject to the following conditions [19]

(1) The optical path must be sufficiently small so that the beam deflection is small.

(2) The entrance and exit angles should be small enough that the first term of sine expansion is sufficiently accurate.

(3) The absolute refractive index values at the entrance and exit points of a ray are essentially the same.

The first one is the necessary condition. If this condition is satisfied, the remaining two conditions are implicitly satisfied. It has also been assumed in the present analysis that a linear refractive index gradient occurs along the x-axis. However, if the index variation is not linear, the second-order effects of index variation, i.e., $\frac{\partial^2 n}{\partial x^2}$ may cause spreading of the beam of the order $\Delta\theta = l_g \frac{\partial^2 n}{\partial x^2}$.

2.3. Fraunhofer Diffraction Effects

The optical theory in Section (2.2) ignores the diffraction effects due to the wave nature of light. In this section, the diffraction effects when the input laser

beam passes through the glass (a) with a uniform refractive index and (b) with a linear refractive index gradient, are studied.

In Figure 2.3, a collimated light beam AB passes through the circular aperture OO' into the glass with a uniform refractive index, and is imaged onto a screen. The aperture OO' is also the laser beamwidth b. If we consider the plane wavefront at OO', then the wavelets arising from all points on it will produce effects over most of the forward direction. The wavelets reaching point Q as shown in Figure 2.3, have the same path length, that is, $OQ = O'Q$. They, therefore, arrive at Q with the same phase and this point, which is the centre of the diffraction pattern, is thus a maximum and bright. For the point Q' the ray paths OQ' and FQ' are equal as are the paths from all points on the line OF. With the collimated light source, the only wavelets available in phase are along the line OO'. If they are compounded along the line OF there will be an increasing phase difference moving from O to F. This phase difference δ is generated due to the path difference $O'F = O'Q' - OQ'$. The amplitude of light for a circular aperture due to these phase differences is given by [20]

$$A_l = \frac{2J_1(\delta/2)}{(\delta/2)} \tag{2.12}$$

while the intensity is the square of this and J_1 is the first order Bessel function. The function $J_1(\delta/2)$ gives zero values for particular values of $\delta/2$ showing the locations of the minima. The diffraction pattern obtained must be circular and take the form of a bright central disc surrounded by alternate light and dark rings.

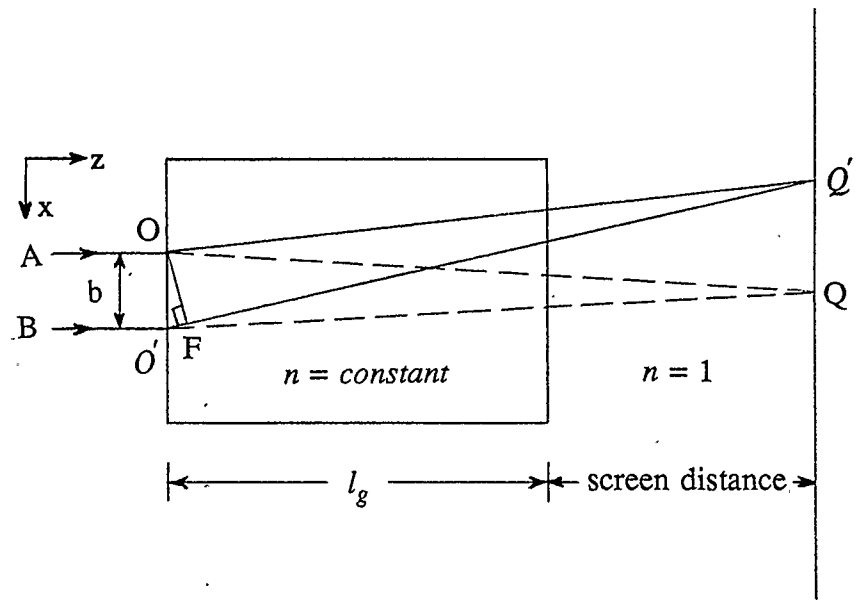

Figure 2.3 Fraunhofer diffraction effects with a uniform refractive index

Figure 2.4 shows the input laser beam passing through the glass with a linear refractive index gradient, the index being maximum at x = 0. Figure 2.4b is an equivalent diagram for Figure 2.4a. The physical length l_g of the glass has been replaced by the optical length ($l_g \times$ refractive index). The optical length decreases as x is increased since the change in refractive index dn is maximum at x = 0. From Figure 2.4b, with

$$O'C = l_g \cdot n_1$$

denoting the optical length, then

$$\begin{aligned} OD &= l_g \cdot n_2 \\ &= l_g(n_1 + b\frac{dn}{dx}) \end{aligned}$$

Now, the wavelets reaching point P have the same path length, that is, $OP = O'P$. Therefore, P is now the centre of the diffraction pattern and has a maximum intensity. The amplitude of light at point P' is not a maximum because a phase difference δ is generated due to the path difference $O'P' - OP'$. The amplitude of light is still given by Equation (2.12).

Figure 2.5 shows the diffraction pattern due to the finite width, b, of the input laser beam. The beam spread angle θ_s is given by

$$\theta_s = 1.27\frac{\lambda}{b} \tag{2.13}$$

(the factor 1.27 signifies a beam with a Gaussian intensity distribution)

The diameter of the beam at any distance from the aperture depends on θ_s. As the

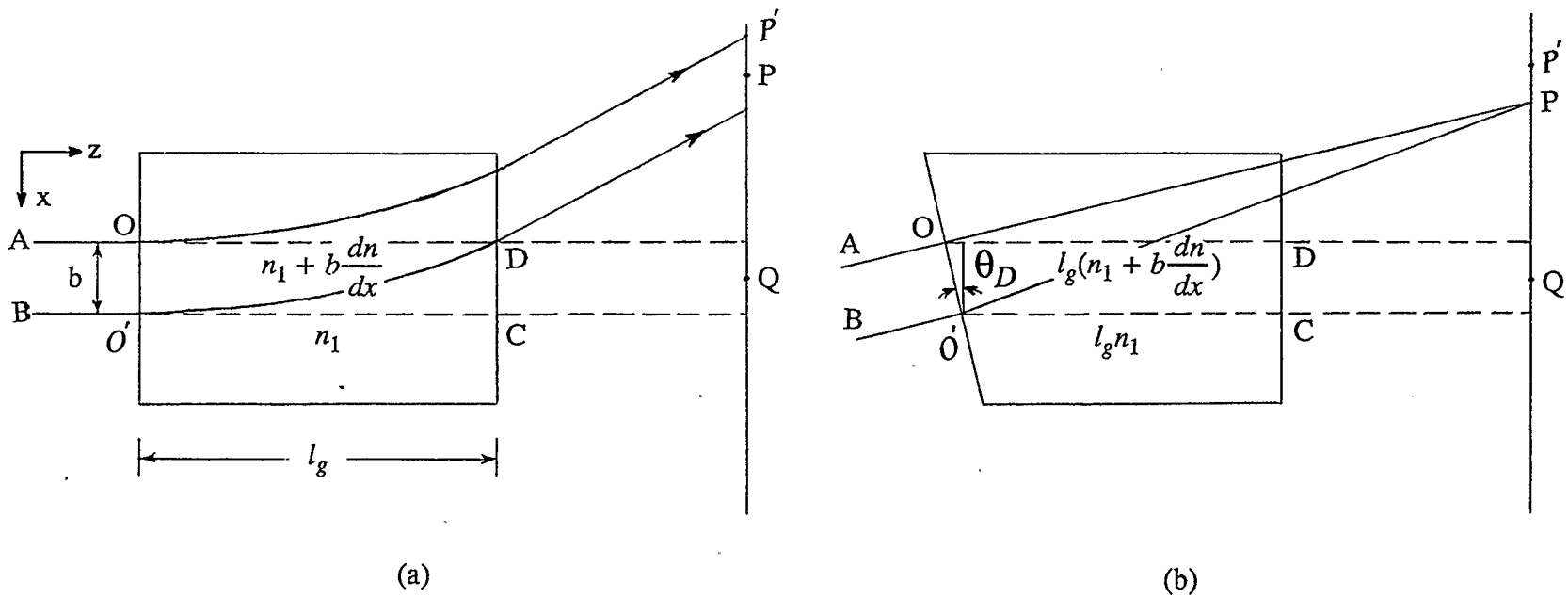

Figure 2.4 Fraunhofer diffraction effects with a linear refractive index gradient

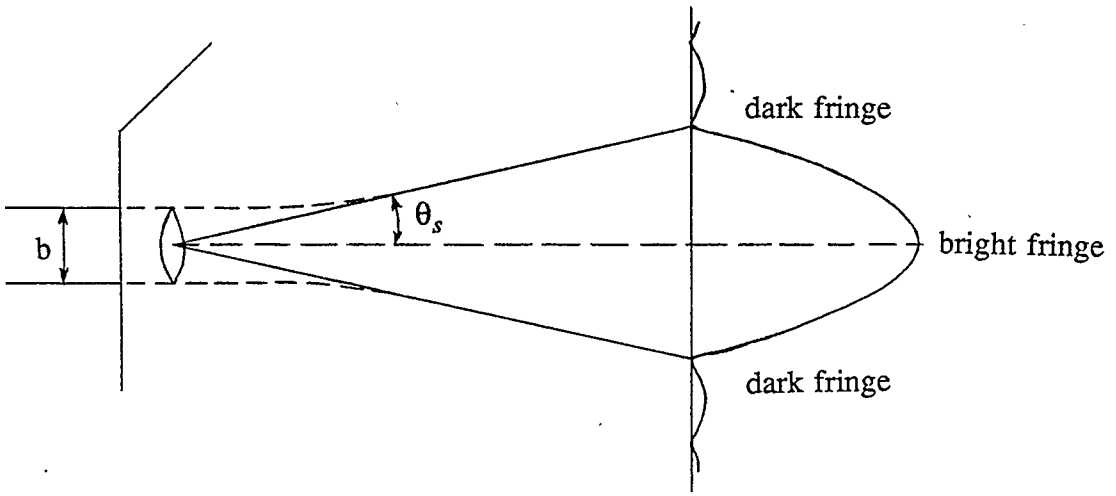

Figure 2.5 Fraunhofer diffraction pattern

screen distance is increased away from the aperture, the bright fringe diameter increases. The diameter of the bright and dark rings are also inversely proportional to the diameter of the aperture.

2.4. Temperature Analysis

As presented in Section 2.2, a refractive index gradient normal to the incident beam is necessary to obtain optical beam deflection within the glass, where the deflection angle is given by Equation (2.11). Since the refractive index within the glass is dependent on temperature, Equation (2.11) can be rewritten as

$$\theta_D \simeq l_g \frac{dn}{dT}\frac{dT}{dx} \tag{2.14}$$

where $\frac{dn}{dT}$ is the change in refractive index with temperature and $\frac{dT}{dx}$, the temperature gradient normal to the direction of the incident light beam. Thus the problem of evaluation of the deflection angle, θ_D, reduces to that of evaluating the temperature gradient, $\frac{dT}{dx}$, since the variation of the refractive index with temperature can be obtained from Figure 1.2 for the different glass samples considered.

The temperature gradient in the sample may be analysed by solving the two-dimensional equation of heat conduction. Within the device the differential equation which governs the heat flow is

$$\frac{\partial}{\partial x}\left[k\frac{\partial T}{\partial x}\right] + \frac{\partial}{\partial y}\left[k\frac{\partial T}{\partial y}\right] = \rho c\frac{\partial T}{\partial t}$$

where k is the thermal conductivity, ρc the specific heat (per unit volume) of the material and $\frac{\partial T}{\partial t}$ the change in temperature with time.

For constant thermal conductivity, the above equation is written as

$$\frac{\partial^2 T}{\partial x^2} + \frac{\partial^2 T}{\partial y^2} = \frac{1}{\alpha}\frac{\partial T}{\partial t} \tag{2.15}$$

where the quantity $\alpha = \frac{k}{\rho c}$ is called the thermal diffusivity of the material.

Before commencing with the thermal analysis of Equation (2.15) the terms and method used for solving the equation are briefly reviewed [21].

2.4.1. Conduction heat transfer

When a temperature gradient exists in a body, there is an energy transfer from the high-temperature region to the low-temperature region. The energy is transferred by conduction and the heat-transfer rate per unit cross-sectional area is proportional to the normal temperature gradient

$$\frac{q}{A} \propto \frac{\partial T}{\partial x}$$

When the proportionality constant is inserted,

$$q = -kA\frac{\partial T}{\partial x} \tag{2.16}$$

Schott glass name	Thermal conductivity k (watt/m^oK)	Specific heat ρc (watt.sec/m^3K)$\times 10^6$	Thermal diffusivity $\alpha=\frac{k}{\rho c}$ $(\frac{m^2}{\text{sec}})\times 10^{-7}$
SF59	0.506	1.91556	2.641
SF57	0.6	2.2718	2.641
SF11	0.737	2.04294	3.6
SF13	0.8868	2.0056	4.4216

Table 2.1 Physical constants of the four Schott glasses

where q is the heat-transfer rate and $\frac{\partial T}{\partial x}$ is the temperature gradient in the direction of the heat flow. The (positive) constant k is called the thermal conductivity of the material, and the minus sign is inserted such that heat must flow down hill on the temperature scale. Equation (2.16) is called Fourier's law of heat conduction and is the defining equation for the thermal conductivity, k having the units of watt/m–^{o}C.

2.4.2. Thermal diffusivity

By definition, thermal diffusivity, $\alpha = \frac{k}{\rho c}$. The larger the value of α, the faster will heat diffuse through the material. This may be seen by examining the quantities which make up α. A high value of α could result either from a high value of thermal conductivity, which would indicate a rapid energy-transfer rate, or from a low value of the thermal heat capacity ρc. A low value of the heat capacity would mean that less of the energy moving through the material would be absorbed and used to raise the temperature of the material; thus more energy would be available for further transfer.

2.4.3. Convection heat transfer

Consider a heated surface with temperature T and the temperature of air surrounding it be T_{∞}. The temperature gradient at the surface is dependent on the rate at which the air carries the heat away. Newton's law of cooling relates the

heat transfer rate to the overall temperature difference between the surface and air and the surface area A by

$$q = hA(T - T_\infty)$$

where h is called the convection heat-transfer coefficient and its units are in watt/m^2–^oC. The approximate value of h for free convection mode in air is 5 - 25 W/m^2–^oC when a heated surface is exposed to ambient room air without an external source of motion.

2.4.4. Heat-transfer analysis

We will now examine the applications of Fourier's law of heat conduction to predict the temperature which results from a certain heat flow. The solution to Equation (2.15) will give the temperature in a two-dimensional body as a function of the two independent space coordinates x and y. The heat flow in the x and y directions may be written from the Fourier equations

$$q_x = -kA_x \frac{\partial T}{\partial x} \tag{2.17a}$$

$$q_y = -kA_y \frac{\partial T}{\partial x} \tag{2.17b}$$

These heat-flow quantities are directed either in the x-direction or in the y-direction. The total heat flow at any point in the material is the resultant of the q_x and q_y at that point.

The numerical method of analysis based on the finite difference technique is used to solve the two-dimensional equation of heat conduction for a rectangular block of glass heated with a heater element on the surface (at x = 0) and placed on an aluminium base. Based on the fact that the length of the glass block is much greater than both its width and thickness it is considered that a two-dimensional analysis will produce results very close to those expected from the very much more complex and difficult to implement three-dimensional model.

The xy plane of the device is divided into equal increments in both the x and y directions as shown in Figure 2.6. The nodal points are designated as shown, the m locations indicating the y increments and the n locations indicating the x increments. We wish to establish the temperatures at any of these nodal points within the body, using Equation (2.15) as the governing condition. Finite differences are used to approximate the differential increments in the temperature, space and time coordinates, and the smaller these finite increments are chosen, the more closely the true temperature distribution will be approximated.

2.4.4.1. Discretisation in space

The temperature gradients may be written as follows [21]

$$\left.\frac{\partial T}{\partial y}\right]_{m+\frac{1}{2},n} \approx \frac{T_{m+1,n} - T_{m,n}}{\Delta y}$$

$$\left.\frac{\partial T}{\partial y}\right]_{m-\frac{1}{2},n} \approx \frac{T_{m,n} - T_{m-1,n}}{\Delta y}$$

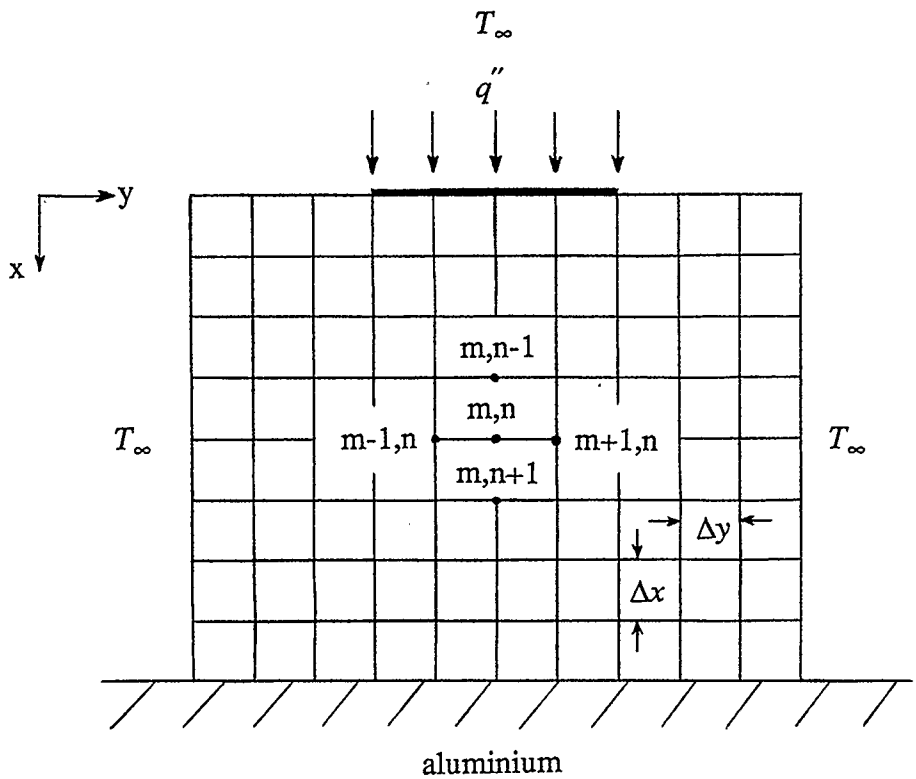

Figure 2.6 Sketch illustrating nomenclature used in 2-dimensional numerical analysis of heat conduction

$$\left.\frac{\partial T}{\partial x}\right]_{m,n+\frac{1}{2}} \approx \frac{T_{m,n+1} - T_{m,n}}{\Delta x}$$

$$\left.\frac{\partial T}{\partial x}\right]_{m,n-\frac{1}{2}} \approx \frac{T_{m,n} - T_{m,n-1}}{\Delta x}$$

$$\left.\frac{\partial^2 T}{\partial y^2}\right]_{m,n} \approx \frac{\left.\frac{\partial T}{\partial y}\right]_{m+\frac{1}{2},n} - \left.\frac{\partial T}{\partial y}\right]_{m-\frac{1}{2},n}}{\Delta y} \tag{2.18a}$$

$$= \frac{T_{m+1,n} + T_{m-1,n} - 2T_{m,n}}{(\Delta y)^2}$$

$$\left.\frac{\partial^2 T}{\partial x^2}\right]_{m,n} \approx \frac{\left.\frac{\partial T}{\partial x}\right]_{m,n+\frac{1}{2}} - \left.\frac{\partial T}{\partial x}\right]_{m,n-\frac{1}{2}}}{\Delta x} \tag{2.18b}$$

$$= \frac{T_{m,n+1} + T_{m,n-1} - 2T_{m,n}}{(\Delta x)^2}$$

2.4.4.2. Discretisation in time

The time derivative in Equation (2.15) is approximated by

$$\frac{\partial T}{\partial t} \approx \frac{T_{m,n}^{p+1} - T_{m,n}^{p}}{\Delta t} \tag{2.19}$$

In this relation the superscripts designate the time increment.

2.4.4.3. Finite difference equations

Using Equations (2.18) and (2.19) the finite difference approximation for Equation (2.15) becomes

$$\frac{T^p_{m+1,n} + T^p_{m-1,n} - 2T^p_{m,n}}{(\Delta y)^2} + \frac{T^p_{m,n+1} + T^p_{m,n-1} - 2T^p_{m,n}}{(\Delta x)^2} = \frac{1}{\alpha}\frac{T^{p+1}_{m,n} - T^p_{m,n}}{\Delta t} \tag{2.20}$$

In effect, the numerical finite-difference approach replaces the continuous temperature distribution by fictitious heat conducting rods connected between small nodal points. If the temperatures of the various nodes are known at any particular time, the temperatures after a time increment Δt may be calculated by writing an equation like Equation (2.20) for each node and obtaining the values of $T^{p+1}_{m,n}$. The procedure may be repeated to obtain the distribution after any desired number of time increments. If the increments of space coordinates are chosen such that

$$\Delta x = \Delta y$$

the resulting equation for $T^{p+1}_{m,n}$ becomes

$$T^{p+1}_{m,n} = \frac{\alpha\Delta t}{(\Delta x)^2}\,(T^p_{m+1,n} + T^p_{m-1,n} + T^p_{m,n+1} + T^p_{m,n-1}) + [1 - 4\frac{\alpha\Delta t}{(\Delta x)^2}]\,T^p_{m,n} \tag{2.21}$$

The finite difference equations limit the values of Δt which may be used once Δx is chosen. For the stability and convergence of numerical solutions the coefficient of

$T^p_{m,n}$ should be less than or equal to zero, therefore the values of Δx and Δt are restricted by

$$\frac{(\Delta x)^2}{\alpha \Delta t} \geq 4 \tag{2.21a}$$

Different geometric shapes that occur for the problem considered are shown in Figure 2.7. The difference equation given by Equation (2.21) is used for determining the temperatures for internal nodes in the glass block shown in Figure 2.7a as a function of space and time. At the boundary of the solid a convection resistance to heat flow is involved, so that the above relation no longer applies. Each convection boundary condition must be handled separately, depending on the particular geometric shape under consideration. A transient energy balance on the node (m,n) is made by setting the sum of the energy conducted and convected into the node equal to the increase in the internal energy of the node.

For the physical situation shown in Figure 2.7b with a vertical convection boundary node, the difference equation is given by

$$T^{p+1}_{m,n} = \frac{\alpha \Delta t}{(\Delta x)^2} \left\{ 2\frac{h_V \Delta x}{k} T_\infty + 2T^p_{m-1,n} + T^p_{m,n+1} + T^p_{m,n-1} - [2\frac{h_V \Delta x}{k} + 4 - \frac{(\Delta x)^2}{\alpha \Delta t}]\, T^p_{m,n} \right\} \tag{2.22}$$

where h_V is the heat transfer-coefficient for a vertical boundary. Similarly for the situation shown in Figure 2.7c, the difference equation is

$$T_{m,n}^{p+1} = \frac{\alpha\Delta t}{(\Delta x)^2}\left\{2\frac{h_V\Delta x}{k}T_\infty + 2T_{m+1,n}^p + T_{m,n+1}^p + T_{m,n-1}^p - [2\frac{h_V\Delta x}{k} + 4 - \frac{(\Delta x)^2}{\alpha\Delta t}]\, T_{m,n}^p\right\} \tag{2.23}$$

For the horizontal convection boundary node at x = 0, as shown in Figure 2.7d, the difference equation is

$$T_{m,n}^{p+1} = \frac{\alpha\Delta t}{(\Delta x)^2}\left\{2\frac{h_H\Delta x}{k}T_\infty + 2T_{m,n+1}^p + T_{m-1,n}^p + T_{m+1,n}^p - [2\frac{h_H\Delta x}{k} + 4 - \frac{(\Delta x)^2}{\alpha\Delta t}]\, T_{m,n}^p\right\} \tag{2.24}$$

where h_H is the heat transfer-coefficient for a horizontal boundary.

For the situation in Figure 2.7e, the difference equation is

$$T_{m,n}^{p+1} = \frac{\alpha\Delta t}{(\Delta x)^2}\left\{2\frac{K_{Al}\Delta x}{k}T_\infty + 2T_{m,n-1}^p + T_{m-1,n}^p + T_{m+1,n}^p - [2\frac{K_{Al}\Delta x}{k} + 4 - \frac{(\Delta x)^2}{\alpha\Delta t}]\, T_{m,n}^p\right\} \tag{2.25}$$

where K_{Al} is the coefficient which takes care of conduction in aluminium.

Writing the energy balance equations for exterior corners with convection boundary, the difference equation for Figure 2.7f is

$$T^{p+1}_{m,n} = \frac{\alpha\Delta t}{(\Delta x)^2}\left\{2\frac{(h_V+h_H)\Delta x}{k}T_\infty + 2T^p_{m-1,n} + 2T^p_{m,n+1} - [2\frac{(h_V+h_H)\Delta x}{k} + 4 - \frac{(\Delta x)^2}{\alpha\Delta t}]\ T^p_{m,n}\right\} \tag{2.26}$$

The difference equation for Figure 2.7g is

$$T^{p+1}_{m,n} = \frac{\alpha\Delta t}{(\Delta x)^2}\left\{2\frac{(h_V+h_H)\Delta x}{k}T_\infty + 2T^p_{m+1,n} + 2T^p_{m,n+1} - [2\frac{(h_V+h_H)\Delta x}{k} + 4 - \frac{(\Delta x)^2}{\alpha\Delta t}]\ T^p_{m,n}\right\} \tag{2.27}$$

For Figure 2.7h, the equation is

$$T^{p+1}_{m,n} = \frac{\alpha\Delta t}{(\Delta x)^2}\left\{2\frac{(h_V+K_{Al})\Delta x}{k}T_\infty + 2T^p_{m+1,n} + 2T^p_{m,n-1} - [2\frac{(h_V+K_{Al})\Delta x}{k} + 4 - \frac{(\Delta x)^2}{\alpha\Delta t}]\ T^p_{m,n}\right\} \tag{2.28}$$

For Figure 2.7i, the equation is

$$T^{p+1}_{m,n} = \frac{\alpha\Delta t}{(\Delta x)^2}\left\{2\frac{(h_V+K_{Al})\Delta x}{k}T_\infty + 2T^p_{m-1,n} + 2T^p_{m,n-1} - [2\frac{(h_V+K_{Al})\Delta x}{k} + 4 - \frac{(\Delta x)^2}{\alpha\Delta t}]\ T^p_{m,n}\right\} \tag{2.29}$$

The values of Δx and Δt are now restricted by

$$\frac{(\Delta x)^2}{\alpha\Delta t} \geq 2\left\{\frac{(h_V+K_{Al})\Delta x}{k} + 2\right\} \tag{2.29a}$$

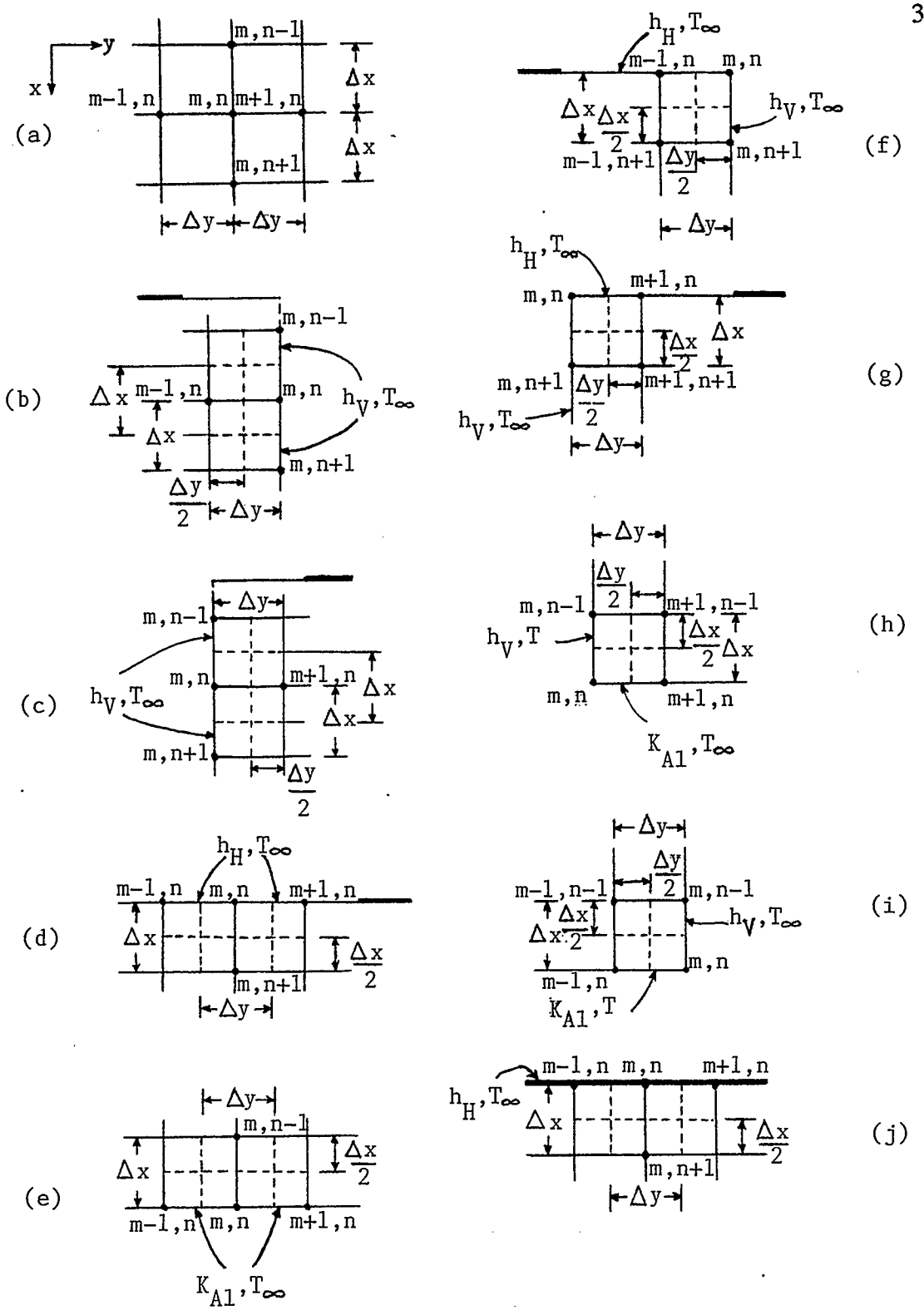

Figure 2.7 Nomenclature for numerical solutions of different geometric shapes

With the surface heat flux q'' (units in watts/m^2) due to the heater element on the surface of the glass block, the difference equation for the physical situation shown in Figure 2.7j is

$$T_{m,n}^{p+1} = \frac{\alpha\Delta t}{(\Delta x)^2}\left\{2\frac{h_H\Delta x}{k}T_\infty + 2T_{m,n+1}^p + T_{m-1,n}^p + T_{m+1,n}^p - [2\frac{h_H\Delta x}{k} + 4 - \frac{(\Delta x)^2}{\alpha\Delta t}]\,T_{m,n}^p\right\} + 2\frac{\alpha\Delta t}{\Delta x}\frac{q''}{k} \tag{2.30}$$

Equations (2.21) to (2.30) are solved simultaneously for all nodal points at each time increment for any desired total number of time increments.

The equations above have been developed on the basis of a forward difference technique in that the temperature of a node at a future time increment is expressed in terms of the surrounding nodal temperatures at the beginning of the time increment. The expressions are called explicit formulations and the procedure involves the direct calculation of the future nodal temperatures $T_{m,n}^{p+1}$ in terms of the previous nodal temperatures $T_{m,n}^p$. In this formulation, the calculation proceeds directly from one time increment to the next until the temperature distribution is calculated at the desired final state.

The values of the average heat-transfer coefficients for free convection from various surfaces to air at atmospheric pressure are obtained using the following empirical equations [21]:

(1) For both heated and cooled vertical surfaces, the heat-transfer coefficient h_V is given by

$$h_V = 0.29\left[\frac{\Delta T}{L}\right]^{\frac{1}{4}} \tag{2.31a}$$

(2) For a heated horizontal surface facing upward, the heat-transfer coefficient h_{Hh} is given by

$$h_{Hh} = 0.27\left[\frac{\Delta T}{L}\right]^{\frac{1}{4}} \tag{2.31b}$$

This expression of h_H is used in Equations (2.24), (2.26), (2.27) and (2.30) when a voltage is applied to the heater element on the surface of glass, that is, when q'' is not equal to zero.

(3) For a cooled horizontal surface facing upward, the heat-transfer coefficient h_{Hc} is given by

$$h_{Hc} = 0.12\left[\frac{\Delta T}{L}\right]^{\frac{1}{4}} \tag{2.31c}$$

The value obtained from this expression of h_H is used when the applied heater power is zero, that is, $q'' = 0$.

In Equations (2.31a) to (2.31c), ΔT is given by

$$\Delta T = T_{surface} - T_{\infty}$$

and L is the mean of the two dimensions for a rectangular surface given by

$$\frac{1}{L} = \frac{1}{L_h} + \frac{1}{L_v}$$

where L_h and L_v are the horizontal and vertical dimensions respectively. The values for heat-transfer coefficient as obtained from Equation (2.31) may effect the theoretical results to a small extent.

A detailed formulation of Equations (2.22) to (2.30) is dealt with in the Appendix. These expressions are used to tie together the theoretical results of Chapter 4.

2.5. Summary

In this chapter, the theory of the thermooptic effect originating from the temperature dependence of the refractive index of the dielectric, glass, is considered. Expressions for the temperatures of different nodes within the glass, with the effects of convection boundaries and surface heat flux, are also derived. These expressions are required to analyse the physical property, $\frac{dT}{dx}$, of the glass which results in light deflection. The next Chapter will deal with the experimental method used to obtain the light beam deflection and switching.

CHAPTER 3

IMPLEMENTATION OF OPTICAL SWITCH

3.1. Introduction

This chapter first deals with the preparation of the glass TO bulk deflector which includes polishing and cleaning the glass samples, vacuum deposition of the heater elements, annealing of the heater film and finally making the electrical contacts to the film. The experimental setup required to obtain the light beam deflection is further described. A theoretical description of the experimental setup for the transient analysis of the switch is also presented.

3.2. Device Structure and Fabrication

The structure of a 1-dimensional 1×2 TO bulk deflector is illustrated in Figure 3.1. The active component of the device is a $24\text{mm} \times 5\text{mm} \times 2.3\text{mm}$ Schott glass block. The light beam deflection is due to the index gradient caused by applying an appropriate voltage to the film heater on the upper glass surface. In the absence of the heater voltage the incident beam will encounter no refractive index change within the glass and it will be transmitted with no internal deflection.

The preparation of the TO bulk deflector samples begins with the precision cutting of the glass samples to the required size. A mechanical method of variable speed is used for grinding and polishing the two end-faces of glass. Plastic is used

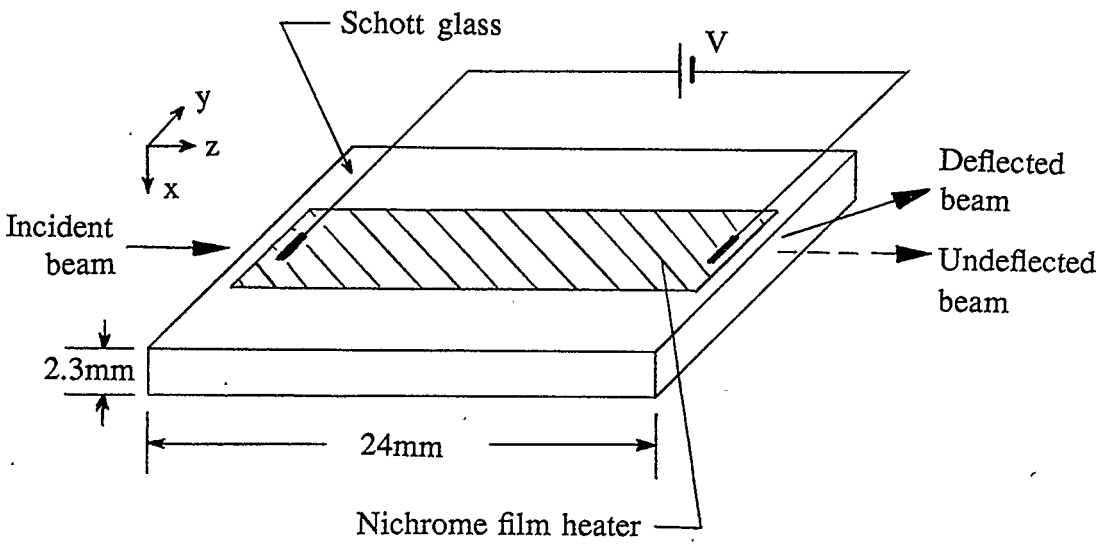

Figure 3.1 Structure of a 1-D, 1×2 TO bulk deflector

for mounting the glass to the grinding and polishing machine. The grinding is done with 600 grid silicon carbide paper with oil as the lubricant. Finally 1 micron diamond paste is used for optically polishing the two end-faces of the glass samples. It is vitally important that these two end faces be as parallel as possible. All other surfaces are hand polished with #200 silicon carbide finishing paper to help remove any microcracks that may initiate fracture lines when the glass is heated on the surface by applying a voltage to the heater element (advice from Schott Glass Co.). In view of the surface properties of the substrate having a marked effect on the specimen quality, the glass samples are ultrasonically cleaned with acetone and methanol solvents before the heater element is evaporated onto the surface of the samples.

The approximately 2mm wide heating strips are prepared in a vacuum deposition plant (Edwards High Vacuum Ltd.) having a 12 inch diameter chamber equipped with pumps capable of reducing the pressure in the vacuum chamber below 10^{-6} torr. The alloy of chromium with nickel (80% Ni and 20% Cr) is chosen to be the material for the heater because of the high stability resistance films obtained from them by correct annealing treatment and suitable protection. The films of the alloy are also thicker, due to their high bulk resistivity (80-130 $\mu\Omega$cm), than films of the pure metals for the same resistance values. Films of resistance 400 Ω/square are at least 8nm thick, more or less continuous and are outside the very unstable region of thickness. The nickel-chromium alloy films also have a low temperature coefficient of resistance in bulk, and have very high

chemical stability [22].

It has been recommended that the substrate glass be heated in a vacuum before deposition to a temperature above 200°C. This relieves the high internal stresses in the film and removes some defects in the crystal lattice, thus improving the heat stability. A further heating in air for 30 minutes at 300°C completes the annealing of the film, making the film less subject to an external atmospheric attack [22].

The vacuum chamber heating apparatus used for nichrome film preparation on glass is shown in Figure 3.2. It consists of a silica glass cylinder 4 inch diameter with an aluminium gauze placed on the upper side to support the glass samples. A nichrome heating filament, dissipating 200 watts at 40V, is housed inside the silica glass cylinder. This is used to raise the substrate temperature to the required value during evaporation. The temperature is measured by means of a copper-constantum thermocouple placed inside the vacuum chamber with its junction resting on the top face of aluminium gauze - thus an approximate temperature reading for the substrate is obtained. The thermocouple is connected to an external meter and provision for the electrodes which connect the radiant heater and the thermocouple in the vacuum chamber is made through vacuum sealed holes in the aluminium lid of the chamber.

Before being placed in the vacuum chamber the glasses are suitably masked individually by very thin steel strips to obtain a sharp step from the film to the glass. The optically polished sides of the glasses are also carefully masked to

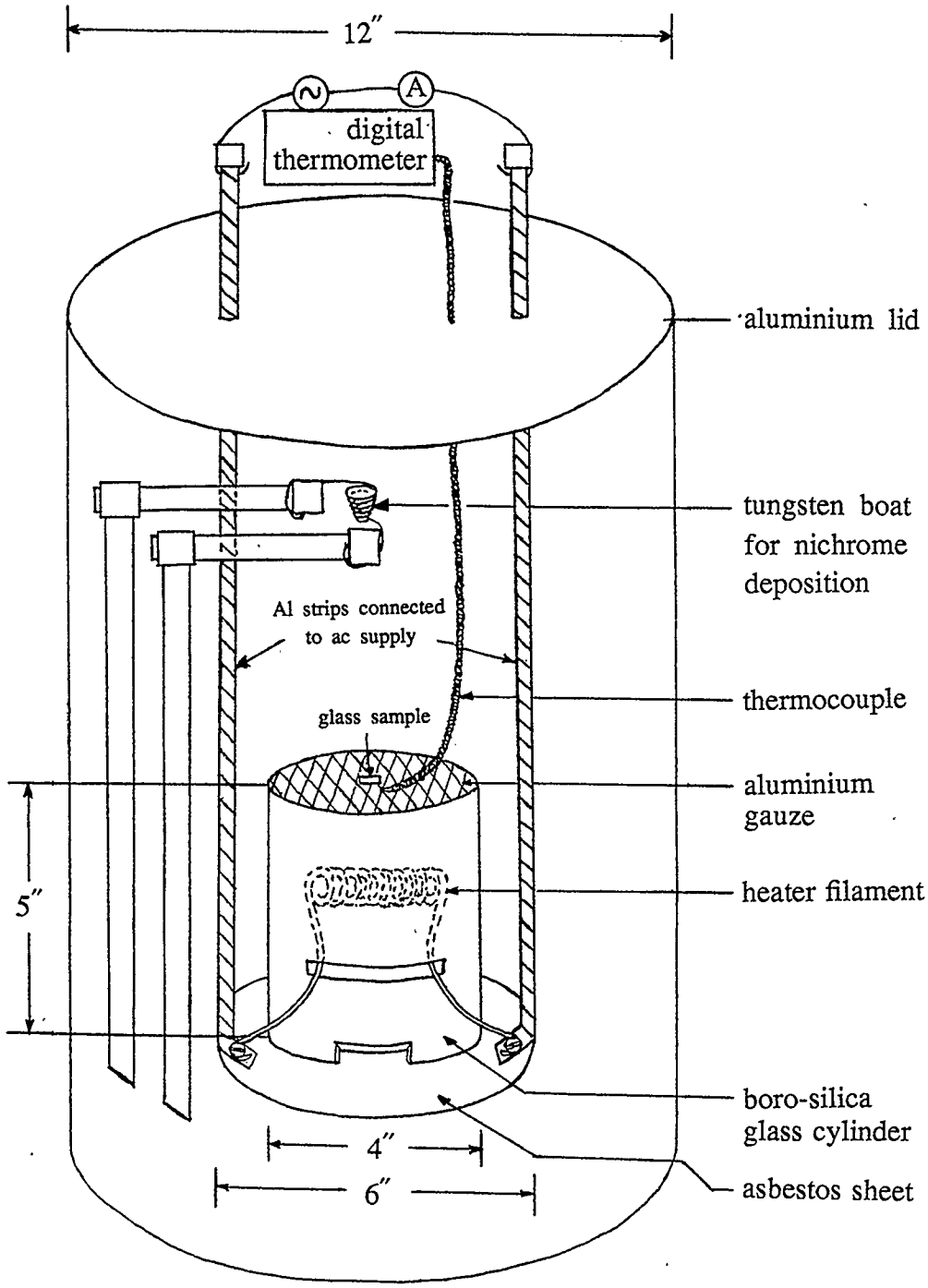

Figure 3.2 Vacuum chamber heating apparatus used for nichrome film preparation on glass

prevent the evaporation of nichrome on them. The nickel-chromium wire (24*swg*) is placed directly above the glass samples in a tungsten boat. The chamber is now evacuated to a pressure of less than 10^{-5} torr and the substrates heated to a temperature of 200°C by means of the nichrome heater element. The samples are heat treated for about 10 minutes before a known amount of nickel-chromium is deposited on their surfaces.

It is observed that when heating the substrate the pressure of the vacuum chamber increased to $\sim 10^{-3}$ torr and that there is no effective way to reduce the pressure in order to obtain a better vacuum. The tungsten boat is fed with a power of 400 watts at 10 V to evaporate the nichrome. The film obtained by the above procedure does not prove to have a good bonding with the glass and is virtually a non-conducting film. The principal gases which evolve from glasses upon heating are water vapour and carbon dioxide. The gas quantities released into vacuum are significantly greater for aged than for freshly drawn glass. Another source of glass-surface contamination is oil-diffusion-pump vapours which are firmly chemisorbed by dehydrated (baked) glass surfaces. The resulting surface film may weaken the adhesion of subsequently deposited films on the glass substrate surfaces [23].

Thus in order to obtain conducting films with a better adhesion property, the glass samples are vacuum evaporated at room temperatures since the outgassing rates are slow at room temperatures, thereby not changing the pressure in the vacuum chamber to a significant extent. During deposition, the Schott glass

surfaces suitably masked, are placed in a rotary substrate holder to equalise the deposition. After evacuation and evaporation the chamber is allowed to cool before breaking the vacuum.

Heat treatment carried out after deposition also serves the purpose of relieving the high internal stresses in the film. Baking after deposition re-orders the crystal lattice, and improves the resistance stability with time, also forming a compact oxide surface layer [22]. The stabilisation or annealing of the resistance films is carried out in a special oven in air at atmospheric pressure and the temperature of the oven is raised to 200°C and maintained at this level for about 10 minutes. The oven is then allowed to cool to less than 100°C before the samples are removed.

The method of making contacts to the deposited film influences both the accuracy with which the film can be measured and the ultimate stability. Electrical contacts to the thin resistance films are made using conducting paste (Loctite grid repairing paste) and .001 inch thick brass sheets and this resulted in slight differences in the heater lengths for the different glass samples. The values of the widths and lengths of the heater elements obtained for the different Schott glass samples are given in Table 3.1. The film resistances for the different glass samples are in the range of 2 kΩ to 3 kΩ.

A unique property of the glass TO bulk deflector is its ability to utilise its optical isotropy to produce a 2-dimensional switching action. The structure of such a 2-D 1×4 TO bulk deflector is illustrated in Figure 3.3. The two heater elements are placed on adjacent faces, in the x and y-axis of the device. The 2-

Schott glass name	heater width (mm)	heater length (mm)	heater area A (mm^2)
SF59	2.25	17.0	38.25
SF57	2.0	15.5	31.0
SF11	1.75	17.0	29.75
SF13	2.25	17.0	38.25

Table 3.1 Experimentally obtained heater areas for the Schott glasses

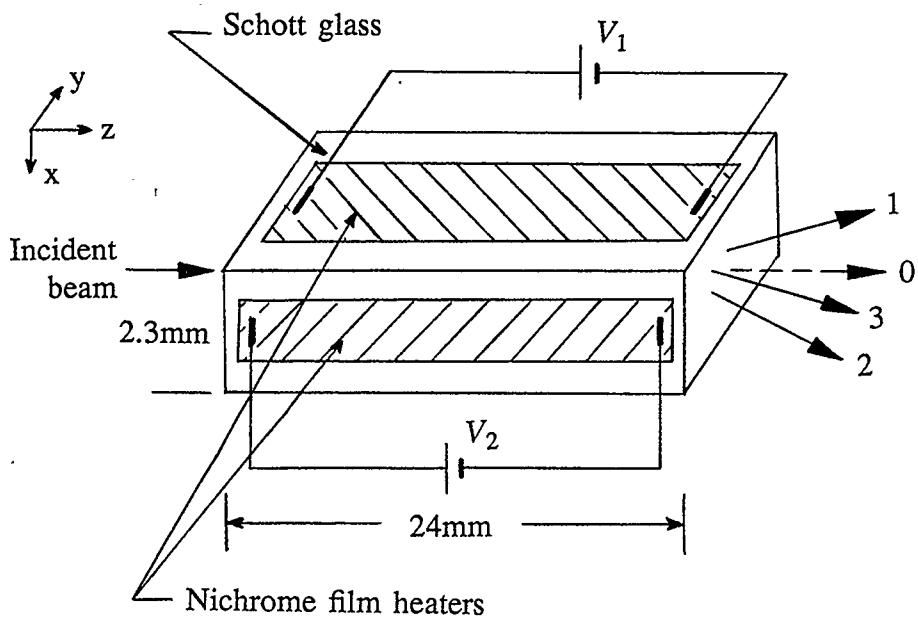

Figure 3.3 Structure of a 2-D, 1×4 TO bulk deflector

dimensional switch heater elements are prepared in the same manner as described above.

3.3. Experimental set-up

The schematic diagram for the experimental set-up required to observe light deflection in glass is shown in Figure 3.4. A Helium Neon laser at a wavelength of 632.8nm with a beam width of approximately 1mm is used as a source of collimated light. A plano-convex lens of 200mm focal length is used to focus the input beam to approximately 0.2mm on the optically polished side of the glass. The plano side of the lens faces the glass. The screen is at a distance of approximately 1860mm from the glass. The optical deflection experimental equipment used in the present work is shown in Figure 3.5. The laser and the optical set-up are situated on top of a vibration-isolation optical bench, a stainless steel magnetic surface providing good stability and proper horizontal levelling of the bench setup. The laser, lens and the glass are mounted on the optical bench with their individual holders. The laser holder gives firm support to the laser and provides a vertical movement and an angular movement in the vertical direction to ensure the laser beam is parallel to the horizontal axis of the switch. The lens holder is also mountable on the optical bench in the plane of the input beam. A digital micrometer (1 μm accuracy) is fitted along the vertical axis of the glass holder for precisely controlling the position of the He-Ne input beam under the film heater (in x-direction of Figures 3.1 and 3.3). The glass holder is made of

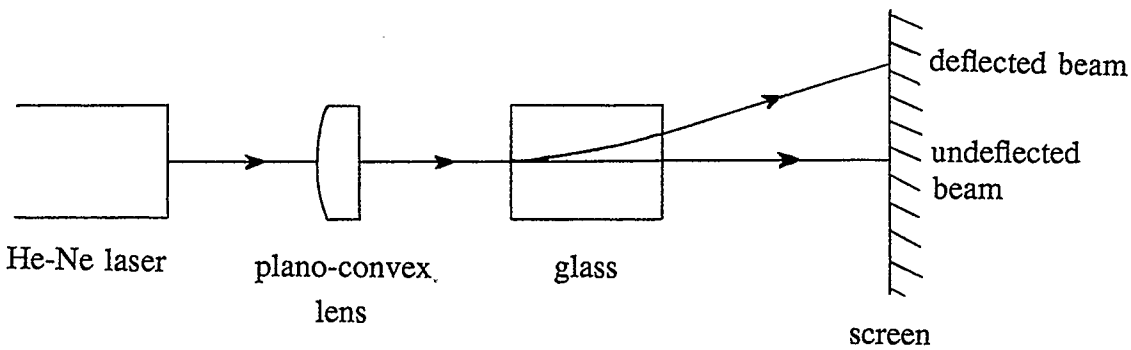

Figure 3.4 Schematic diagram of the experimental set-up

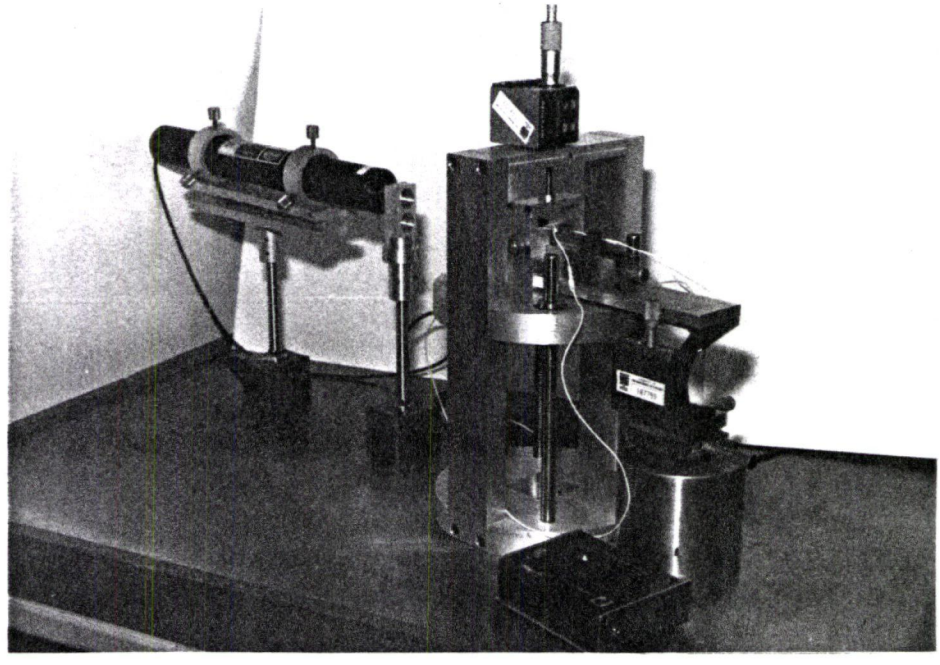

Figure 3.5 Optical deflection experimental equipment

aluminium. Mounting the glass for testing must not introduce compressive stresses else it is liable to fracture. Therefore the glass is placed on the aluminium base of the holder with all other surfaces exposed to the atmospheric conditions. Figure 3.5 also shows an XYZ mount for holding the communications quality fibres at the output end of the switch. The graded index fibre (62.5 μm core-125 μm cladding) used is either connected to a power meter to determine the extinction ratio ER (ratio of the output switch-off power level state to the switch-on state) or to a waveform analyzer which converts the input optical power signals into electrical output signals. The output of the waveform analyzer is plugged directly into the oscilloscope to observe the transient response of the switch.

3.3.1. Procedure for the Experiment

The observations of the beam deflection angle and the extinction ratio are made for the 1-dimensional 1×2 TO circuit switch by applying a dc voltage to the heater element on the surface of the glass. The 0.2mm input beam is incident at a distance of 0.3mm from the heater surface. The position of the incident beam is controlled by the vertical micrometer adjustment. The activation of the switch by the application of heater power causes the input beam to be deflected towards the heater element. The deflection is observed on the screen and the distance between the maximum intensity spots for the undeflected and deflected beam is noted. The procedure is repeated for different heater powers and different types of the Schott glasses considered. The effect of the incident beam position on the

deflection angle is observed by increasing the position of the incident beam from the heater surface by the use of the vertical micrometer. The observation of the extinction ratio is made by detecting the power in the fibre at the output end of the switch. The fibre is placed at the maximum power position by the use of the XYZ mount when the heater power is off. The decrease in the power level in dB is recorded from the power meter with the heater power on. The transient response of the switch is observed by applying a pulsed voltage to the heater element. A power transistor is used to amplify the voltage from the pulse generator to the required heater voltage levels.

3.4. Theoretical Description of Experimental setup for Pulsed Heater Operation

The sectional view of the device along the z-axis at y = 2.5mm is shown in Figure 3.6. The input beam is incident at x = 0.3mm with a beam diameter of 0.2mm. The fibre is positioned along the path of the beam at the output end. Since the fibre diameter which is equal to the maximum value of w_f is less than the beam diameter it could have a displacement s along the x-axis.

For small deflection angles, it can be written that $\theta_D \simeq x_d / l_g$ where x_d is the deflection in the x-axis. The corresponding temperature gradient required for the beam to travel the distance x_d is given by substituting Equation (2.14) for the beam deflection angle:

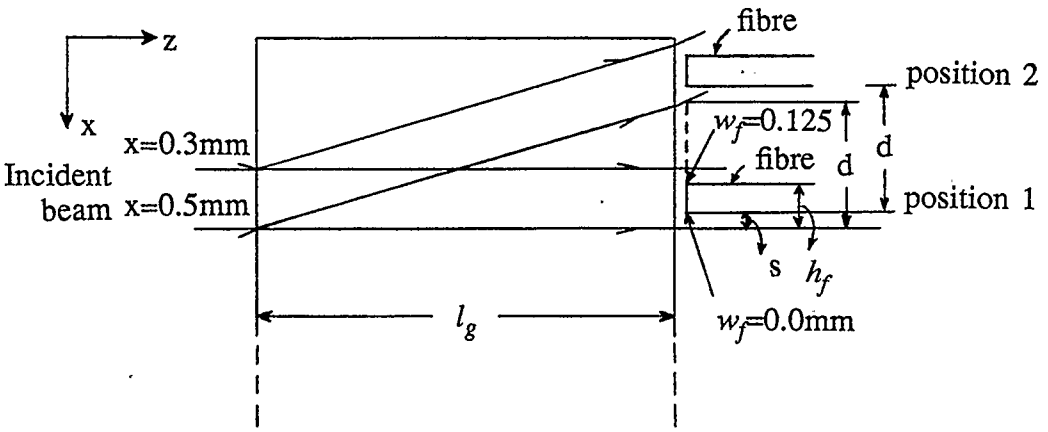

Figure 3.6 Sectional view of the device showing fibre placement

$$\left.\frac{dT}{dx}\right|_{x_d} \simeq \frac{x_d}{l_g^2(\frac{dn}{dT})} \tag{3.1}$$

The temperature gradient required for the beam to be deflected by any amount of distance can be similarly calculated from Equation (3.1). The variation of the temperature gradient with respect to time can be obtained by solving the two-dimensional equation of heat conduction as described in Section 2.4. When a heater power is applied for a certain pulse width duration, d is the maximum deflection obtained, the beam being switched from position 1 to position 2. The corresponding temperature gradient is $\left.\frac{dT}{dx}\right|_d$ for $x_d = d$. Now when the heater power is off for the remaining duration of the pulse, the beam will deflect back from position 2 to position 1.

With the heater power on, the fibre at position 1 starts to experience a decrease in its received power level only when the beam is deflected by an amount equal to s and the corresponding $\left.\frac{dT}{dx}\right|_s$ required is for $x_d = s$ in Equation (3.1). The power in fibre at position 1 is zero when a $\left.\frac{dT}{dx}\right|_{h_f}$ for $x_d = h_f$ is reached. The corresponding time required is the rise time t_r of the switch. The detected power at position 1 remains zero until the beam has travelled the distance d (with the input heater voltage pulse high) and back to the fibre at position 1 (when the input heater voltage pulse level is zero). The time taken by the beam to travel the distance $d - h_f$ is the delay time t_d of the switch. Now the fibre at position 1 starts

experiencing an increase in its power level, the maximum power being detected when the beam has reached the distance $x_d = s$. The time corresponding to $\left.\frac{dT}{dx}\right|_s$ for $x_d = s$ when the input heater power is zero gives the fall time t_f of the switch.

The initial distance s at which the fibre is placed effects the transient response of the switch in terms of its rise time and fall time. If s is large, the distance $h_f = w_f + s$ increases, resulting in a higher $\left.\frac{dT}{dx}\right|_{h_f}$ to give a larger rise time than when s is small. But the delay time and fall time decreases since now the beam has to travel a smaller distance to return back to the fibre at position 1 for a given input power.

The distance s at which the fibre is placed at the output end can be calculated from $s = l_g^2 \frac{dn}{dT} \left.\frac{dT}{dx}\right|_s$ [rewriting Equation (3.1)] where the temperature gradient $\left.\frac{dT}{dx}\right|_s$ is obtained from the theoretical curves based on the experimental time taken for the beam to travel the distance s.

3.5. Summary

In this Chapter, the different steps required for the preparation of the glass thermo-optic bulk deflector have been described. The experimental equipment to obtain light beam deflection and switching is shown. A theoretical description of the experimental setup to analyze the transient response of the switch based on the

physical property $\frac{dT}{dx}$ is considered. The next Chapter will deal with the theoretical results obtained by solving the two-dimensional equation of heat conduction for the heater areas fabricated.

CHAPTER 4

THEORETICAL RESULTS

4.1. Introduction

The results based on the theory presented in Chapter 2, with respect to the Fraunhofer diffraction effects and the temperature analysis of glass with the heater power applied on the surface, are presented in this Chapter. The Fraunhofer diffraction effects due to the finite width of the input beam with and without the heater power applied are first considered for all the four types of Schott glasses. The temperature analysis results for the dc and pulsed operation of the heater voltage, characterising the physical properties of the glass samples, are presented later. The results for the deflection angle due to the presence of the temperature gradient are also shown.

4.2. Fraunhofer Diffraction Effects

The effects of the finite beam width of 0.2mm (which is assumed to be collimated) passing through the glass are shown in Figures 4.1 to 4.4 for the four Schott glasses SF59, SF57, SF11 and SF13 respectively. The diffraction effects with the heater power applied are also shown in the same Figures. The intensity curves are at a distance of 1860mm from the glass for the input beam incident at x = 0.3mm from the heater surface of the glass, the axis chosen being same as that

shown in Figure 3.1. Since the deflection occurs towards the heater element the Figures show a shift in the Fraunhofer diffraction pattern towards the $-x$ axis.

When the heater power is not applied there is a uniform refractive index in the medium and Q is the maximum intensity spot as shown in Figure 2.3. Since the input wavefront extends from x = 0.3mm to x = 0.5mm, the maximum intensity occurs at x = 0.4mm as shown in Figures 4.1 to 4.4 for all the glasses. With the heater power applied, a refractive index gradient occurs and the maximum intensity spot now shifts to point P as shown in Figure 2.4. Figure 4.1 shows the intensity curves for the Schott glass SF59. The point P occurs at x = -21.3mm when the heater power P_H of approximately 1W is applied. The deflection d from x = 0.4mm to x = -21.3mm is therefore 21.7 mm. The deflection d increases as applied heater power is increased, d being 46.5mm for heater power of 2.06375W. Figure 4.2 shows the intensity curves for SF57. The deflection is of the order of 16.9mm for a heater power of 0.925W and increases to 38.3mm for P_H = 2.04375W. Figures 4.3 and 4.4 show the intensity curves similarly for SF11 and SF13. It is obvious from the Figures that SF59 exhibits the maximum deflection whereas SF13 has the lowest amount of deflection among the four types of Schott glasses. This is due to the fact that SF59 has the maximum refractive index gradient.

The Figures 4.1 to 4.4 also show an increase in the beam diameter from 0.2mm to approximately 14.7mm for both the undeflected and deflected beams. The beam spread angle θ_s (Figure 2.5) is therefore given by

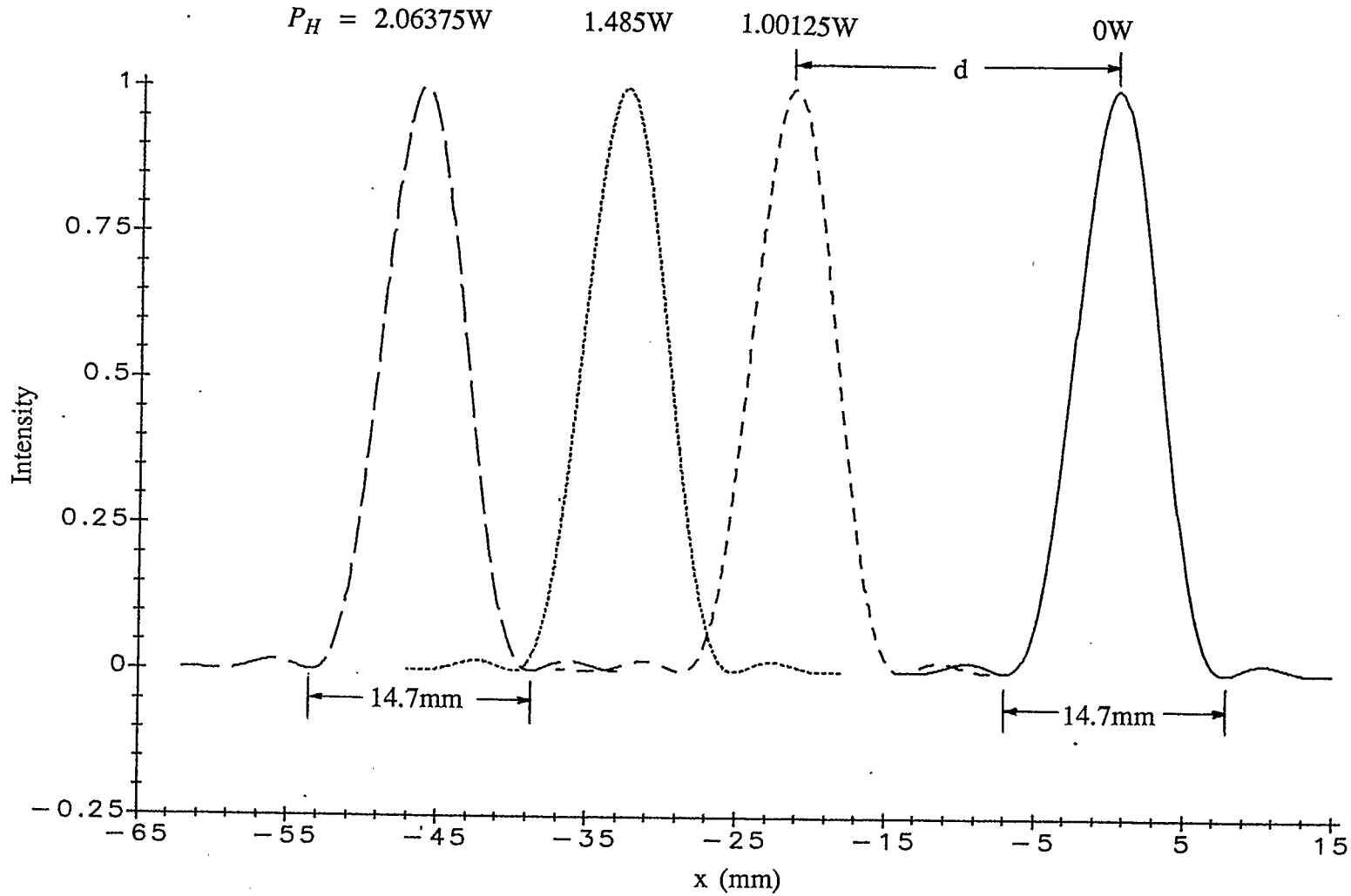

Figure 4.1 Intensity distribution for Fraunhofer diffraction for glass type SF59

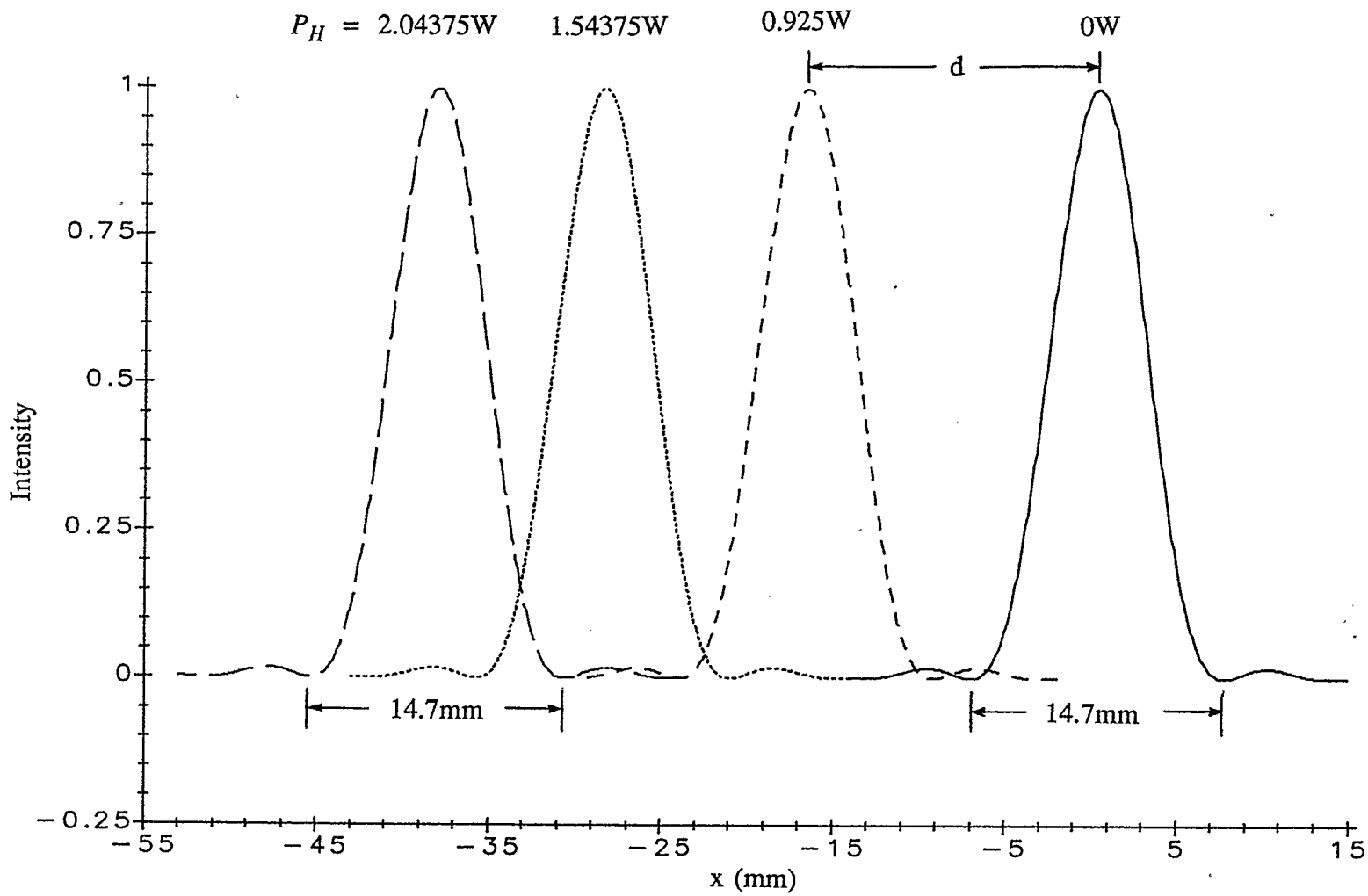

Figure 4.2 Intensity distribution for Fraunhofer diffraction for glass type SF57

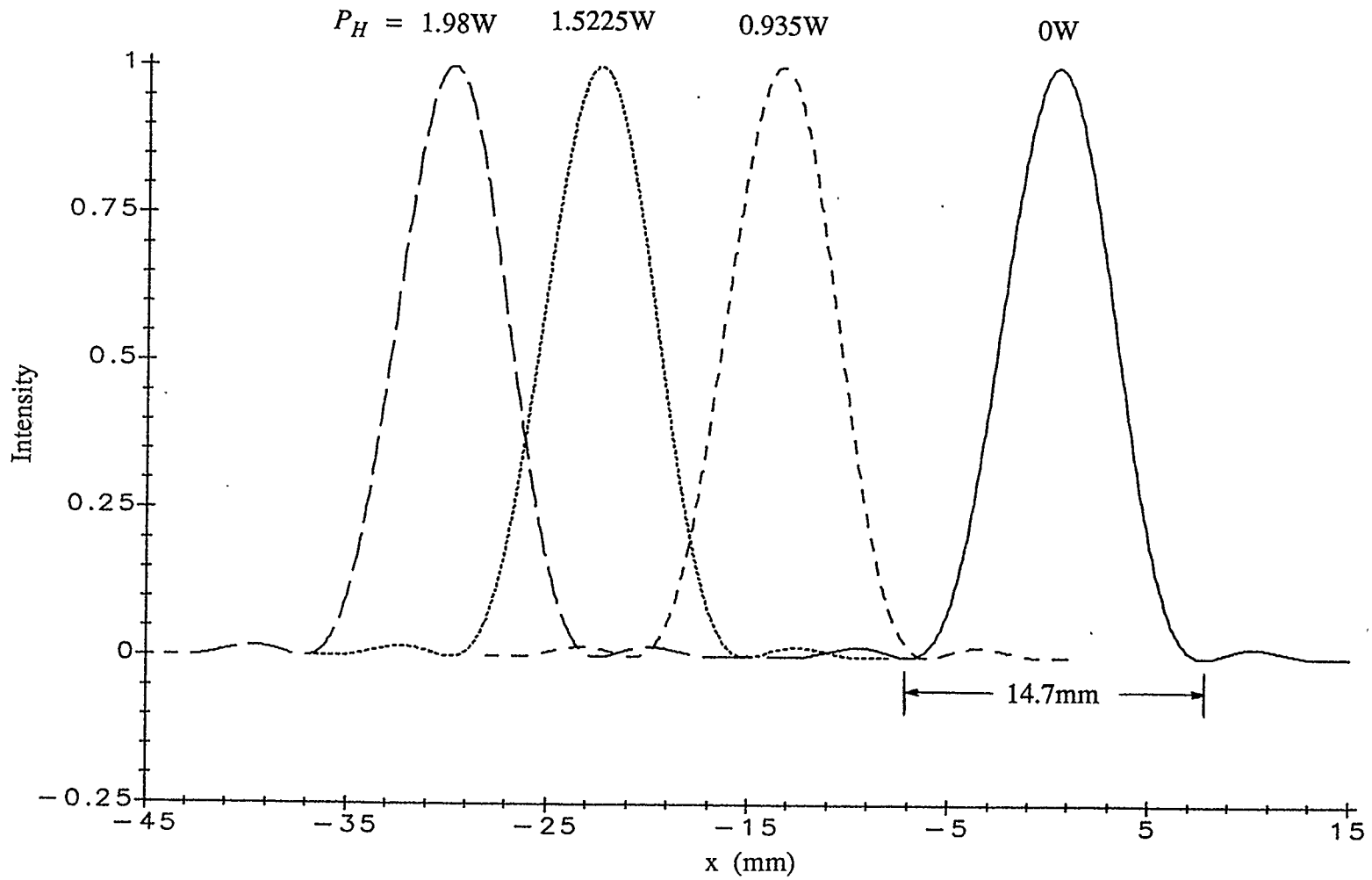

Figure 4.3 Intensity distribution for Fraunhofer diffraction for glass type SF11

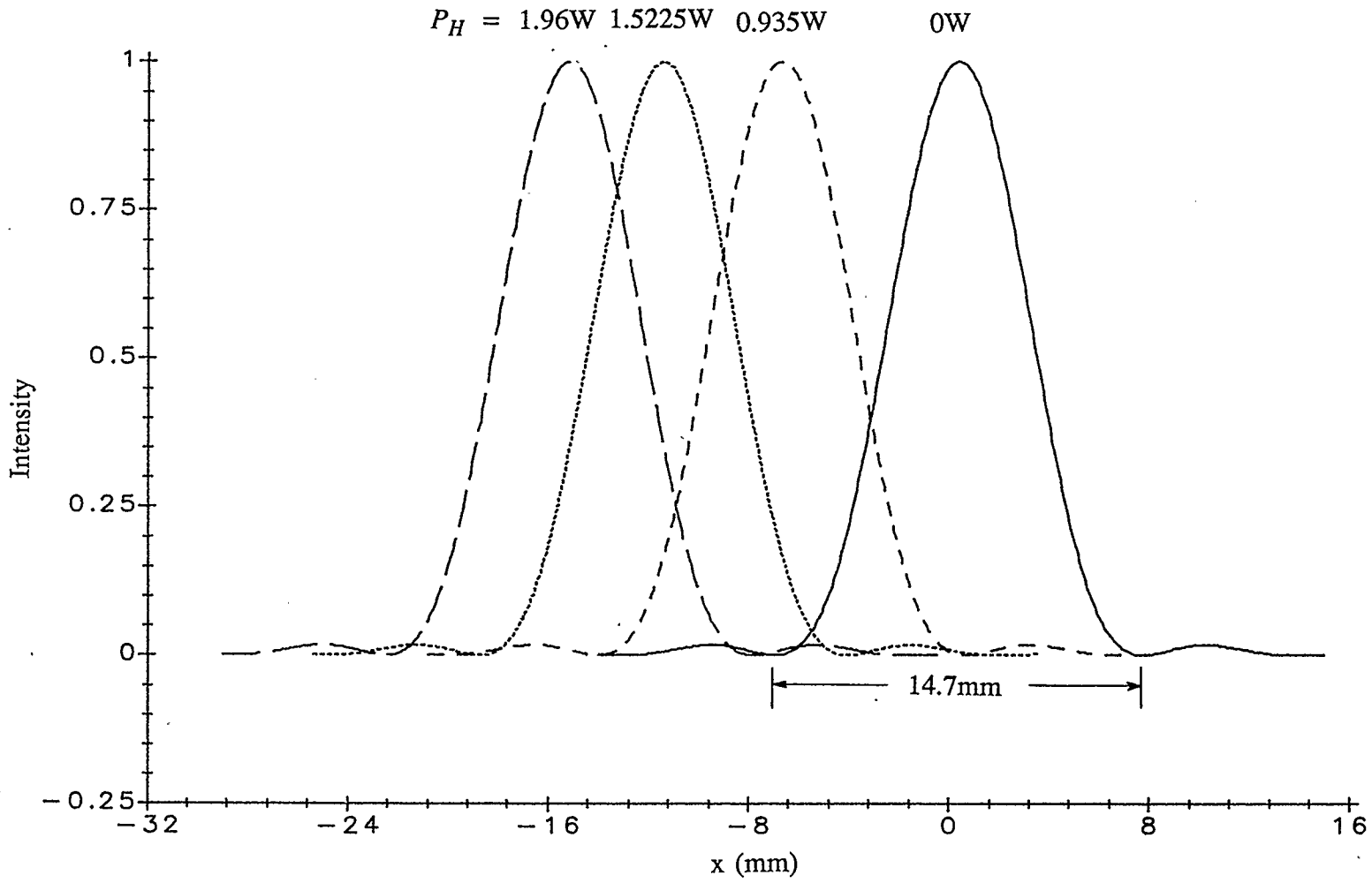

Figure 4.4 Intensity distribution for Fraunhofer diffraction for glass type SF13

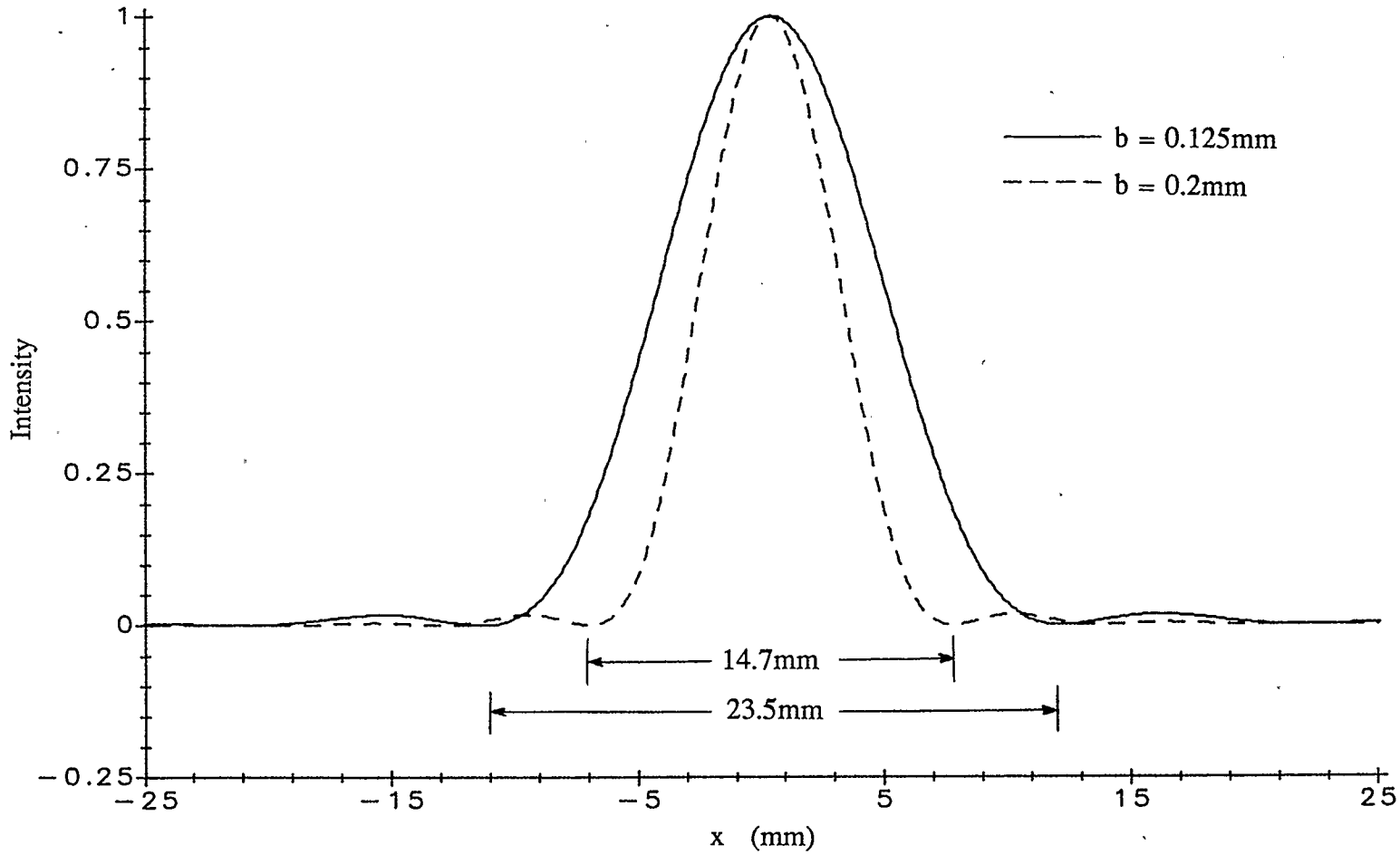

Figure 4.5 Effect of beamwidth on the diameter of the brightest ring for Fraunhofer diffraction pattern

$\tan^{-1}(\frac{14.7/2}{1860+24}) = .004$ rad where the glass length is 24mm. Theoretically θ_s is given by Equation (2.13) and is equal to .004018 rad for a beam diameter $b = 0.2$mm. Figure 4.5 shows that when $b = 0.125$mm the beam width at a distance of 1860mm from the glass increases to approximately 23.5mm which agrees with Equation (2.13) that the diameter of the bright ring is inversely proportional to the diameter of the aperture.

4.3. Temperature Analysis

The theoretical dc and pulsed responses of the switch for the heater power applied to the surface of the glass is examined by solving the two-dimensional equation of heat conduction using numerical method of analysis based on the finite difference techniques as described in Chapter 2 with $\Delta x = \Delta y = 0.1$mm and $\Delta t = 5$ms.

4.3.1. dc analysis

Figures 4.6 to 4.11 show the theoretical dc analysis for the glass type SF57 with heater width of 2mm and q'', the surface heat flux, corresponding to the applied heater power of 2W. The Figures are as a function of the duration of the applied heater power.

Figures 4.6 and 4.7 show respectively the temperature profile at the surface and at x = 0.3mm with respect to the width of the glass and duration of the applied

heater power. It is observed that for a given input power the surface temperature, the temperature at x = 0.3mm, and as a matter of fact, the temperature anywhere in the *xy* plane increases with time but the change in temperature with time, $\Delta T/\Delta t$, decreases and will eventually be zero, that is, the steady state temperature for the glass will be reached. It is also observed that the increase in temperature at any time is greater under the film heater which extends from y = 1.5mm to y = 3.5mm than at the sides which are exposed to the atmospheric temperature of 20°C. The maximum increase in temperature is at the center of the heater. The temperature profile under the center of the heater (y = 2.5mm) with respect to the depth *x* is shown in Figure 4.8. The temperature decreases with distance from the heater surface.

Figure 4.9 shows the variation of the temperature gradient dT/dx (dx being equal to 0.2mm, the input beam diameter at x = 0.3mm to x = 0.5mm) with respect to the width of the glass. The dT/dx increases with the duration of the applied power but the incremental change in dT/dx with time decreases. The Figure also shows that the maximum dT/dx for any time is confined beneath the center of the heater surface. For any duration of the applied heater power the temperature gradient is approximately constant under the center of the heater surface for a beam width of 0.2mm thus giving the same amount of deflection for all portions of the beam. If the input beam diameter is comparable to the heater width the temperature gradient on the sides of the beam will be less than at its center resulting in an elliptical deflected beam [10].

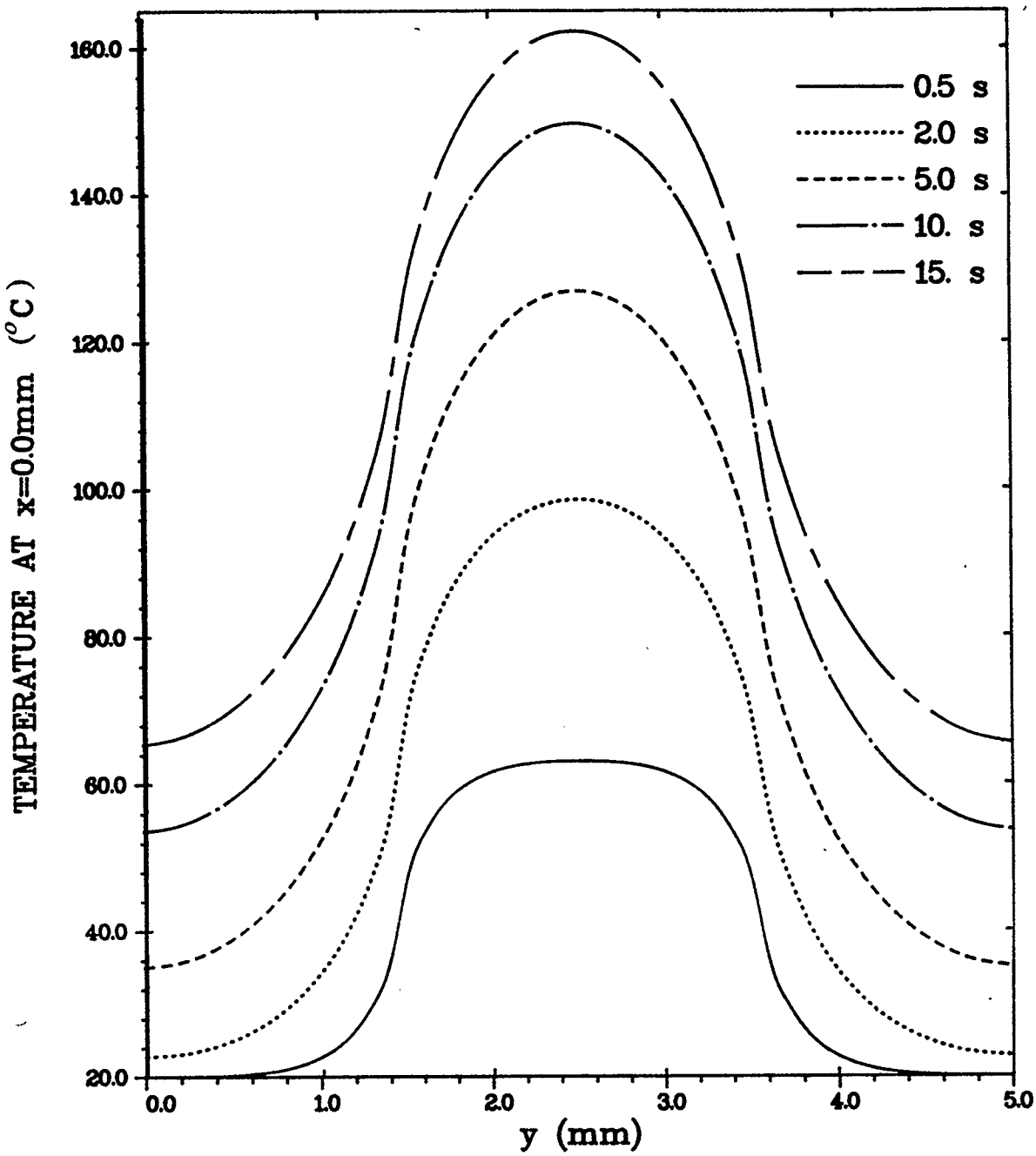

FIGURE 4.6 SURFACE TEMPERATURE vs GLASS WIDTH AS A FUNCTION OF TIME FOR SF57 AT P_H=2W

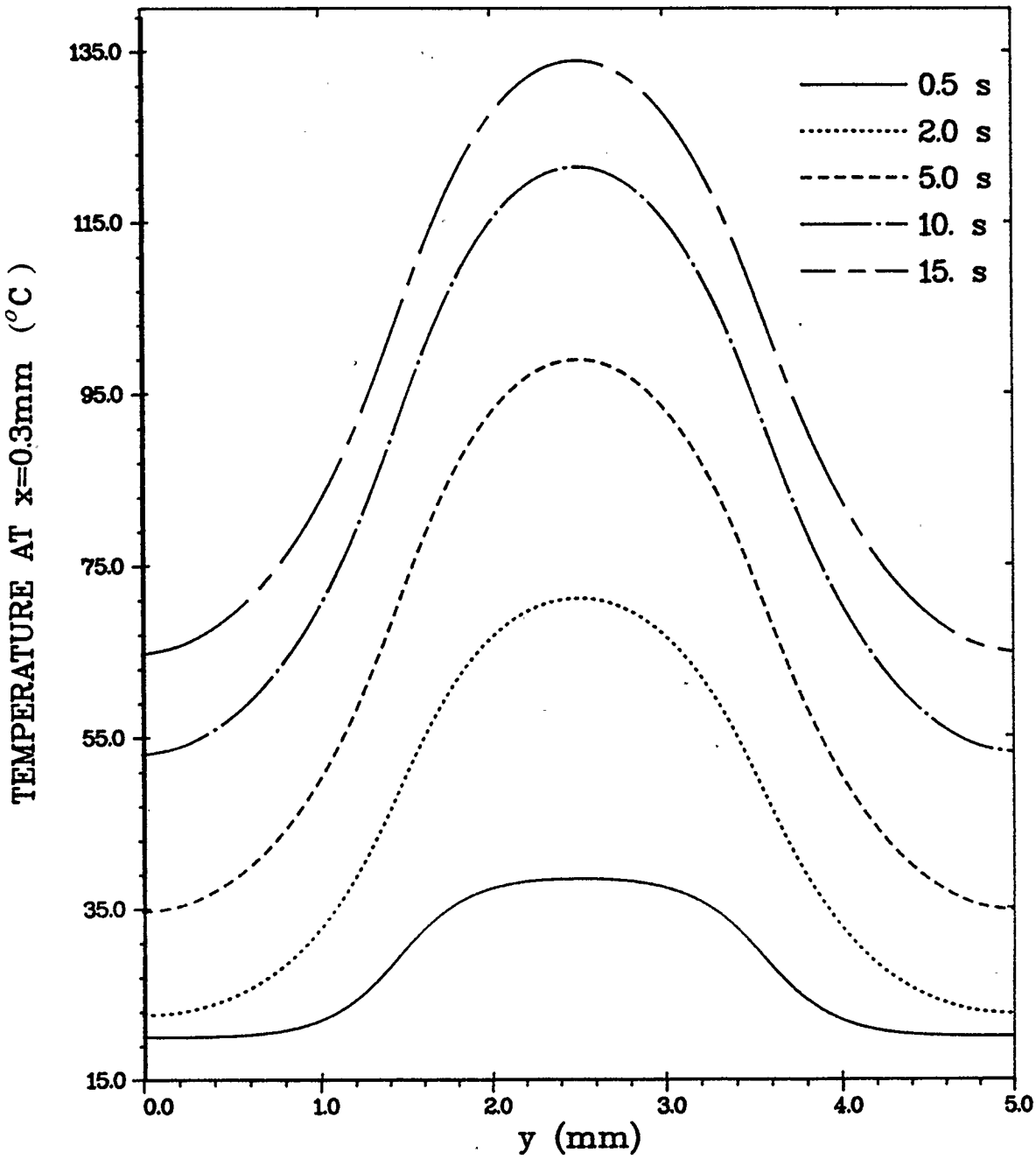

FIGURE 4.7 TEMPERATURE AT x=0.3mm vs GLASS WIDTH AS A FUNCTION OF TIME FOR SF57 AT P_H=2W

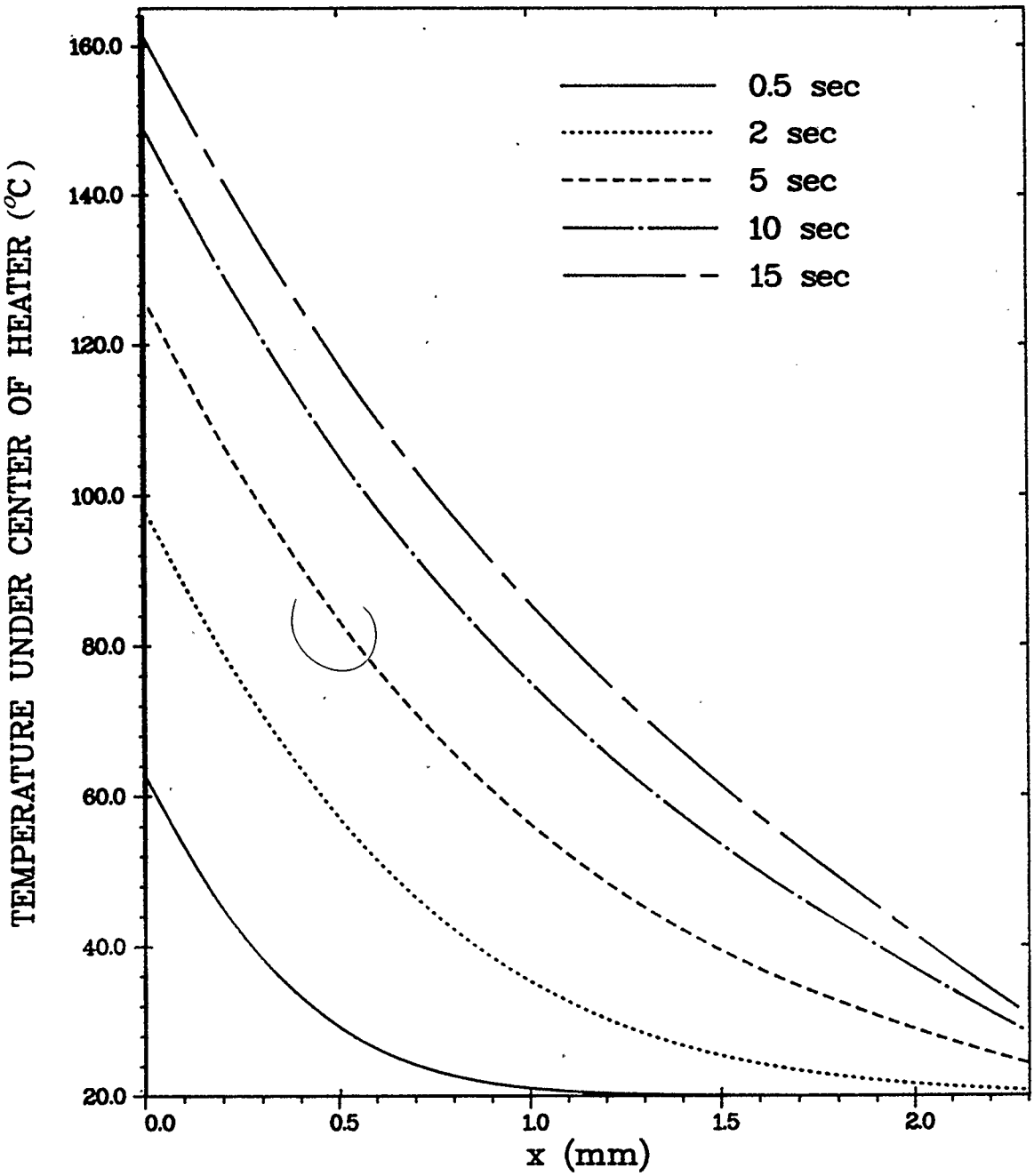

FIGURE 4.8 TEMPERATURE AS A FUNCTION OF DEPTH AND TIME FOR SF57 AT P_H=2W

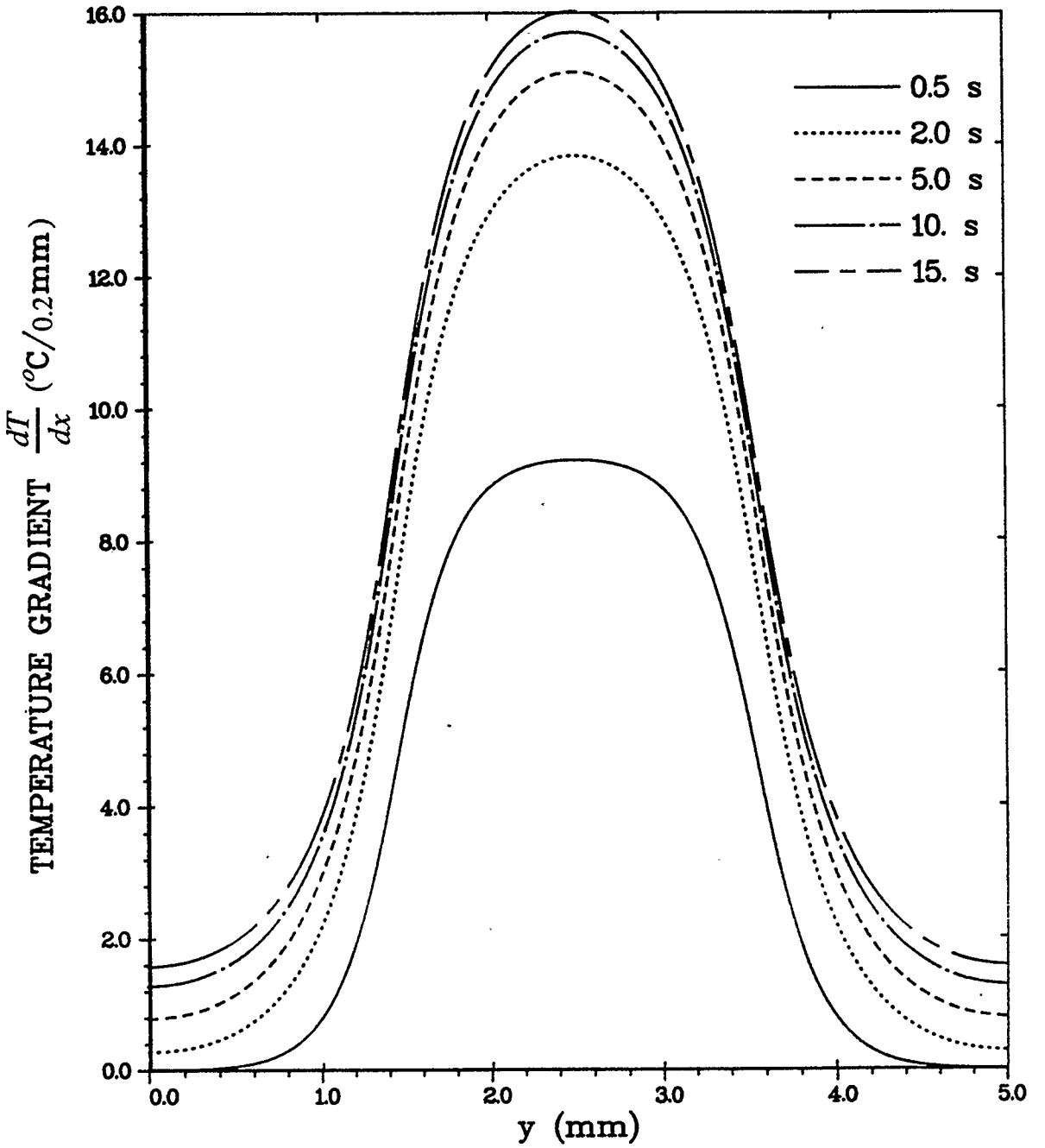

FIGURE 4.9 TEMPERATURE GRADIENT (x=0.3mm TO x=0.5mm) AS A FUNCTION OF WIDTH AND TIME FOR SF57 AT P_H=2W

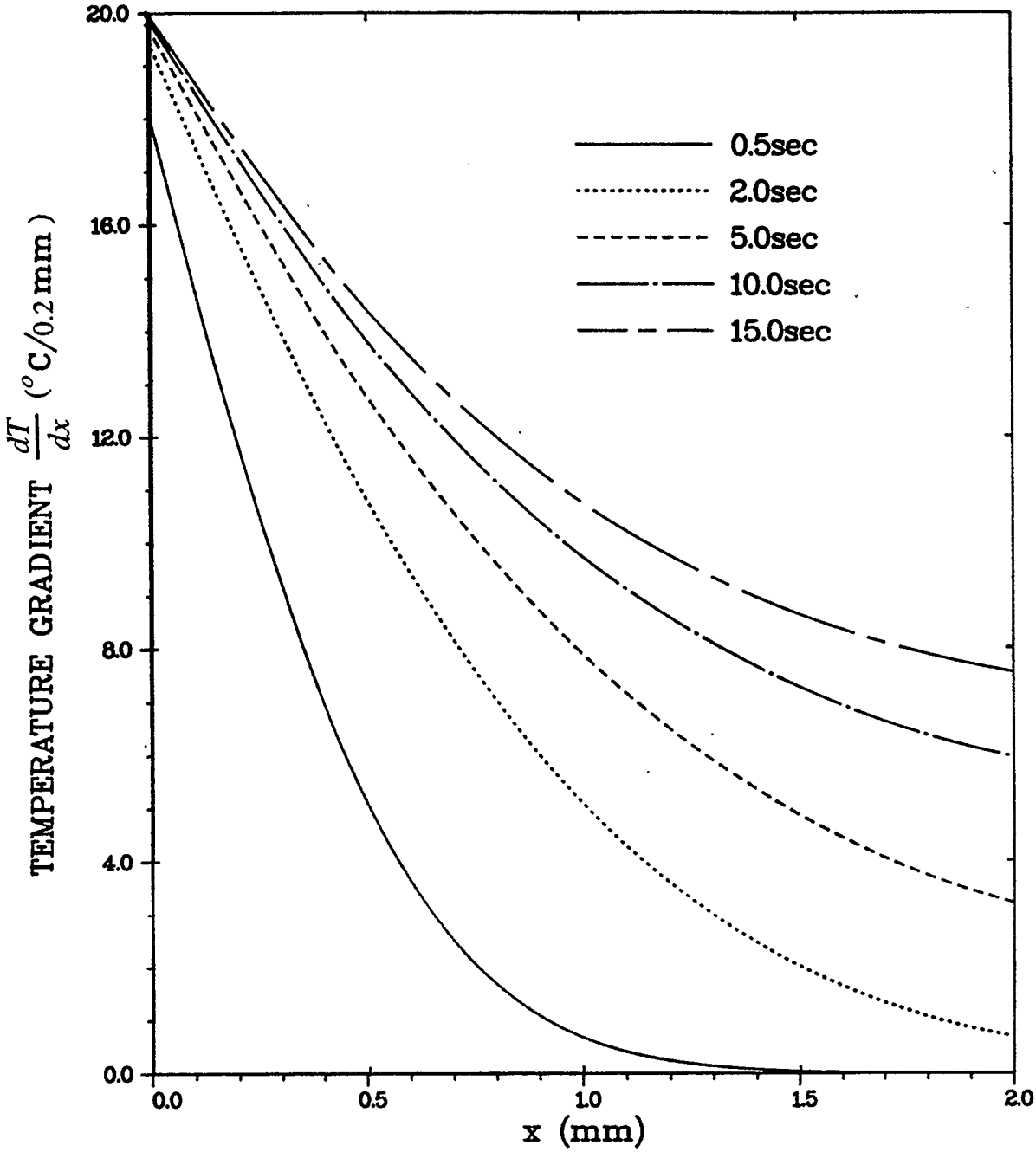

FIGURE 4.10 TEMPERATURE GRADIENT UNDER CENTER OF HEATER AS A FUNCTION OF DEPTH AND TIME FOR SF57 AT P_H=2W

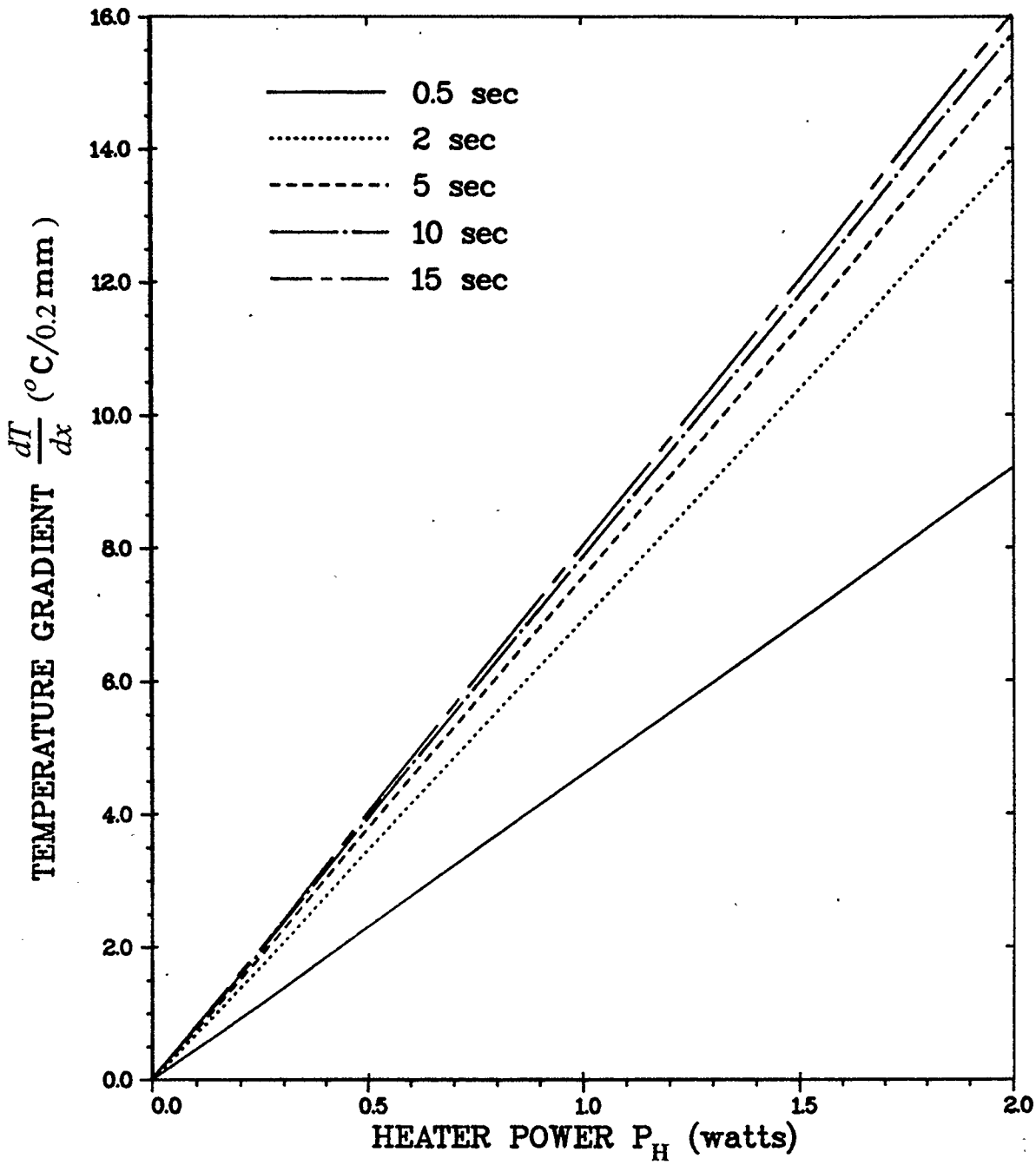

FIGURE 4.11 TEMPERATURE GRADIENT AS A FUNCTION OF HEATER POWER AND TIME FOR SF57

The variation of the temperature gradient dT/dx (dx = 0.2mm) with depth x is shown in Figure 4.10 where x denotes the top of the 0.2mm diameter beam. As x is increased $\frac{dT}{dx}$ decreases and since $\theta_D \propto \frac{dT}{dx}$ (from Equation (2.14)) the maximum deflection is obtained when the incident beam is confined near the glass surface. Therefore, in view of the importance of obtaining maximum deflection it is essential that the beam be incident

(1) under the center of the heater (from Figure 4.9)

(2) and close to the glass surface (from Figure 4.10)

Figure 4.11 shows the variation of the temperature gradient dT/dx with heater power for different times after the input heater power is applied (dx being equal to 0.2mm, beam diameter from x = 0.3mm to x = 0.5mm). The temperature gradient dT/dx and as a result the deflection angle θ_D increases with heater power.

4.3.1.1. Temperature analysis for constant heater power density

The temperature gradient is observed not to increase to a large extent after 10sec of applied heater power. Therefore, Figures 4.12 to 4.16 are plotted after a duration of 10sec of the applied heater power.

It can be shown from Equations (2.14) and (2.16) that $\theta_D \simeq \frac{l}{k}\frac{P_H}{A}(\frac{dn}{dT})$ where P_H/A is the heater power density. Figures 4.12 to 4.16 compare the temperature analysis for different types of glasses at constant heater power density of 67227W/m^2. Figures 4.12 and 4.13 show respectively the temperature profiles

at the surface and at x = 0.3mm with respect to the glass width for all the four types of Schott glasses considered. Due to the thermal conductivity k being the least for SF59 (as given in Table 2.1) among the four types of glasses, it has the highest surface temperature and temperature at x = 0.3mm at the center of the heater. SF57, SF11 and SF13 come next in order depending on their thermal conductivities. The thermal heat capacity, ρc, for SF57 is highest, meaning that more of the energy moving through the material is absorbed, thus less energy is available for further transfer. Therefore, the temperature rise at y = 0mm and y = 5mm is the least of all the four glasses as shown in Figures 4.12 and 4.13.

Figure 4.14 shows the variation of the temperature under the center of the heater (y = 2.5mm) as a function of depth x for different types of glasses at constant heater power density. SF59 has the highest slope due to the fact that its k is the least of all the four glasses. SF13 has the highest value of k, thus its slope is the least at all points along the x-axis. The variation of temperature gradient at x = 0.3mm to x = 0.5mm with respect to the width y of the glass is shown in Figure 4.15 for different types of the Schott glasses considered. The variation of the temperature gradient dT/dx (dx = 0.2mm) under the center of heater as a function of depth x is shown in Figure 4.16. For all the types of glasses the gradient is maximum at the center along the width and decreases with depth. It is also observed that SF59 has the maximum gradient along both the width and depth of the glass and that it has the maximum slope.

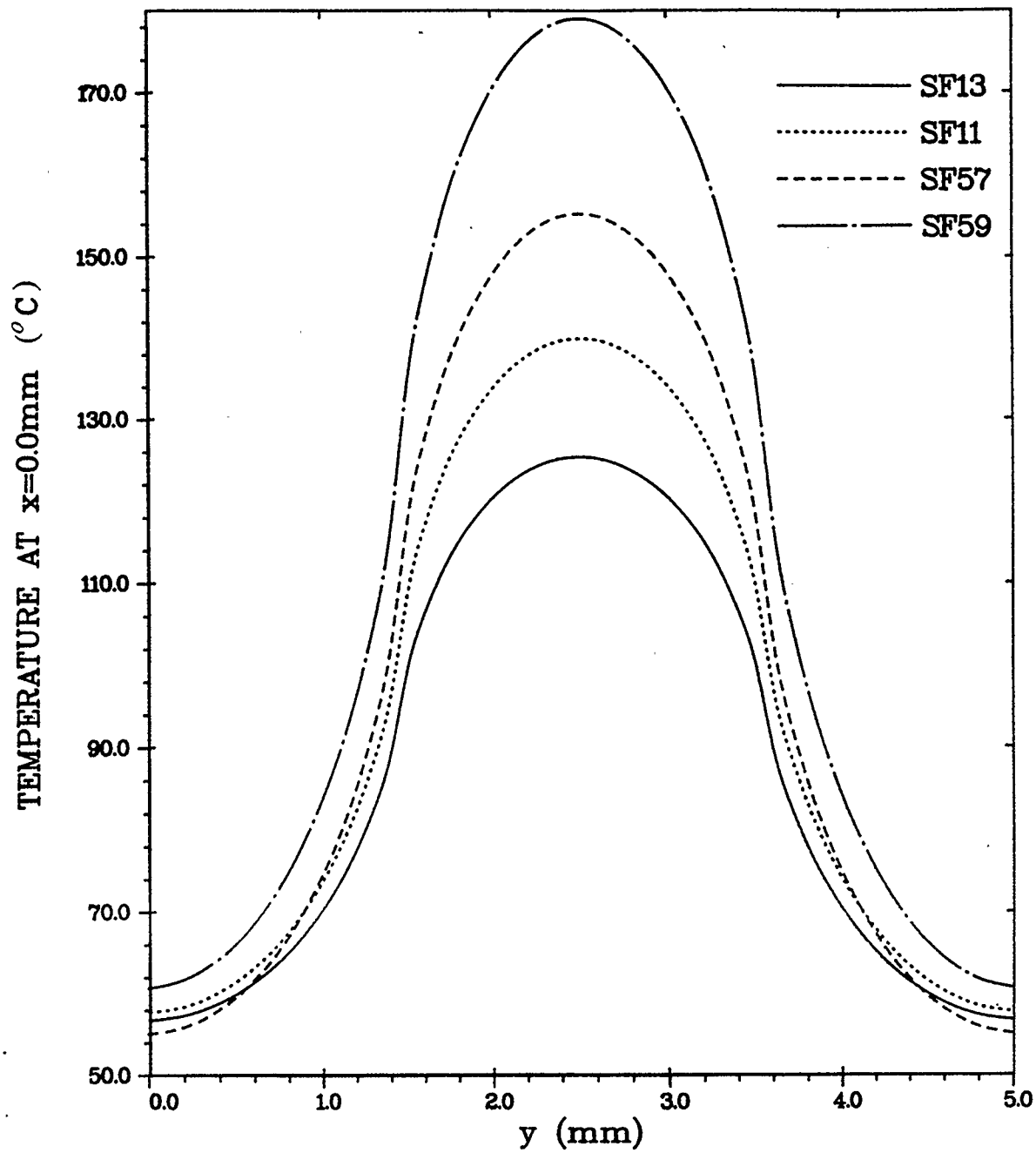

FIGURE 4.12 SURFACE TEMPERATURE vs GLASS WIDTH AS A FUNCTION OF TYPE OF GLASS AT CONSTANT HEATER POWER DENSITY

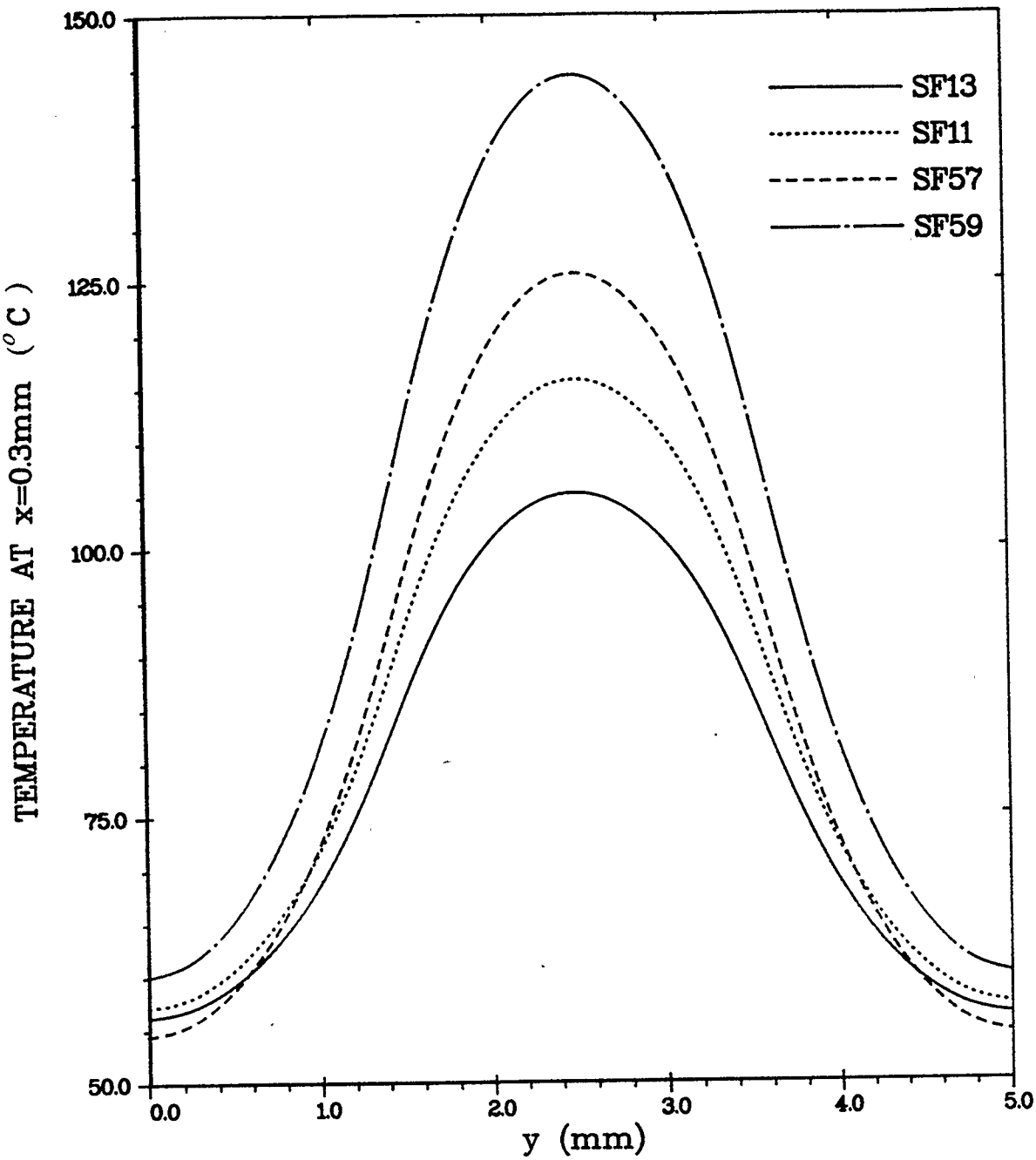

FIGURE 4.13 TEMPERATURE AT x=0.3mm vs GLASS WIDTH AS A FUNCTION OF TYPE OF GLASS AT CONSTANT HEATER POWER DENSITY

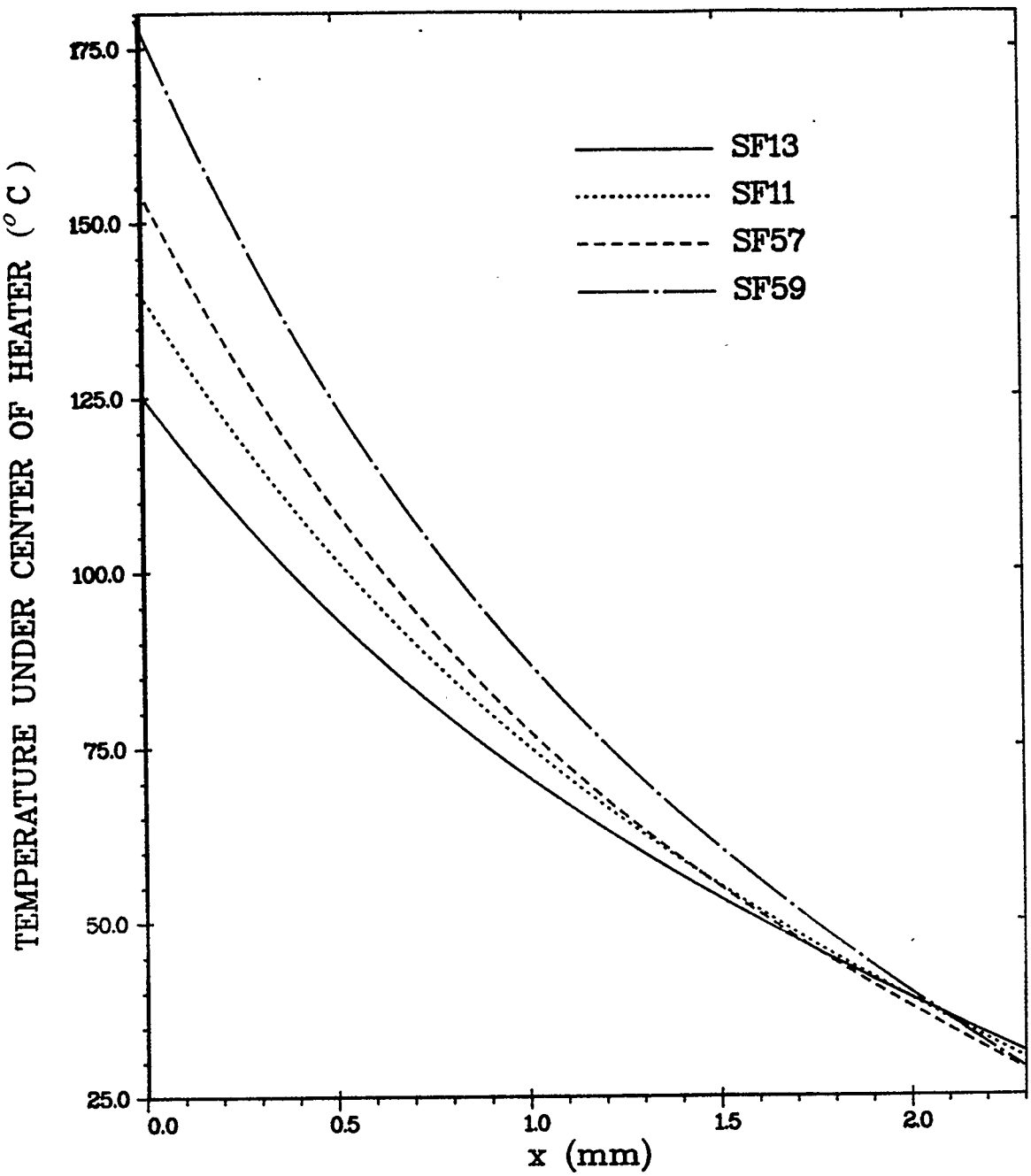

FIGURE 4.14 TEMPERATURE AS A FUNCTION OF DEPTH AND TYPE OF GLASS AT CONSTANT HEATER POWER DENSITY

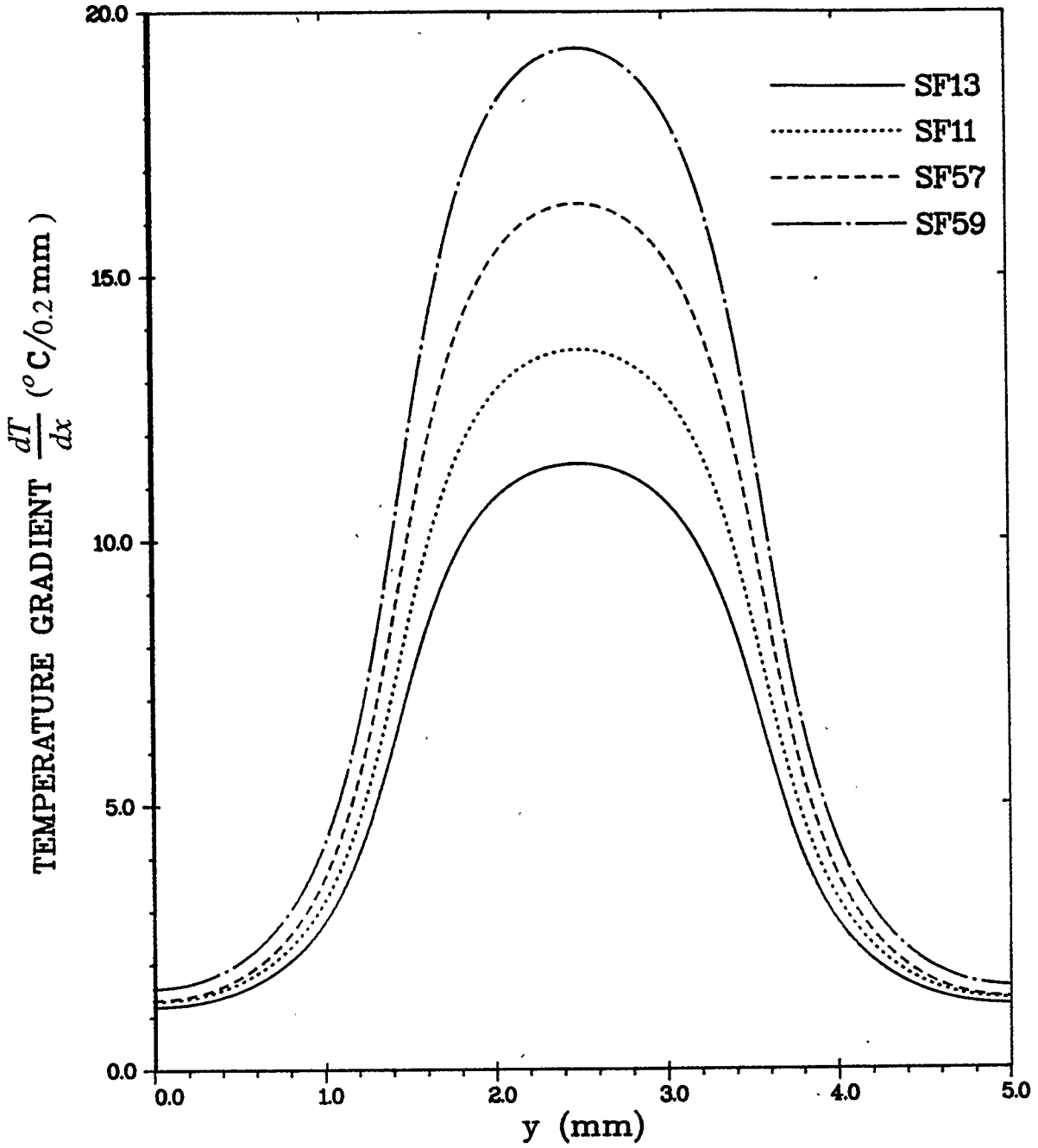

FIGURE 4.15 TEMPERATURE GRADIENT (x=0.3mm TO x=0.5mm) AS A FUNCTION OF WIDTH AND TYPE OF GLASS AT CONSTANT HEATER POWER DENSITY

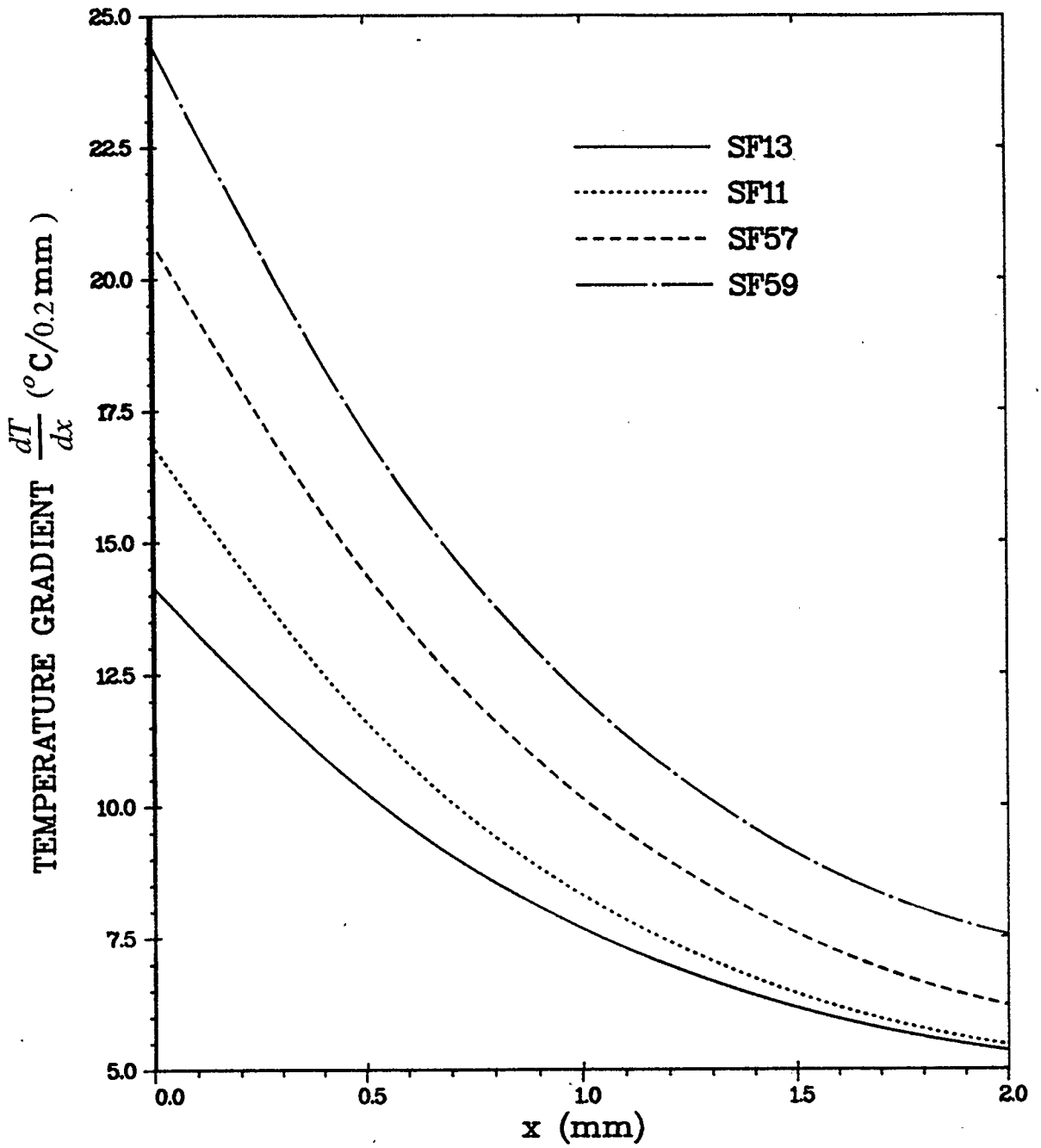

FIGURE 4.16 TEMPERATURE GRADIENT UNDER CENTER OF HEATER AS A FUNCTION OF DEPTH AND TYPE OF GLASS AT CONSTANT HEATER POWER DENSITY

4.3.1.2. Temperature analysis for constant heater power

Figures 4.17 through 4.21 show the temperature analysis for different types of glasses at constant heater power P_H of 2W after a duration of 10sec of the applied heater power. The temperature analysis at constant heater power is done because the heater areas fabricated differ slightly for the different types of glasses as shown in Table 3.1. The value of the surface heat flux $q'' = \frac{P_H}{A}$ is now different for all glasses.

Figures 4.17 and 4.18 show respectively the surface temperature and temperature at x = 0.3mm with respect to the glass width. SF57 now shows the maximum value of the temperature reached instead of SF59 as shown in Figures 4.12 and 4.13. The temperature profile under the center of heater as a function of depth is shown in Figure 4.19. It is no longer the same as that for constant heater power density. SF57 and SF59 have approximately equal slopes with SF13 having the least slope. Figure 4.20 shows the temperature gradient (x = 0.3mm to x = 0.5mm) as a function of width y and type of glass. The variation of the temperature gradient under the center of heater as a function of depth x is shown in Figure 4.21. The temperature gradient for SF57 is maximum instead of SF59 for constant heater power density case.

Figures 4.22 and 4.23 compare dT/dx for different Schott glasses with respect to heater power density and heater power. For the same heater power, Figure 4.23 shows that SF57 has a larger dT/dx than SF59 due to its heater power density

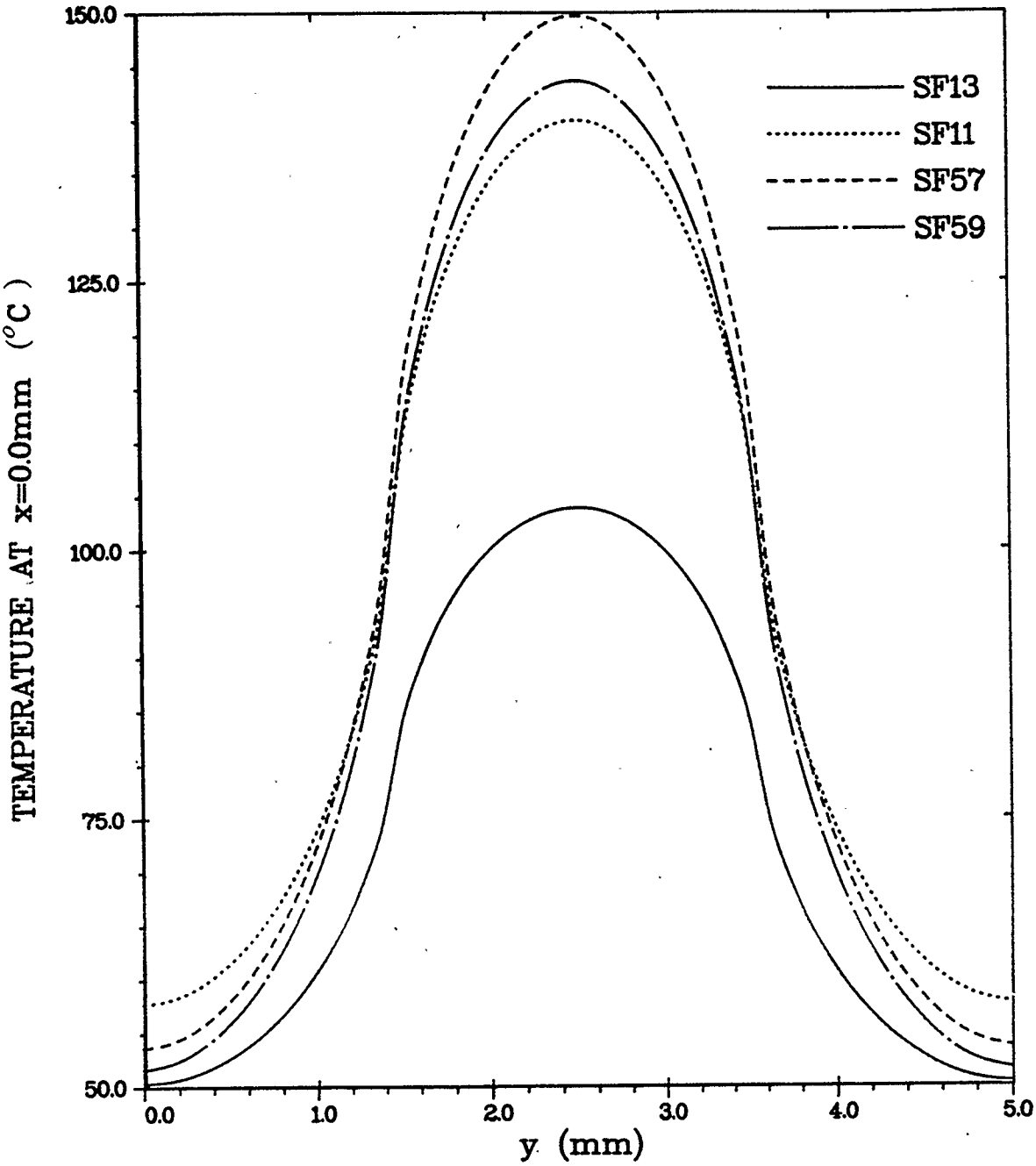

FIGURE 4.17 SURFACE TEMPERATURE vs GLASS WIDTH AS A FUNCTION OF TYPE OF GLASS AT P_H=2W

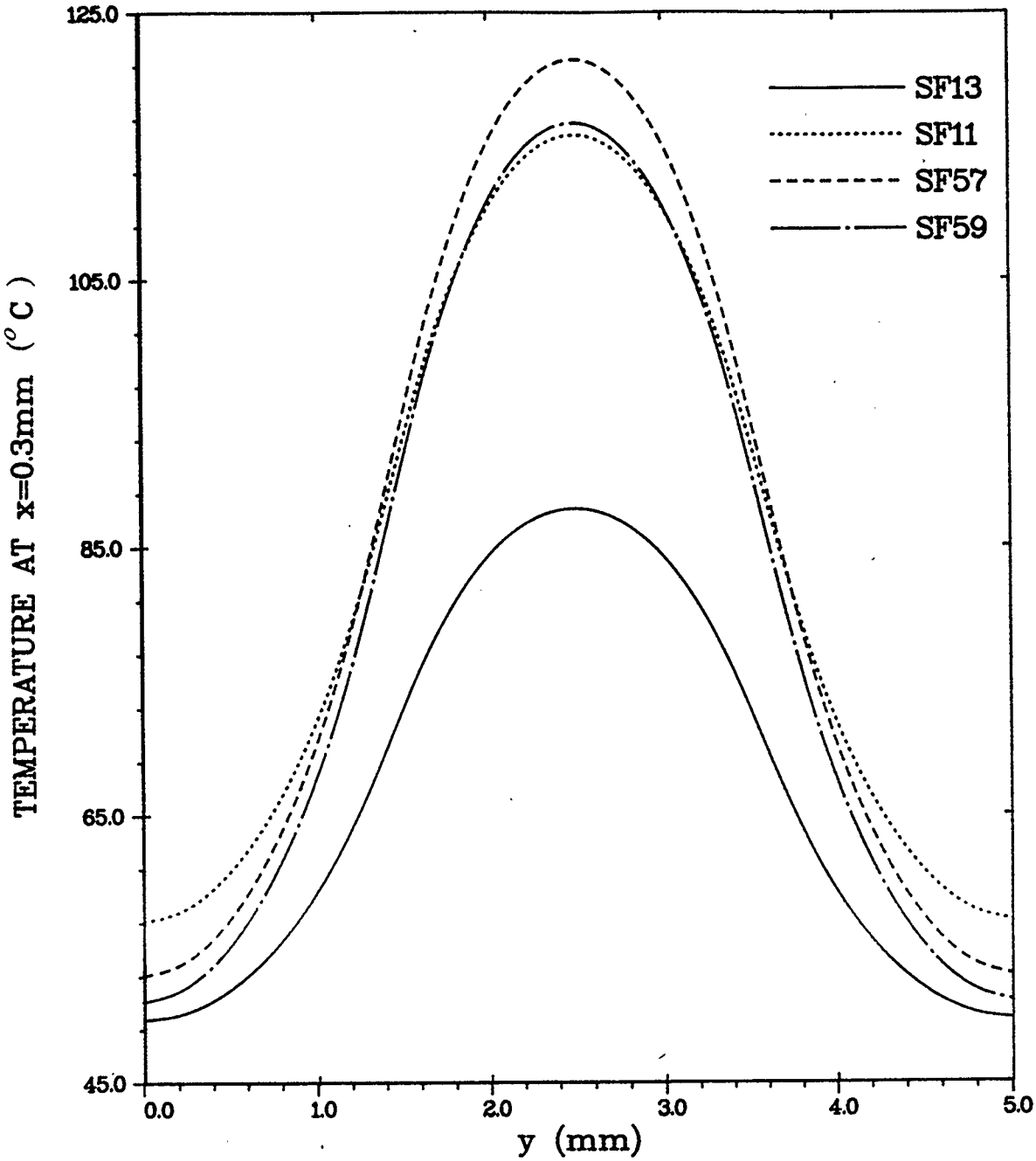

FIGURE 4.18 TEMPERATURE AT x=0.3mm vs GLASS WIDTH AS A FUNCTION OF TYPE OF GLASS AT P_H=2W

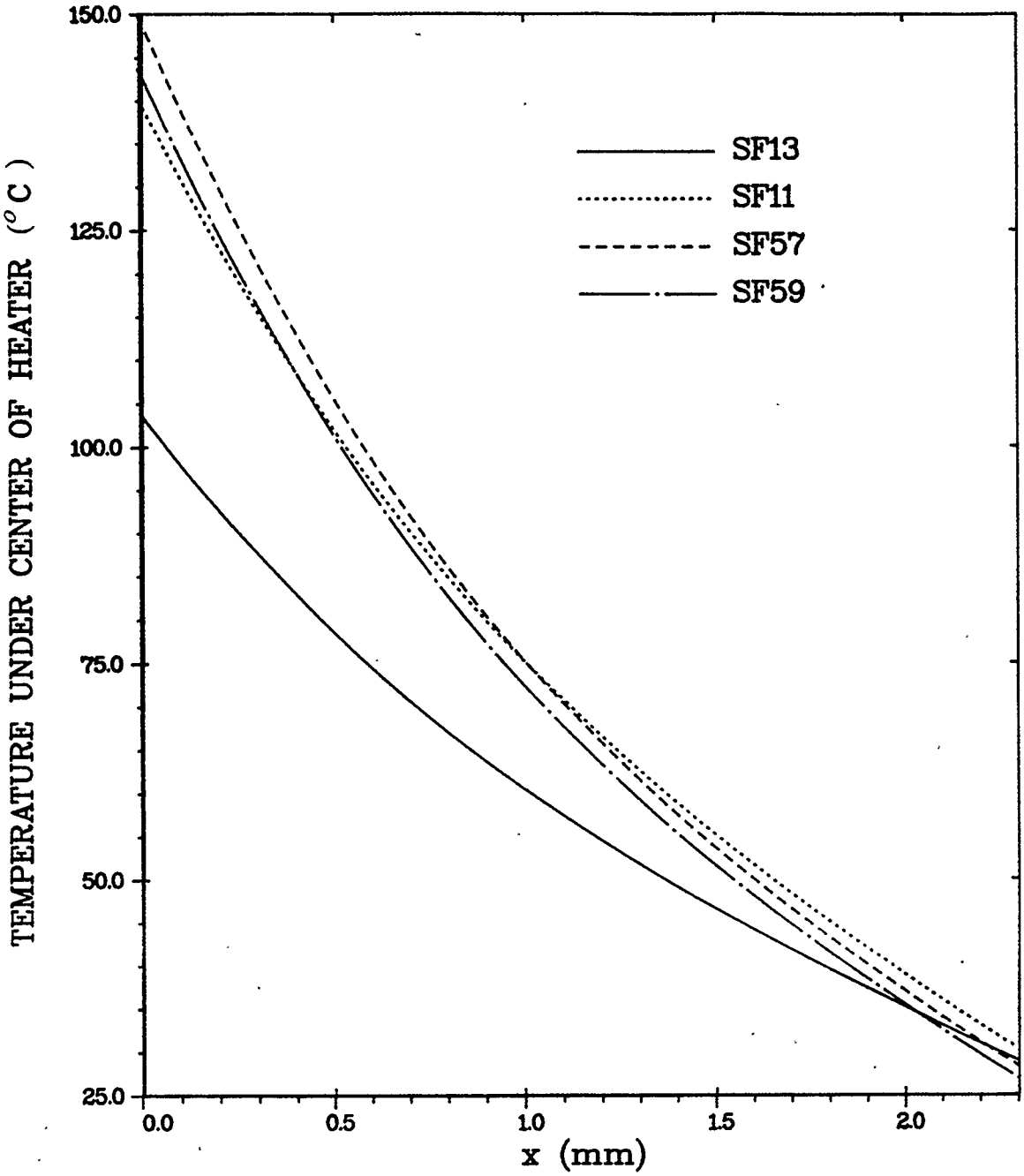

FIGURE 4.19 TEMPERATURE AS A FUNCTION OF DEPTH AND TYPE OF GLASS AT P_H=2W

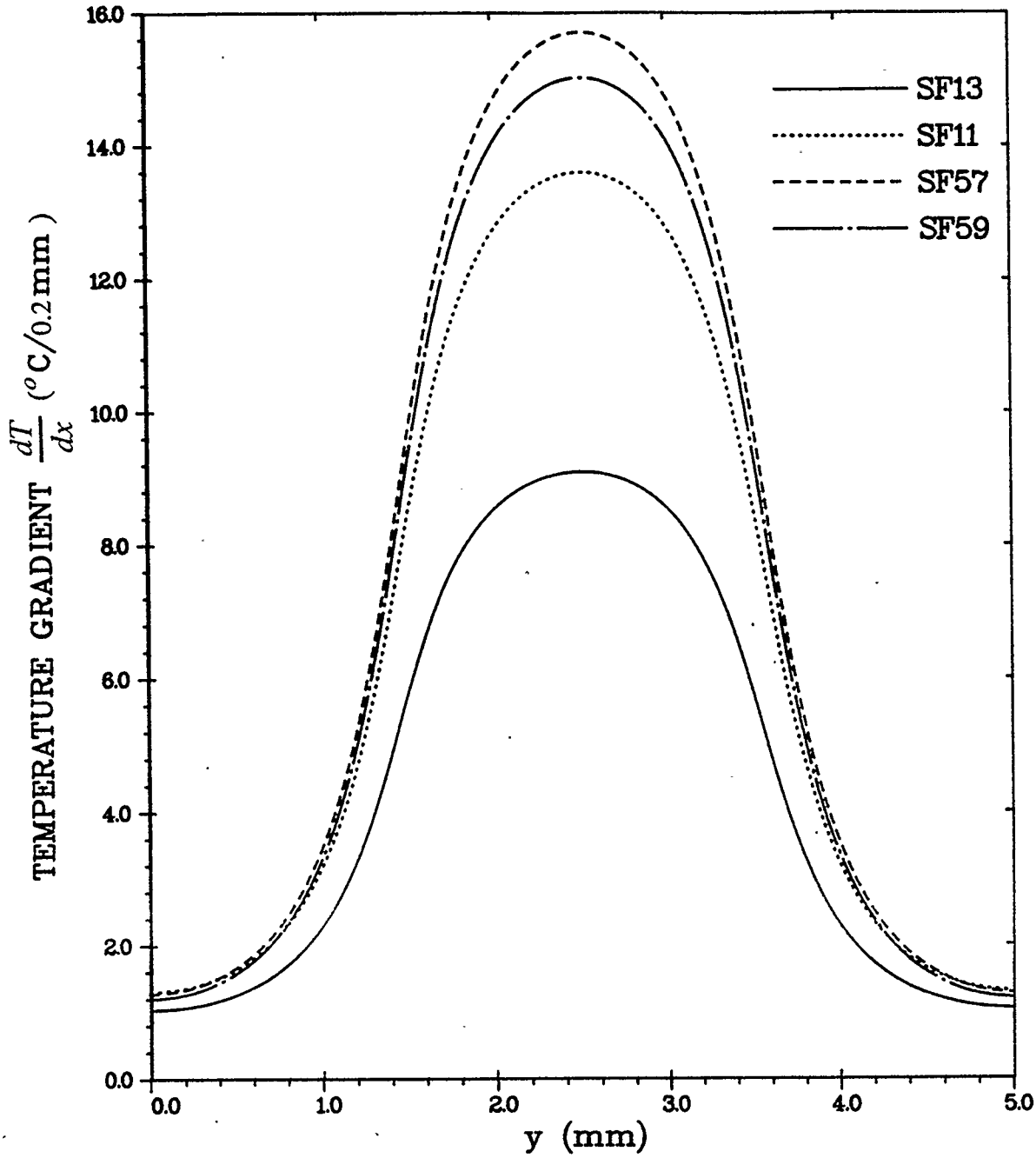

FIGURE 4.20 TEMPERATURE GRADIENT (x=0.3mm TO x=0.5mm) AS A FUNCTION OF WIDTH AND TYPE OF GLASS AT P_H=2W

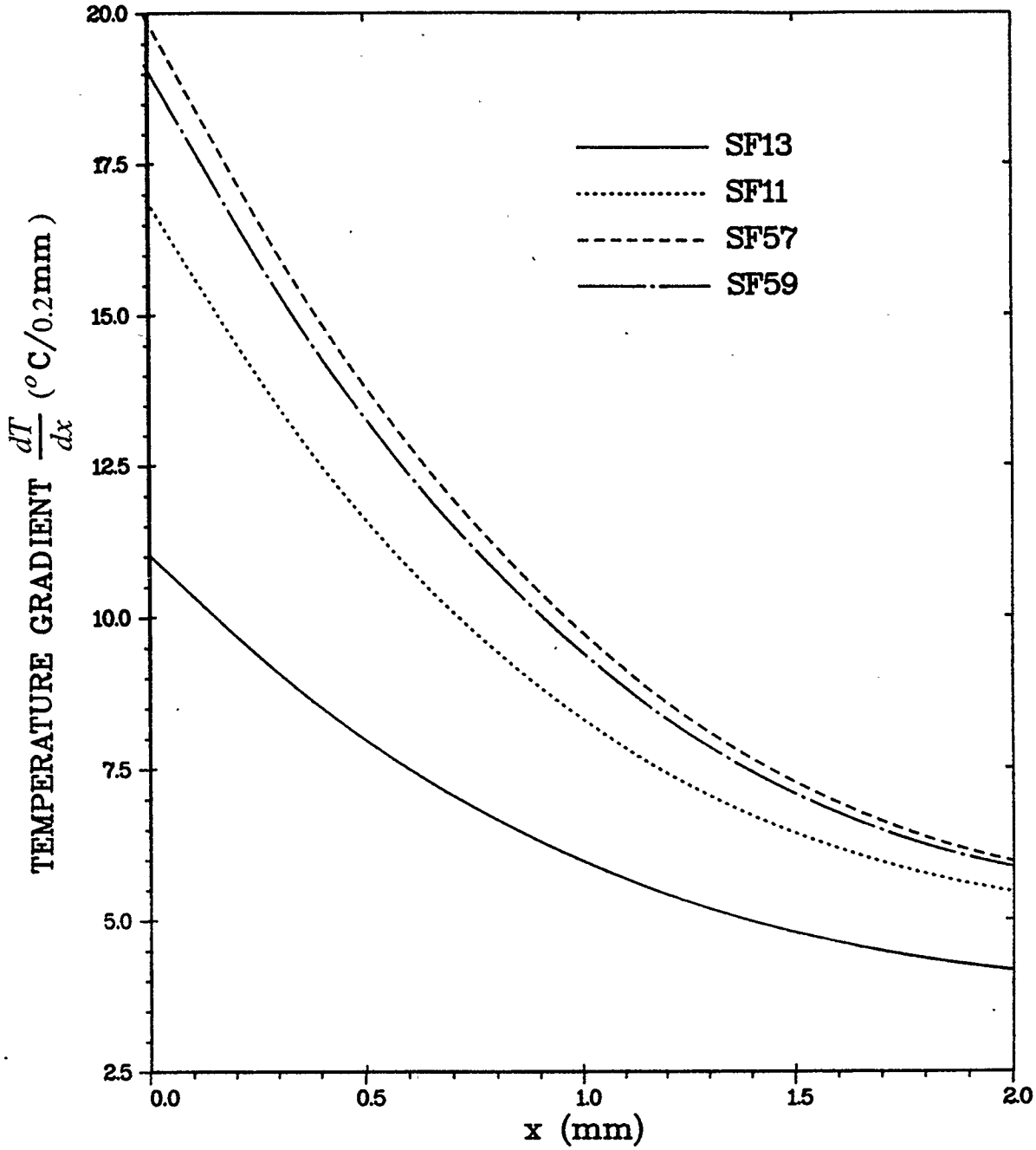

FIGURE 4.21 TEMPERATURE GRADIENT UNDER CENTER OF HEATER AS A FUNCTION OF DEPTH AND TYPE OF GLASS AT P_H=2W

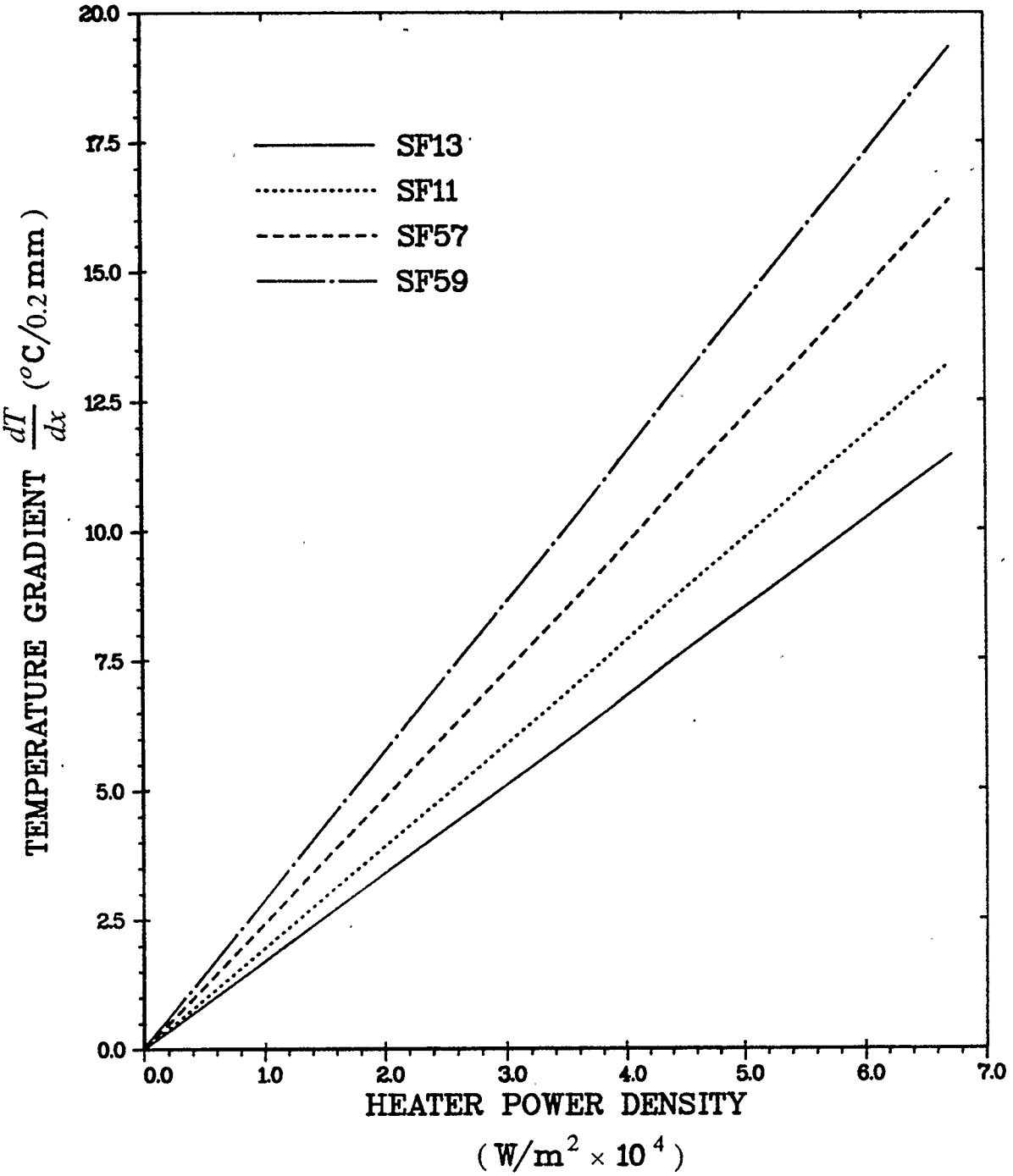

FIGURE 4.22 TEMPERATURE GRADIENT vs HEATER POWER DENSITY FOR DIFFERENT GLASSES AFTER 10sec

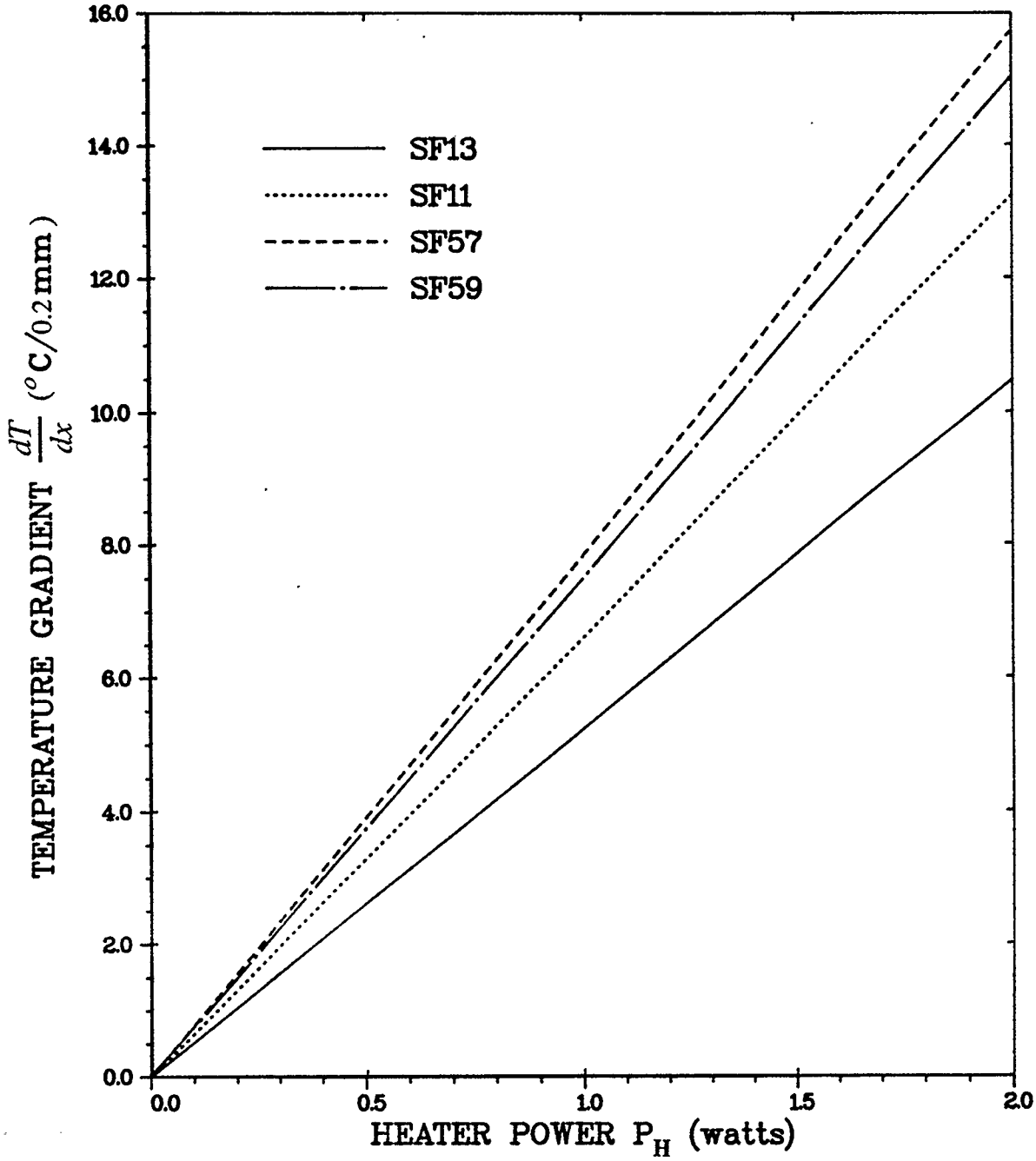

FIGURE 4.23 TEMPERATURE GRADIENT vs HEATER POWER FOR DIFFERENT GLASSES AFTER 10sec

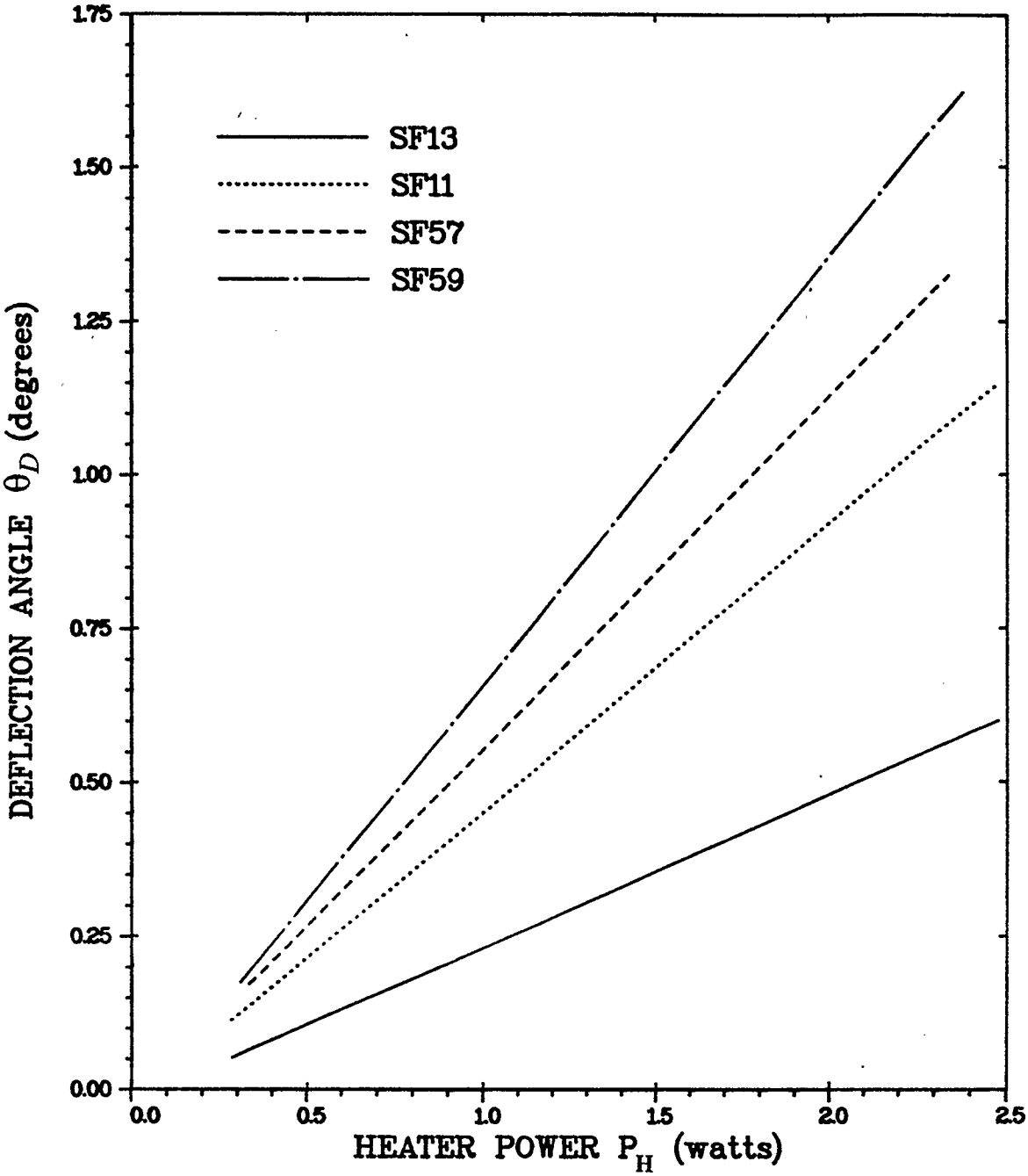

FIGURE 4.24 DEFLECTION ANGLE θ_D vs HEATER POWER P_H

being greater than SF59 at $P_H = 2$W. To be exact, the temperature gradient depends critically on the heater area and Figure 4.22 shows that for similar power densities SF59 has a larger dT/dx than all other glass types considered. It is also observed that the variation of dT/dx with heater power or heater power density is linear for all the glass types and since $\theta_D \propto$ dT/dx its variation with heater power should also be linear. Figure 4.24 shows such a variation of θ_D with heater power. Even though SF57 has a larger dT/dx than SF59 the deflection angle of SF59 is higher than SF57 since it has a much larger dn/dT. SF57 has a larger θ_D than SF11 due to its dT/dx being much greater than SF11. SF13 shows the least amount of deflection among the four glass types. It is observed from Figure 4.24 that $d\theta_D/dP_H$ is linear for all glasses where $d\theta_D/dP_H$ may be thought of as a figure of merit for the switch. The theoretical figure of merit as obtained from Figure 4.24 varies from 0.254^o/watt for SF13 to 0.691^o/watt for SF59.

4.3.2. Pulsed switch operation

Figures 4.25 to 4.29 show the pulse analysis of the device with a heater power pulse width of 0.5sec and a pulse period of 3.0sec. Figures 4.25 to 4.28 show the response of temperature gradient with time for SF59, SF57, SF11 and SF13 respectively for different heater powers (heater area being constant for a given glass sample). It is noted that for all the glass types dT/dx is zero for the first few increments of Δt and also that its maximum value does not occur at the instant the heater power is switched off. This is due to the fact that it takes a finite

time for the heat to flow from the surface to x = 0.3mm. The temperature gradient $\left.\frac{dT}{dx}\right|_s$ corresponding to the time taken to travel the distance s at which the fibre is placed at the output end (as shown in Figure 3.6 in Section 3.4) can be obtained from these Figures. The rise time of the switch is the time corresponding to $\left.\frac{dT}{dx}\right|_{h_f}$. Since $\left.\frac{dT}{dx}\right|_{h_f}$ remains constant for one type of glass and for one position of output fibre, it is observed from Figures 4.25 to 4.28 that the rise time decreases as the heater power is increased, that is, the required dT/dx is reached earlier for higher heater power levels. It is also observed that $\left.\frac{dT}{dx}\right|_d$ or deflection d, where $\left.\frac{dT}{dx}\right|_d$ is shown in the Figures for $P_H = 2$W, increases for increased power levels. Therefore, when the input heater power is off after 0.5 sec, the beam has to travel a greater distance $d - h_f$ before it can again be detected by the fibre in position 1. Therefore the delay time increases as heater power is increased. It is also obvious from the Figures that fall time increases with increased heater power and that fall time is greater than rise time.

Figure 4.29 compares the time responses for different glasses at similar power density. Since the dT/dx required for the beam to travel the distance h_f is inversely proportional to dn/dT (from Equation (3.1)), it is obvious that SF59 and SF13 require the lowest and the highest $\left.\frac{dT}{dx}\right|_{h_f}$ respectively. Therefore, from Figure 4.29, SF59 and SF13 show the minimum and maximum rise time respectively. Similarly

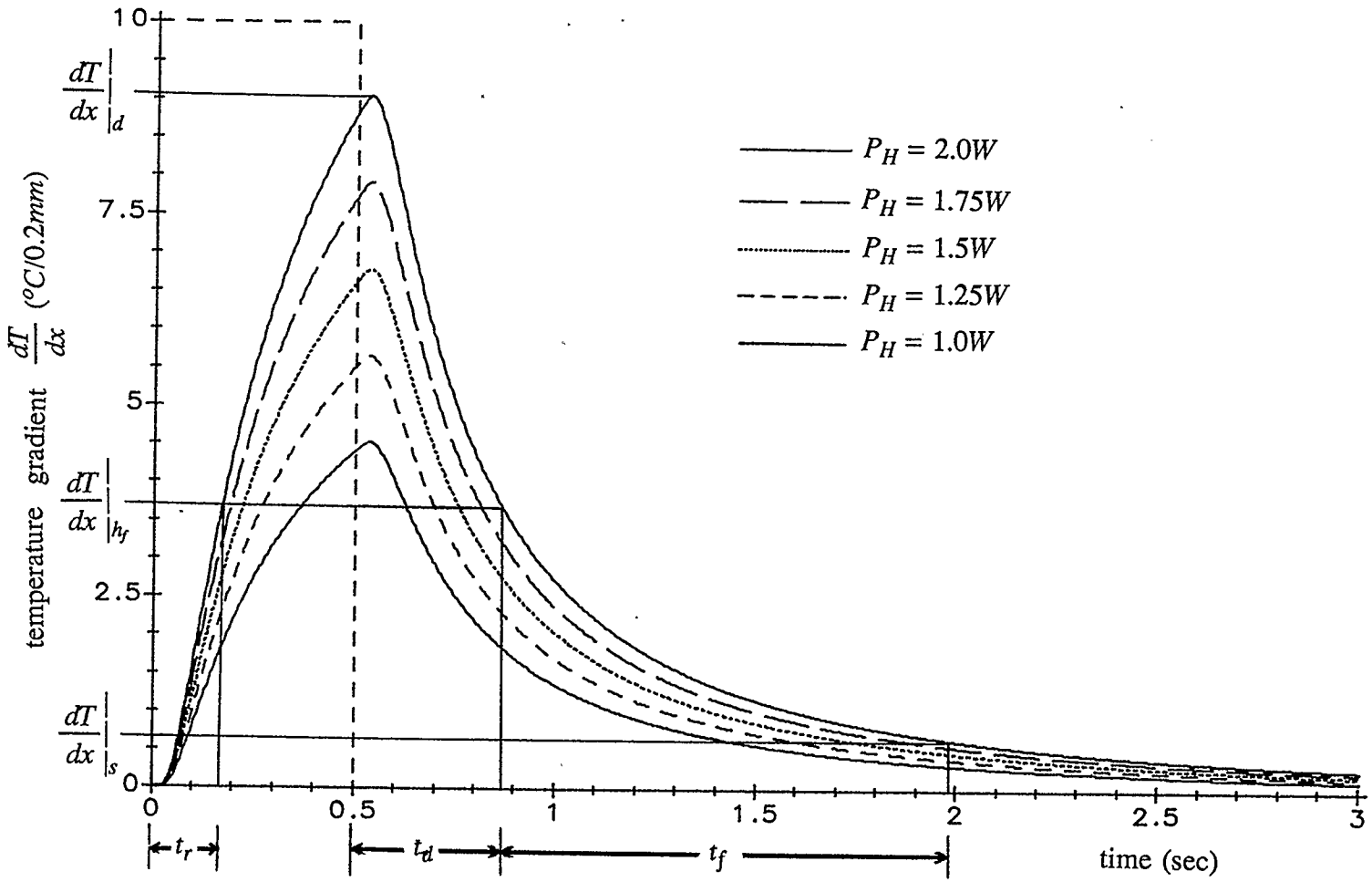

Figure 4.25 Temperature gradient vs time for SF59 at different heater powers

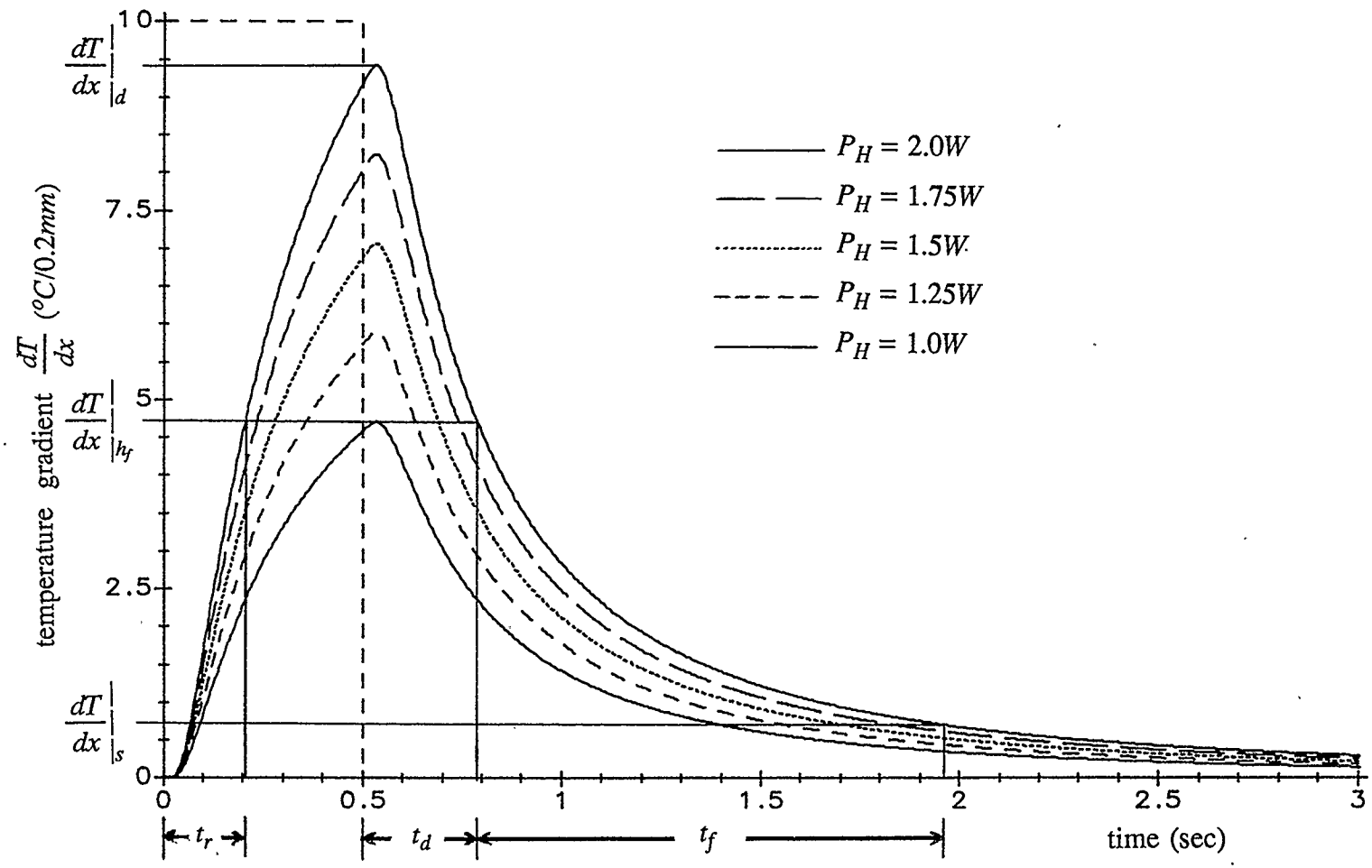

Figure 4.26 Temperature gradient vs time for SF57 at different heater powers

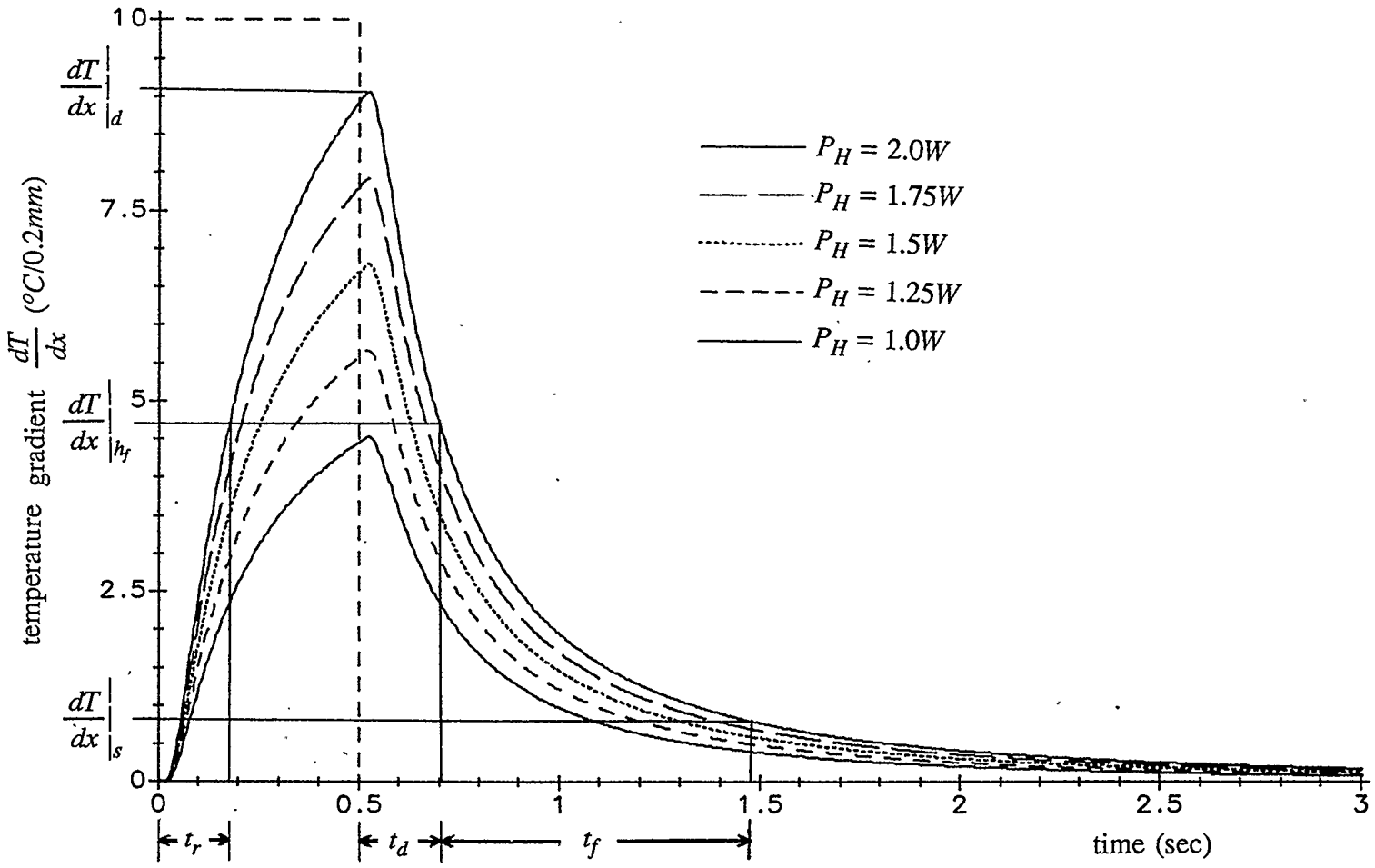

Figure 4.27 Temperature gradient vs time for SF11 at different heater powers

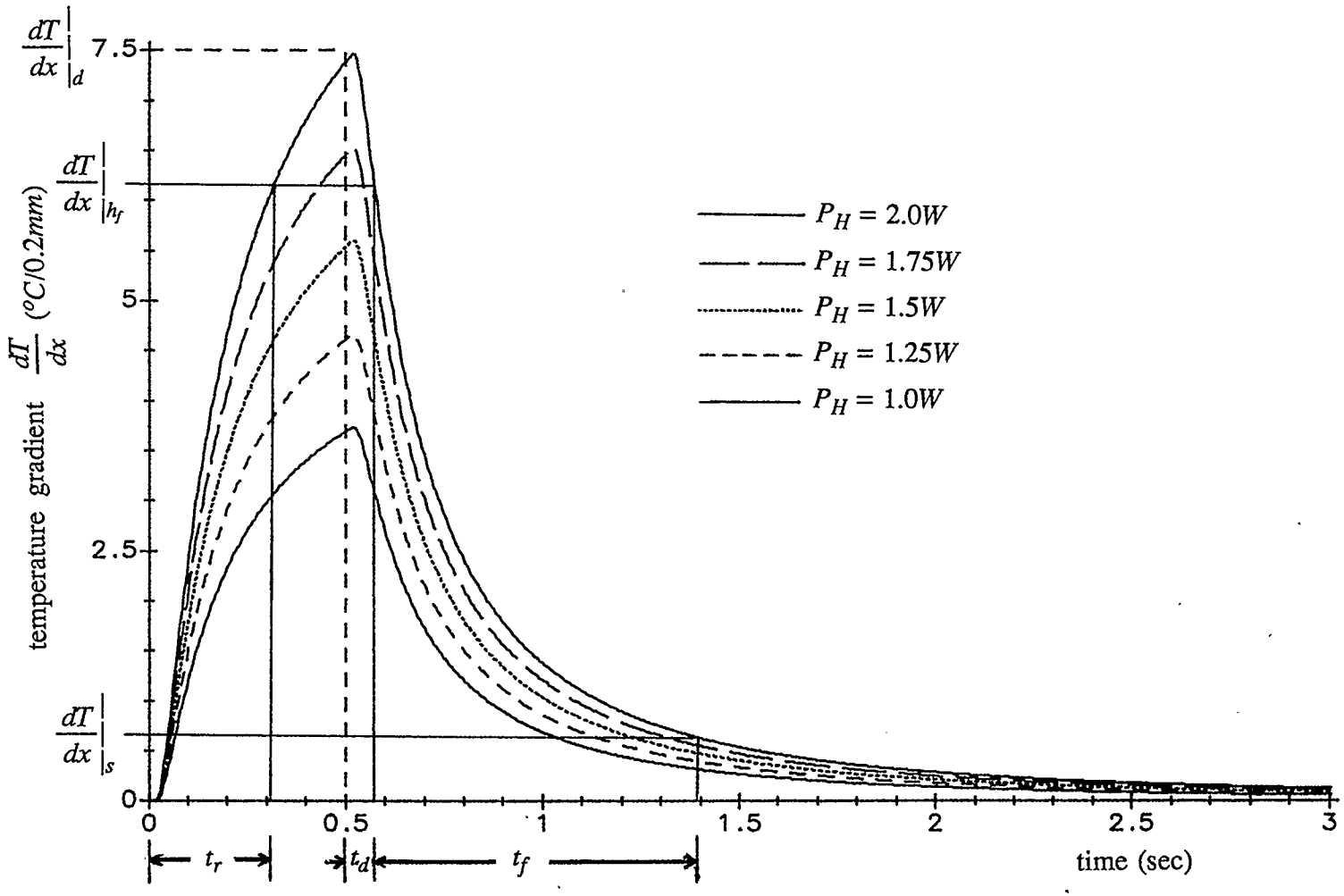

Figure 4.28 Temperature gradient vs time for SF13 at different heater powers

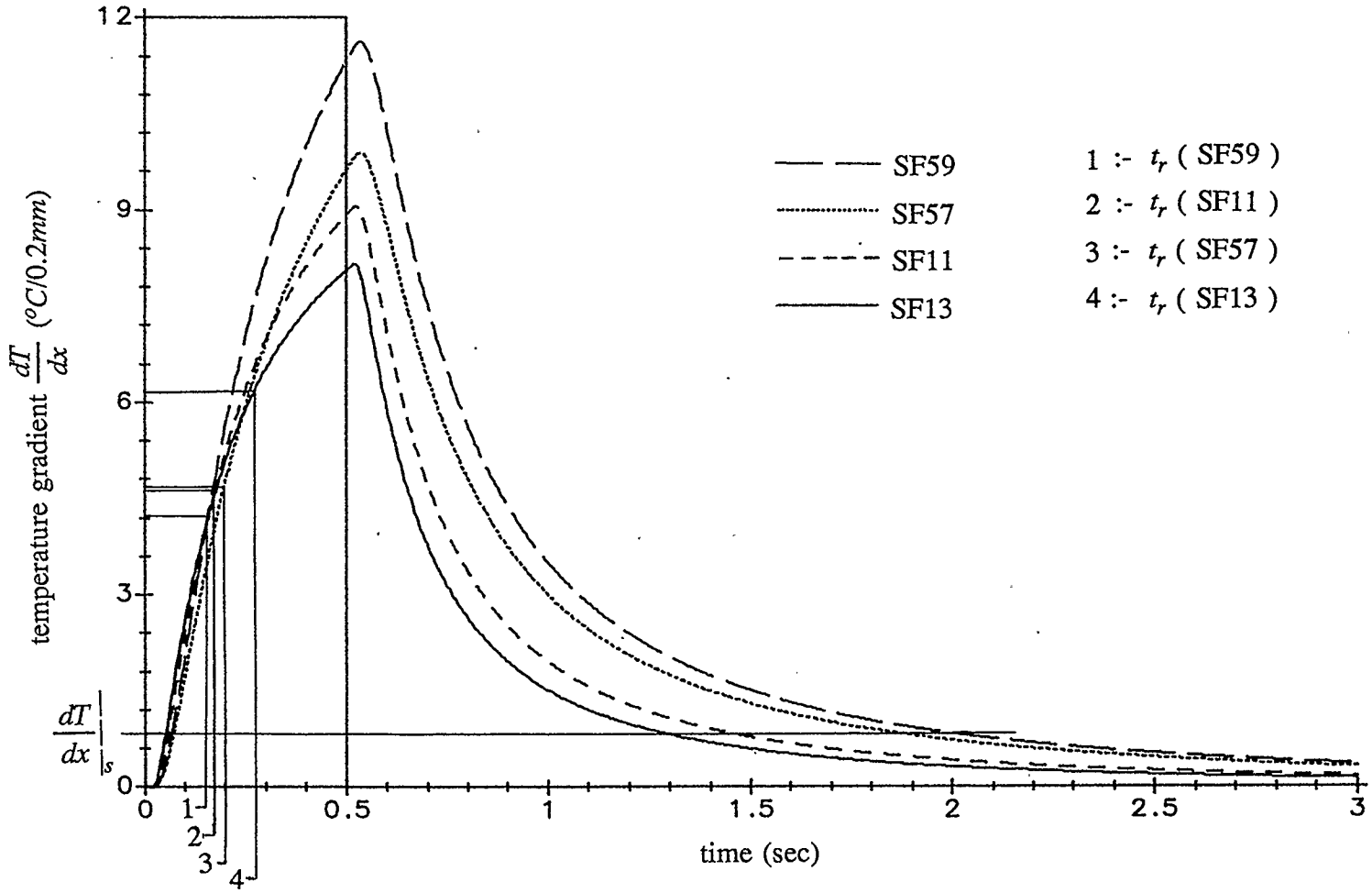

Figure 4.29 Temperature gradient vs time for different glasses at constant heater power density (67227 W/m^2)

SF11 requires a lower $\frac{dT}{dx}\Big|_{h_f}$ than for SF57, and as a result its rise time is lower than SF57. The glass property of SF11 (with its thermal diffusivity α being higher than for SF57 allows for a rapid energy-transfer rate and thus a shorter time to reach a particular temperature) allows for a decrease in its rise time. The delay time and fall time depends on the maximum dT/dx and correspondingly the maximum deflection d reached when the heater power is switched off. Thus SF13 has the minimum delay time and fall time as $d - h_f$ is the smallest and conversely SF59 has the maximum delay time and fall time.

The theoretical dc and pulse responses of the 2-D, 1×4 deflector can be similarly examined by considering dT/dx and dT/dy depending on the control voltages used.

4.4. Summary

This Chapter first begins with the limitations on the finite beam width due to the Fraunhofer diffraction effects. The theoretical dc and pulsed response of the switch are studied when a voltage is applied to the heater on the surface of the glass where the dc response characterises the physical property of the glass and the pulsed response gives the switch transient response. The importance of heater power density is observed in determining the temperature gradient and as a result the deflection angle. The effect of heater power on the transient response of the switch is also studied. The switch transient response as obtained theoretically for

different heater powers is dealt with in the next Chapter along with the experimental results of beam deflection angle and the transient response.

CHAPTER 5

EXPERIMENTAL RESULTS

5.1. Introduction

The experimental results for the 1-dimensional 1×2, and 2-dimensional 1×4 TO bulk deflectors are presented in this Chapter. The optical properties of the Schott glass samples are investigated with respect to the deflection of the input laser beam, extinction ratio in the output power and the transient response of the switch for different heater powers. The switch transient response as obtained theoretically and described in Section 3.4 is also presented later for different heater powers. Different switching patterns for the 2-dimensional TO bulk deflectors are also shown.

5.2. Results of dc Switch Operation

5.2.1. for 1-dimensional 1×2 deflector

The experimental dc operation characterises the optical properties of the glass samples. The variation of the deflection angle, θ_D, as a function of the applied heater power is shown in Figure 5.1, with the incident beam 0.3mm below the center of the heater. The glass type SF59 has the largest deflection angle of the four types of Schott glasses investigated since it has the largest temperature dependent index change dn/dT. Although SF57 has a smaller dn/dT than SF11 it

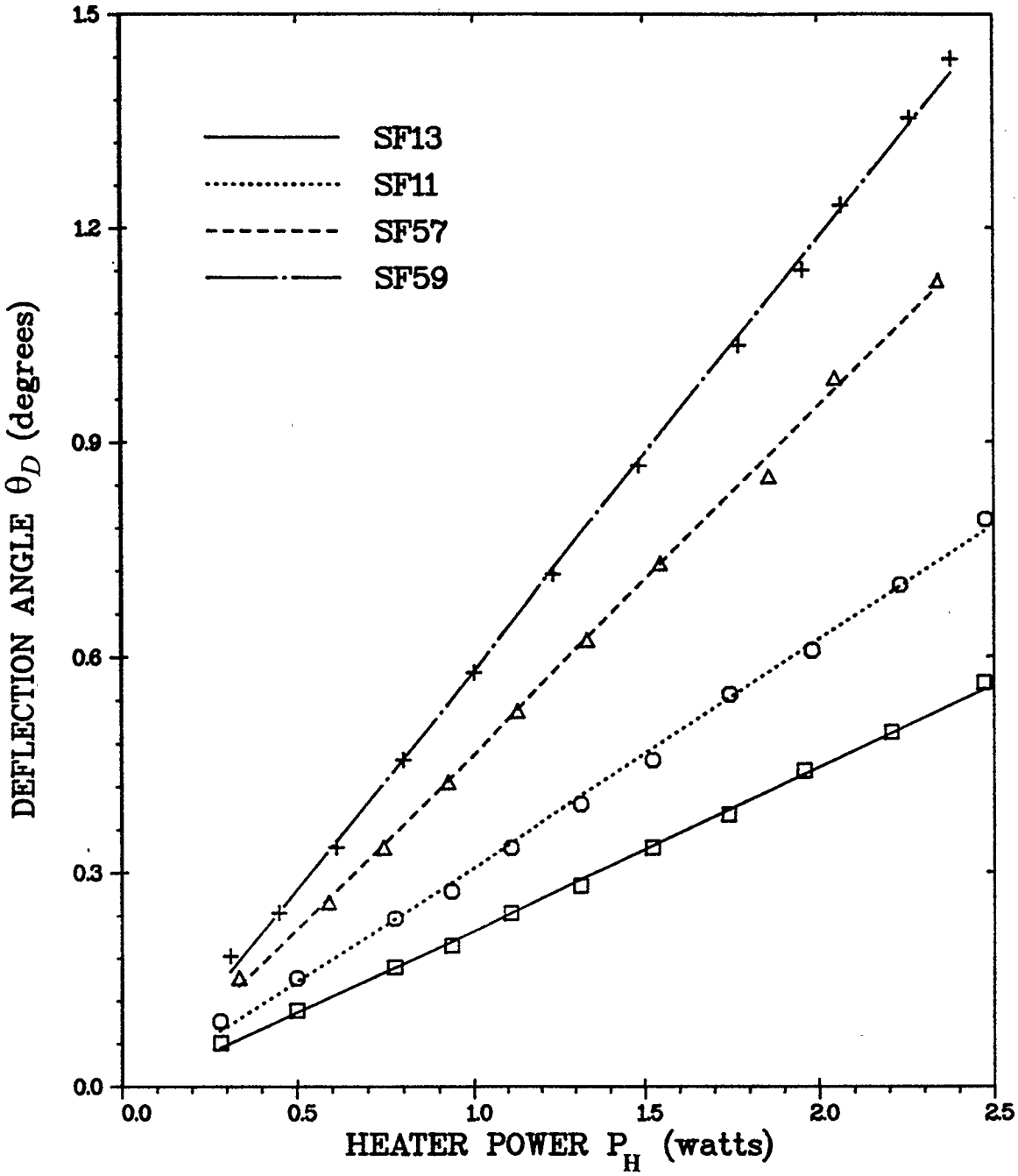

FIGURE 5.1 BEAM DEFLECTION ANGLE θ_D vs HEATER POWER P_H AT x=0.3mm

shows a greater deflection angle due to its thermal conductivity k being smaller than that for SF11. This gives a higher temperature difference between the top and bottom faces of the glass (a larger dT/dx) and as a result a higher index change with respect to the distance (a larger dn/dx) under the heater. The fact that SF57 shows a larger θ_D than SF11 is in agreement with the Figure 4.24.

Figure 5.2 shows the calculated and the experimental beam deflection angle as a function of heater power for the four types of glasses. For the heater power range considered, the maximum deflection angle obtained experimentally is 1.44^o for SF59 which compares within 12% error with the theoretical deflection angle of 1.63^o. The experimental data for SF57 and SF13 are also within reasonable theoretical values but glass type SF11 shows a large error from theoretical results. This may be due to the reason that either the optically polished glass surfaces are not parallel to each other and as a result not normal to the incident beam or the incident beam is itself not parallel to the horizontal axis. It is observed from Figure 5.1 that the figure of merit, $d\theta_D/dP_H$, is linear for all glasses up to the maximum P_H considered and that it varies from 0.228^o/watt for SF13 to 0.609^o/watt for SF59. The theoretical and the experimental values of the figure of merit are given in Table 5.1.

Figure 5.3 shows both theoretical and experimental θ_D as a function of the beam position, x, under the heater and it is seen that all four glass types suffer a reduction in θ_D as x increases. This is due to the temperature gradient decreasing as x increases as shown theoretically in Figure 4.21. The slope $d\theta_D/dx$ is

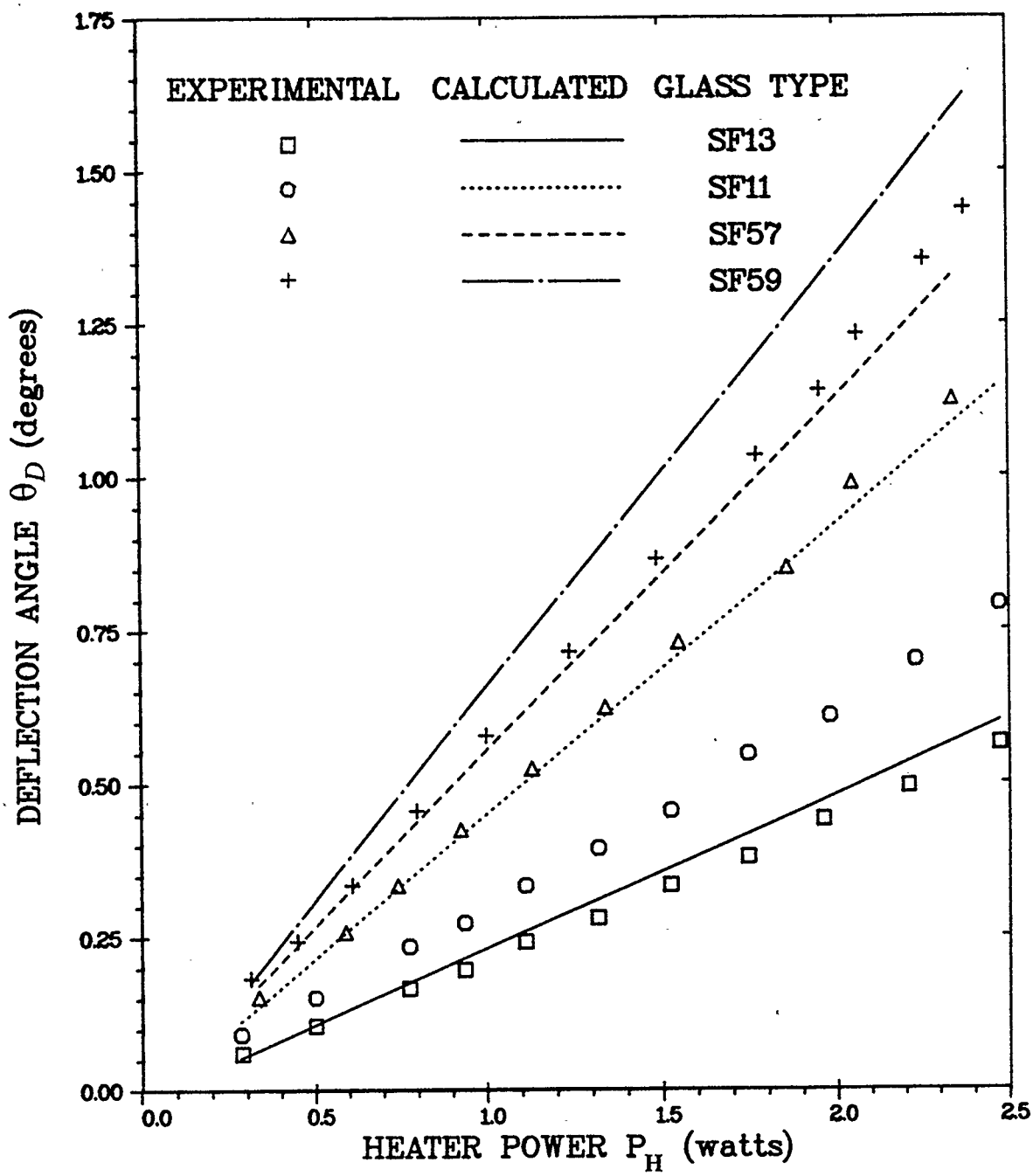

FIGURE 5.2 CALCULATED AND EXPERIMENTAL BEAM DEFLECTION ANGLE θ_D vs HEATER POWER P_H

Glass type	Figure of merit (^{o}/watt)		
	Theoretical	Experimental	% error
SF59	0.691	0.609	11.9
SF57	0.577	0.483	16.3
SF11	0.460	0.317	31.1
SF13	0.254	0.228	10.2

Table 5.1 Figure of merit as obtained theoretically and experimentally

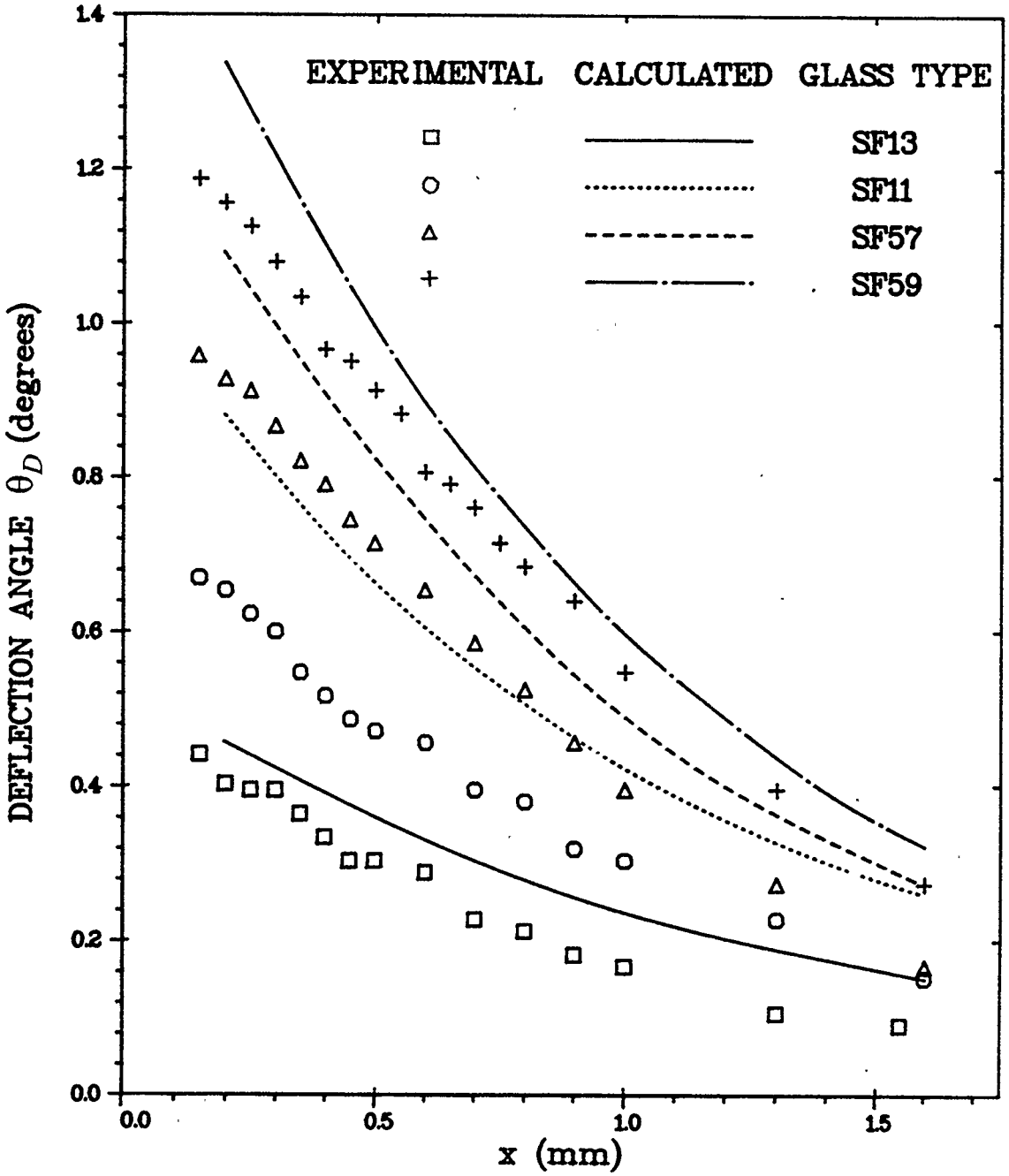

FIGURE 5.3 CALCULATED AND EXPERIMENTAL BEAM DEFLECTION ANGLE θ_D vs BEAM POSITION x

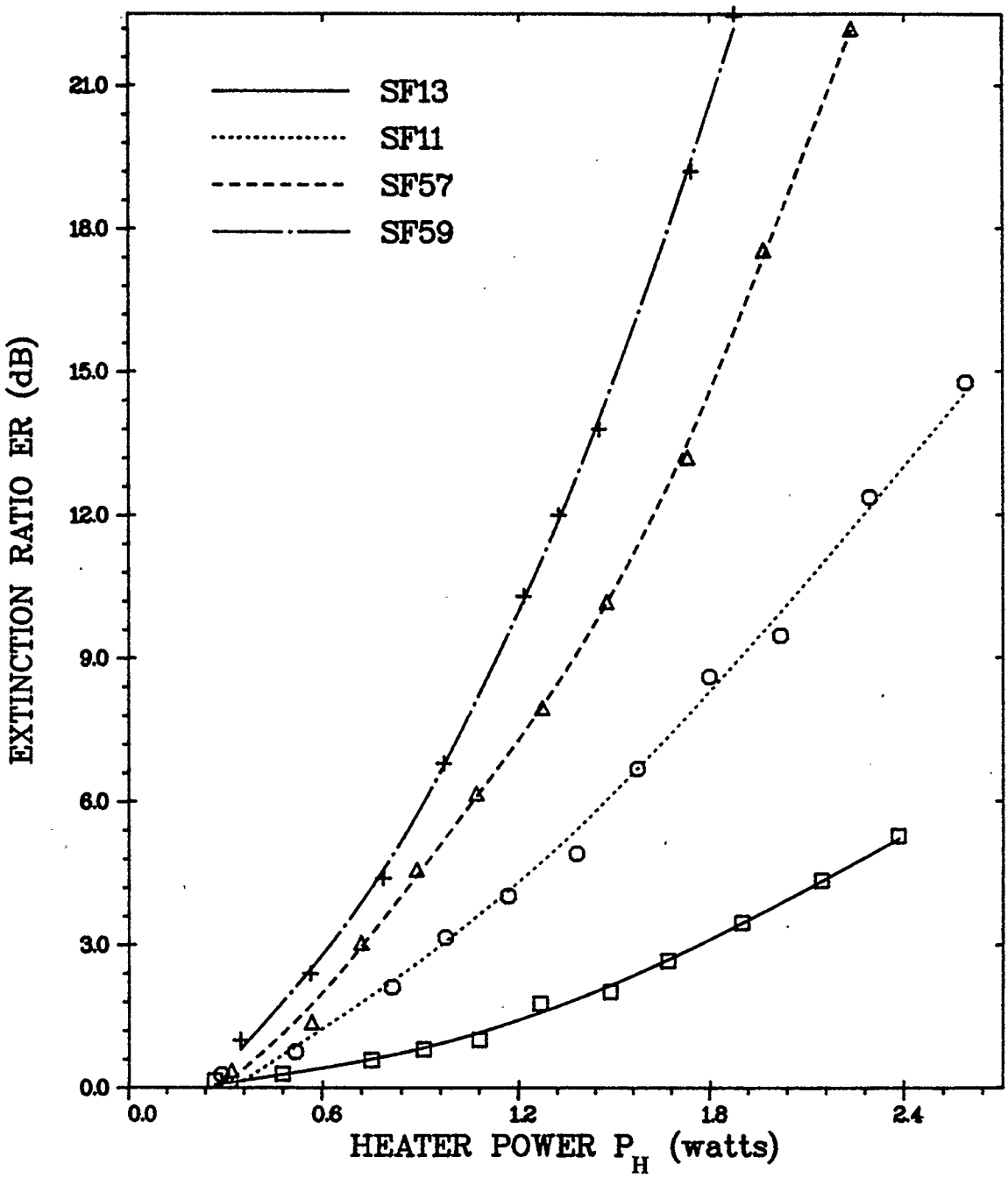

FIGURE 5.4 EXTINCTION RATIO vs HEATER POWER P_H

AT x=0.3mm

approximately same for SF59 and SF57 and this compares with the theoretical results shape of temperature gradient vs x in Figure 4.21. The glass type SF13 suffers the least amount of reduction in θ_D as x increases. The variation of the extinction ratio ER with heater power is given in Figure 5.4 and it is clear that the extinction ratio improves with increasing power (since $\theta_D \propto P_H$). It is confirmed that the TO circuit switch is extremely stable and that the deflection or switching action remains constant after many hours of dc heater operation.

5.2.2. for 2-dimensional 1×4 deflector

The input power requirement for a 1×3 switch can be effectively halved by fabricating the switch with identical heaters on opposite faces. A more novel technique however is to place the two heaters on adjacent faces as shown in Figure 3.3 and utilising the optical isotropy of glass to produce a two-dimensional circuit switch of enhanced capabilities.

The 2-D 1×4 circuit switch of Figure 3.3 has been successfully tested at low power and the output beam made to trace out the pattern shown in Figure 5.5. The output beams 1, 2 and 3 correspond to control voltages V_1, V_2 and V_1 together with V_2 respectively in Figure 3.3. It is observed from Figure 5.5 that an output beam in any given position can be switched directly to any of the three remaining positions. The extinction ratios are approximately equal when identical heater power densities are applied separately to the two heaters and it improves with their simultaneous application. Different forms of switching patterns can be obtained

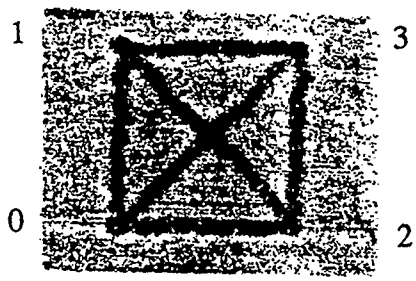

Figure 5.5 2-D Switching pattern of 1×4 TO switch

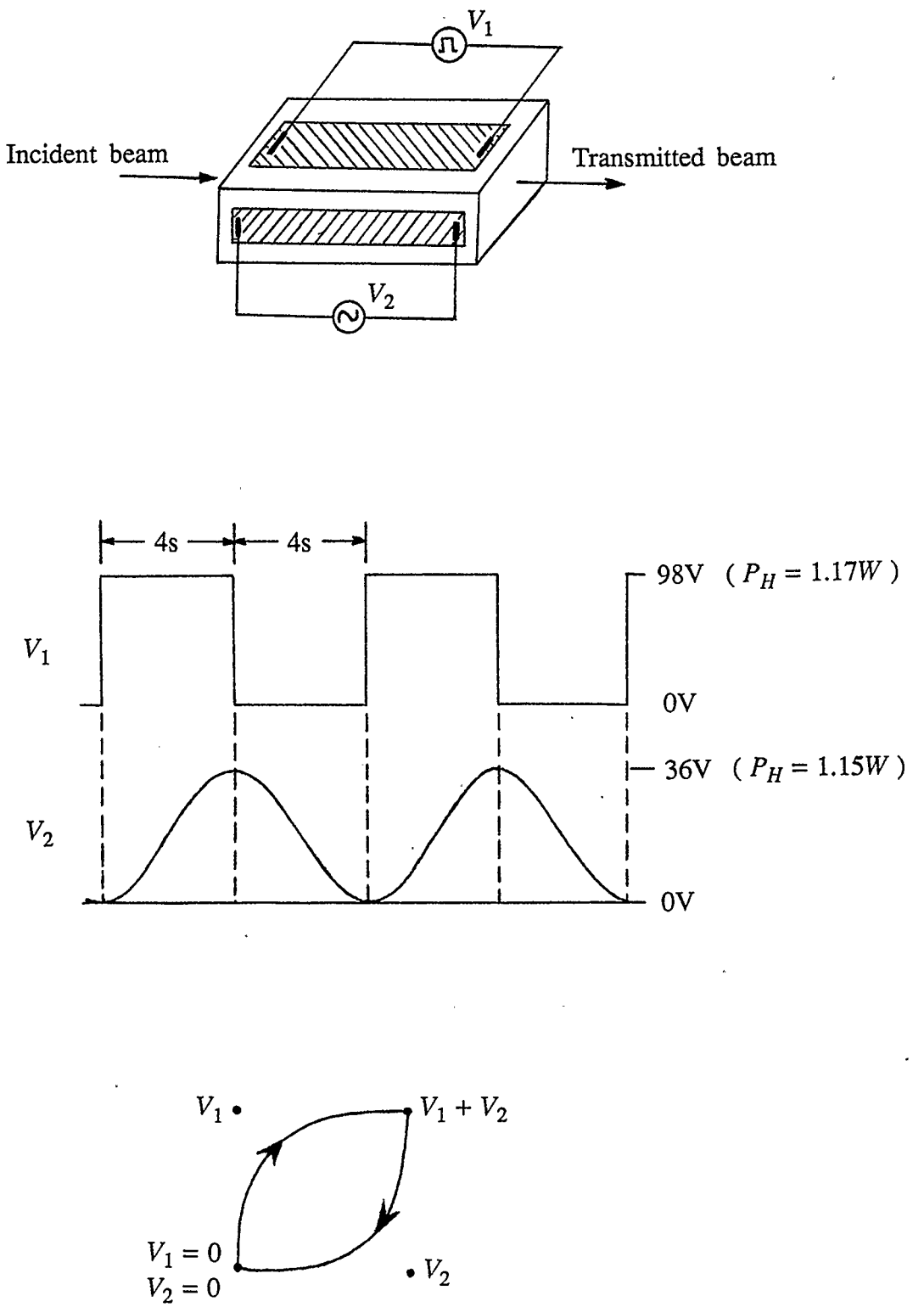

Figure 5.6 Switching pattern of 1×4 TO switch for pulsed and sinusoidal heater voltages

with appropriate voltage waveforms and frequencies applied to the two heater elements. One such pattern is shown in Figure 5.6 along with the voltage waveform and frequency applied.

5.3. Results of Pulsed Switch Operation

Figures 5.7 to 5.9 compare the shape of the experimentally obtained switch transient response at fibre position 1 for SF11, SF57 and SF13 respectively with that obtained theoretically for different heater powers with a heater power pulse width of 0.5sec and a pulse period of 3.0sec. According to the theoretical approach the response of dT/dx with time as shown in Figures 4.26 to 4.28 corresponds to the optical transient responses. To draw the theoretical transient response w_f, depicted in Figure 3.6, is plotted with respect to the time required to obtain the corresponding $\left.\frac{dT}{dx}\right|_{w_f+s}$ where w_f varies from 0.0mm to 0.125mm. At $w_f = 0.0$mm, that is, when $\left.\frac{dT}{dx}\right|_{s}$ is reached, the fibre at position 1 detects a decrease in its power level. When $w_f = 0.125$mm, the time corresponds to $\left.\frac{dT}{dx}\right|_{h_f}$ in Figures 4.26 to 4.28 and is equal to the rise time. When the input heater power pulse is zero the time corresponding to $\left.\frac{dT}{dx}\right|_{h_f}$ and $\left.\frac{dT}{dx}\right|_{s}$ from the cooling curve gives the delay time and the fall time respectively. It is observed experimentally and theoretically from Figures 5.7 to 5.9 that the rise time decreases whereas the

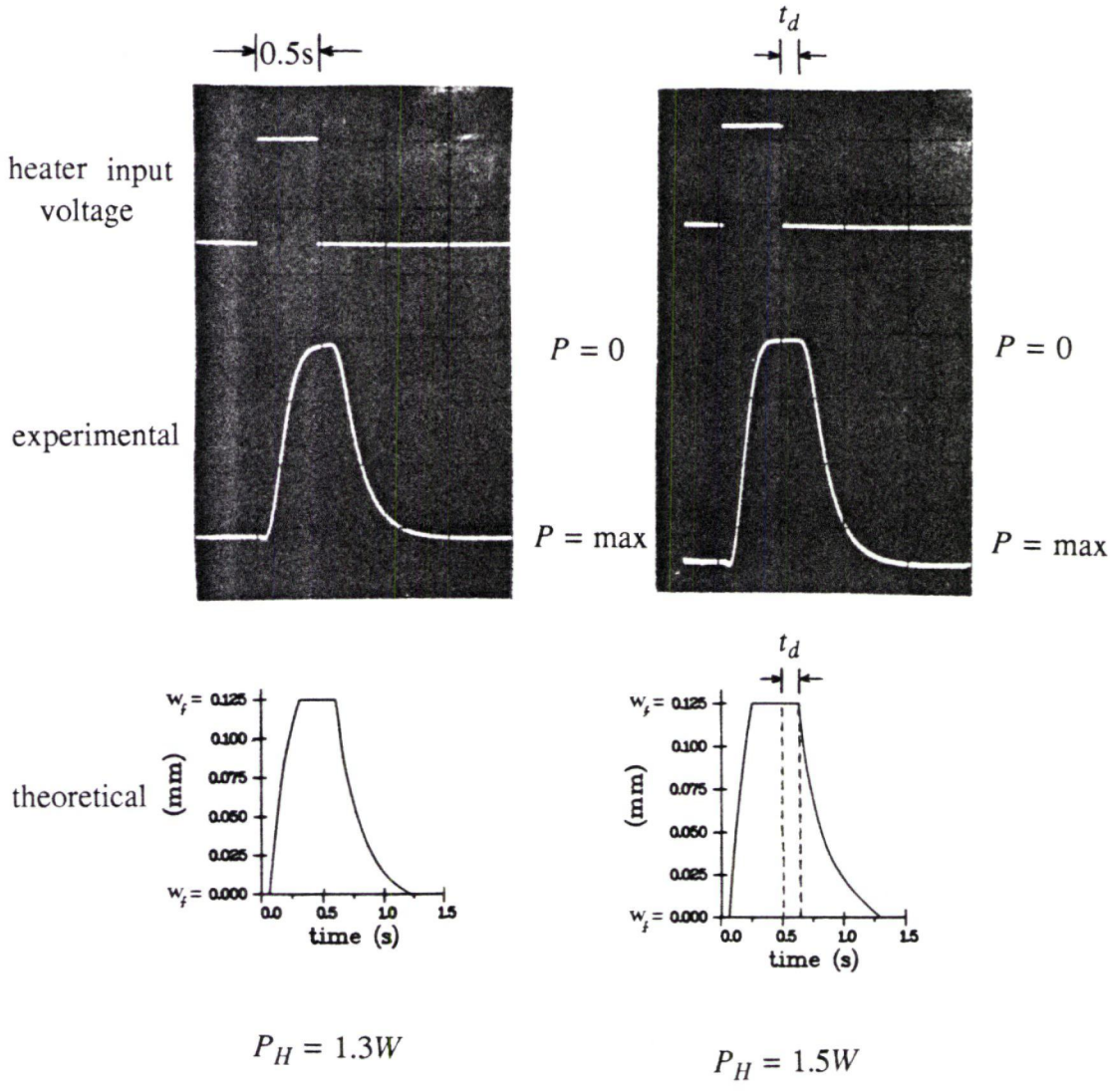

Figure 5.7 Switch transient response for SF11 as obtained experimentally and theoretically for different heater power

(P = Power detected in the fibre at position 1)

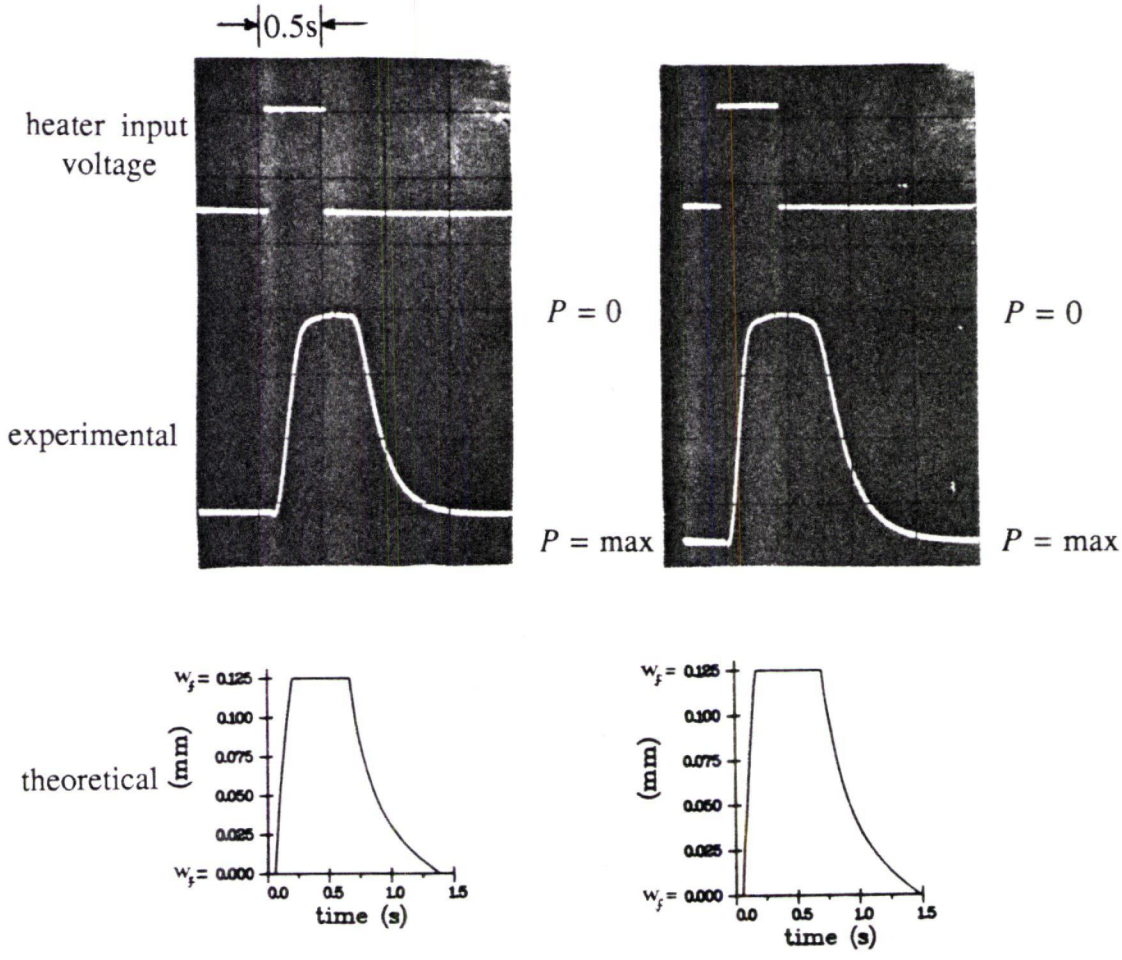

$P_H = 1.75W$ $P_H = 2.0W$

Figure 5.7 (continued)

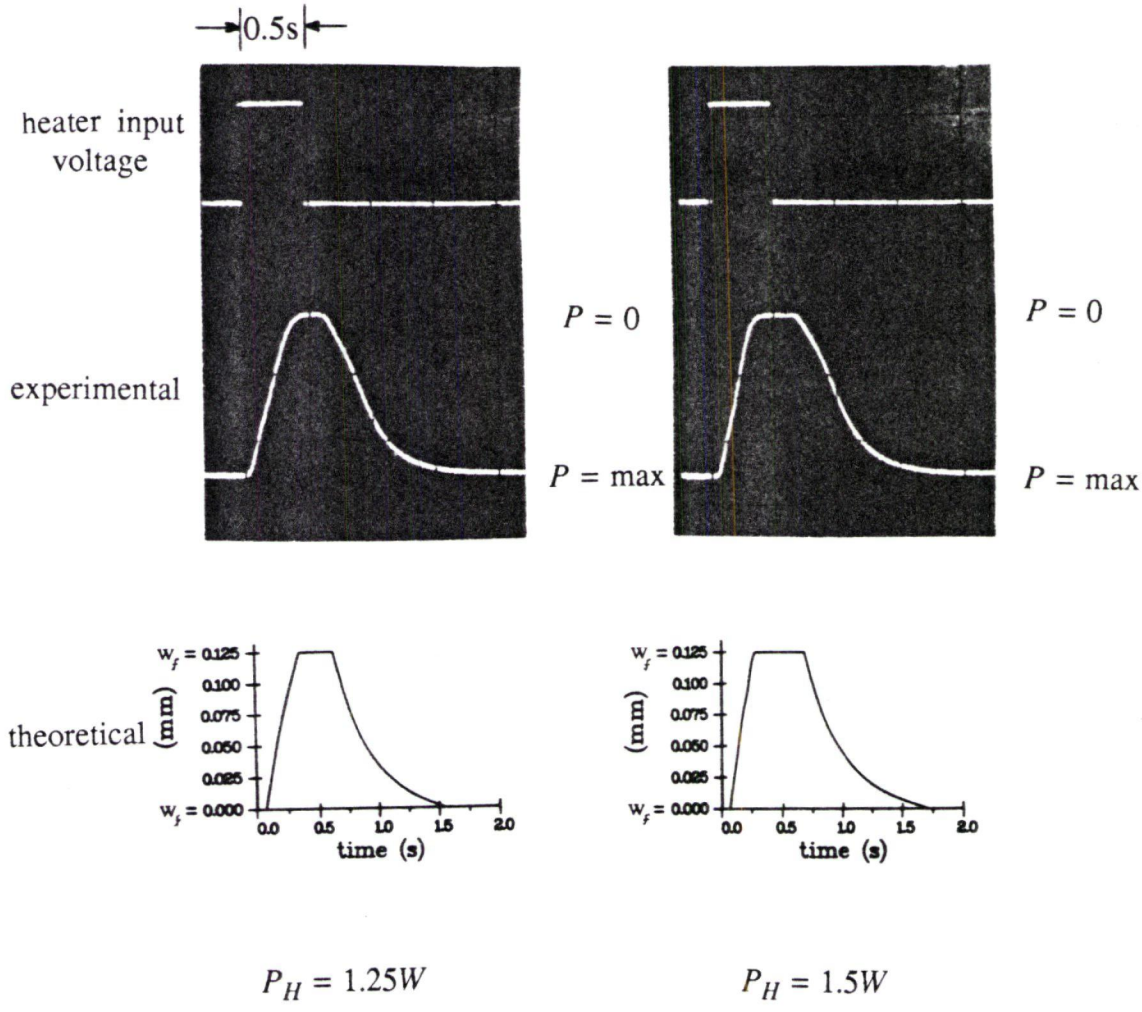

Figure 5.8 Switch transient response for SF57 as obtained experimentally and theoretically for different heater power

(P = Power detected in the fibre at position 1)

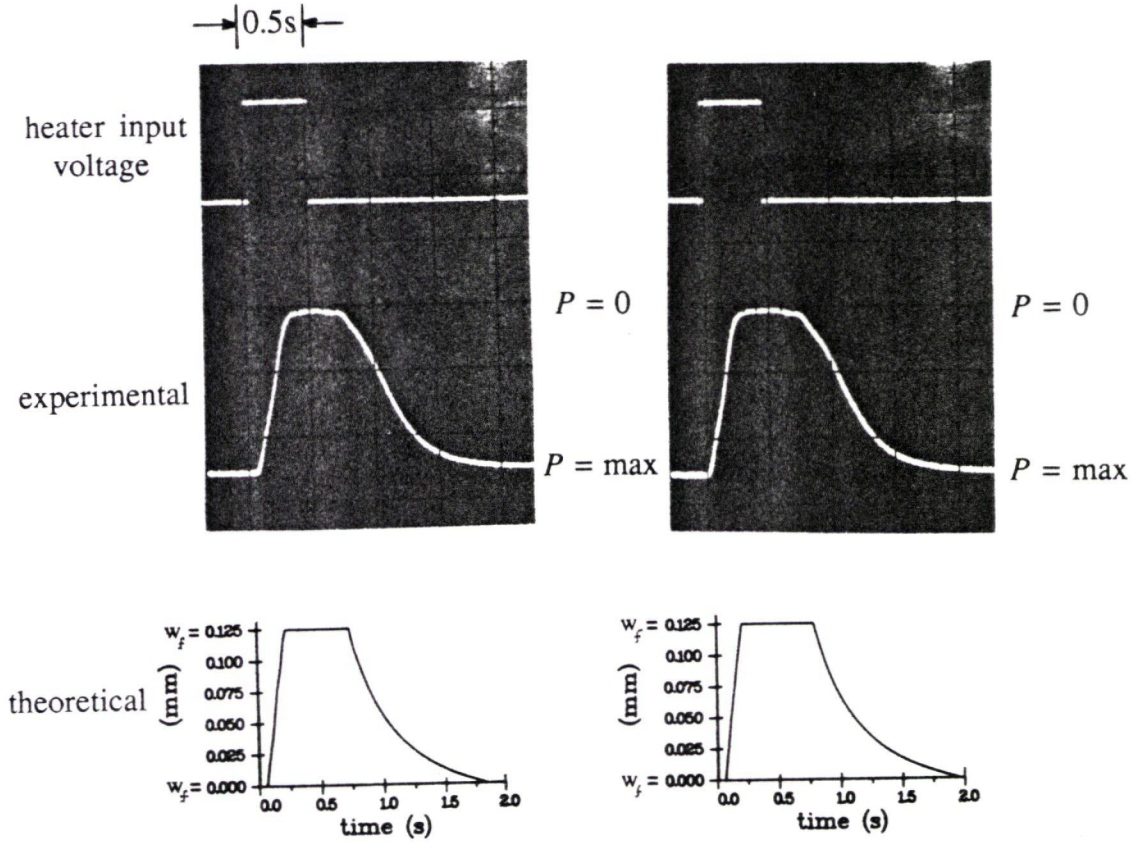

$P_H = 1.75W$ $P_H = 2.0W$

Figure 5.8 (continued)

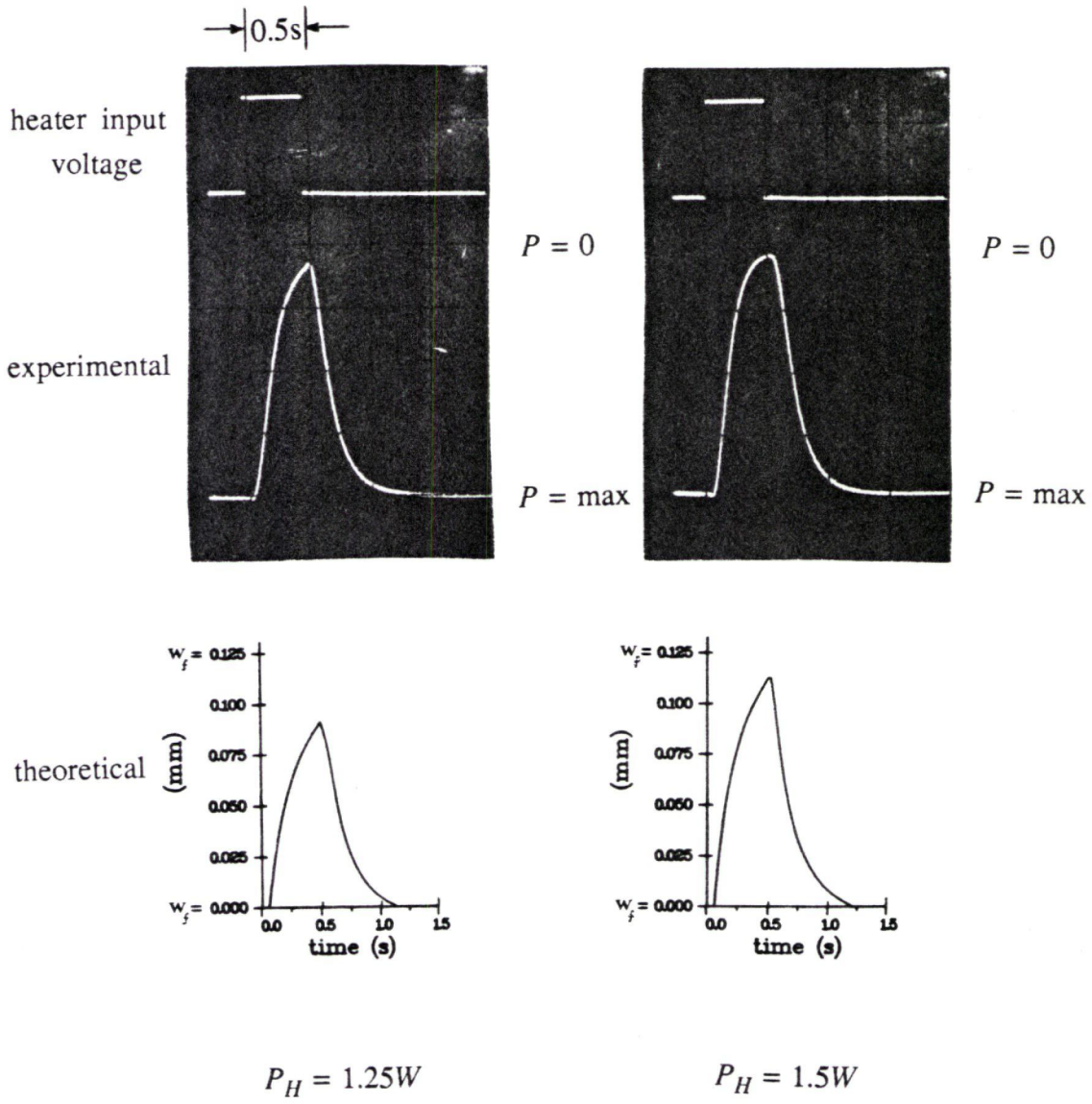

$P_H = 1.25W$ $P_H = 1.5W$

Figure 5.9 Switch transient response for SF13 as obtained experimentally and theoretically for different heater power

(P = Power detected in the fibre at position 1)

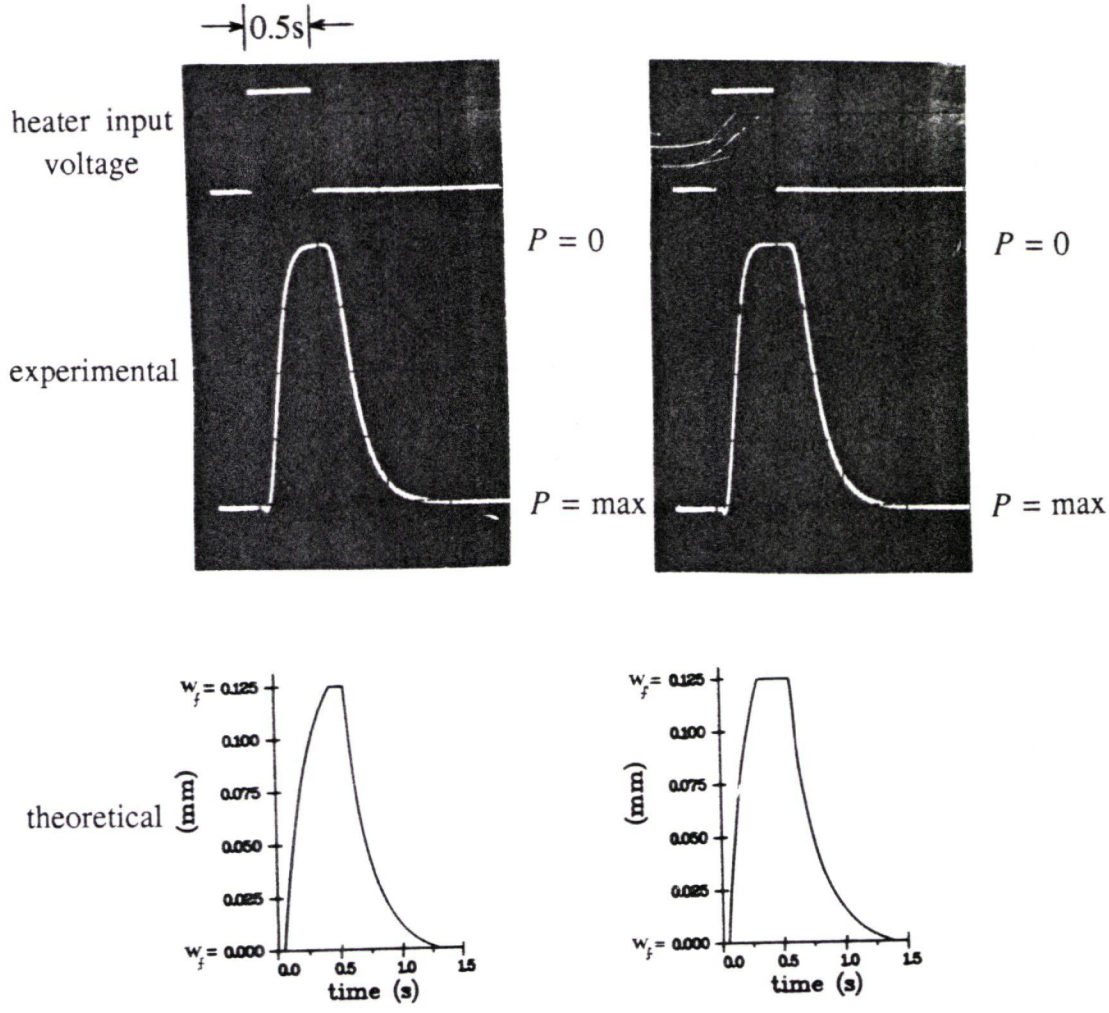

$P_H = 1.75W$ $P_H = 2.0W$

Figure 5.9 (continued)

delay time and fall time increase as the heater power is increased. In the case of SF13, when a heater power of 1.25W is applied the maximum dT/dx obtained is not sufficient for the beam to travel the complete fibre distance. So the power detected at fibre position 1 is not zero in the switch on position, however, for a higher power input, a zero power level is detected at the fibre at position 1. Tables 5.2 to 5.4 depict the values of the experimental and theoretical response times for SF11, Sf57 and SF13 respectively. It is evident that the glass type SF11 has the minimum rise time and fall time of the three glass types for similar heater powers applied whereas SF57 shows their maximum values.

5.4. Summary

This Chapter gives the results for both the 1-D 1×2, and 2-D 1×4 TO bulk deflectors where the 2-dimensional switching action of the glass can be used to obtain output beam patterns of different shapes. The values for the deflection angle as obtained experimentally for the different Schott glass samples are compared with the calculated ones and they are found to be reasonably close except for the glass type SF11. The discrepancies in the results may be primarily due to the accuracy of the experimental set-up and device preparation. The transient response of the physical property dT/dx of glass is observed to correspond very closely with the transient response of the optical switch. The rise time and fall time decrease and increase respectively when the applied heater power is increased, fall time being dependent on the maximum deflection. The glass type

P_H (W)	t_r (sec)	t_d (sec)	t_f (sec)
2.0	0.175	0.205	0.7725
1.75	0.2	0.17	0.72
1.5	0.25	0.1325	0.6675
1.3	0.312	0.1	0.624

(a)

P_H (W)	t_r (sec)	t_d (sec)	t_f (sec)
2.0	0.2	0.23	0.88
1.75	0.22	0.18	0.8
1.5	0.28	0.15	0.75
1.3	0.35	0.1	0.7

(b)

Table 5.2 Switch transient response time for SF11 as obtained (a) theoretically and (b) experimentally

P_H (W)	t_r (sec)	t_d (sec)	t_f (sec)
2.0	0.205	0.287	1.18
1.75	0.23	0.242	1.11
1.5	0.2787	0.1885	1.033
1.25	0.3525	0.1311	0.926

(a)

P_H (W)	t_r (sec)	t_d (sec)	t_f (sec)
2.0	0.225	0.275	1.3
1.75	0.25	0.25	1.25
1.5	0.3	0.185	1.115
1.25	0.38	0.14	1.0

(b)

Table 5.3 Switch transient response time for SF57 as obtained (a) theoretically and (b) experimentally

P_H (W)	t_r (sec)	t_d (sec)	t_f (sec)
2.0	0.3143	0.0714	0.8163
1.75	0.4367	0.047	0.7592
1.5	--	--	0.7245
1.25	--	--	0.6387

(a)

P_H (W)	t_r (sec)	t_d (sec)	t_f (sec)
2.0	0.35	0.08	0.87
1.75	0.45	0.055	0.845
1.5	--	--	0.82
1.25	--	--	0.8

(b)

Table 5.4 Switch transient response time for SF13 as obtained (a) theoretically and (b) experimentally

SF11 shows the best transient response although its beam deflection angle or extinction ratio is not the maximum of the Schott glasses considered.

CHAPTER 6

CONCLUSIONS

6.1. Conclusions

The current rapid development of glass fibre optical communications systems has created the need for investigating the methods of production of optical switches and deflectors. Efficient inexpensive devices have to be sought since the costs of these devices effect the total system cost. The thermo-optic (TO) bulk deflector demonstrated in this thesis fulfills the needs of a low cost circuit switch in glass using the thermo-optic effect originating from the temperature dependence of the refractive index, where, the thermally induced index changes required for light deflection and switching are provided by applying an appropriate voltage to a small film heater deposited on the glass surface.

Four commercial glass samples from Schott Glass Company are investigated theoretically and experimentally for their performance evaluation with respect to deflection angle and transient response of the switch for different heater powers. The theoretical dc operation comprising the temperature analysis of the device characterises the physical properties of the glass samples whereas the experimental dc operation is the characterisation of the optical properties.

In this thesis both a 1-dimensional 1×2, and a 2-dimensional 1×4 TO bulk deflector have been demonstrated. With the dimensions of $24 \times 5 \times 2.3$mm, a

stable deflection of approximately 1.4^o, a $d\theta_D/dP_H$ of $\sim 0.6^o$/watt, an extinction ratio exceeding 20 dB and a rise time of approximately 200 ms, the low cost TO deflector is a viable building block for a full-access non-blocking $(n \times n)$ circuit switch. The TO bulk deflector is designated a circuit switch because its dynamic response is not suitable for Time Division Multiplexing (TDM) or digital switching types of operation, it is however adequate for circuit switching where the switching time is very much shorter than the holding time.

Due to inhouse limitations when cutting and polishing the glass samples it was necessary to maintain the thickness and the width of the switches at 2.3mm and 5mm respectively. As the switches are designated to accommodate 125μm fibres it is obvious that after sufficient fibre separation is allowed in order to achieve a high ER, then a thickness of 2.3mm and a width of 5mm is too great, it increases the bulk of the glass needlessly, and it simply penalises the dynamic performance of the switch.

The deflection angle of all the four Schott glasses considered increases linearly with the heater power. The transient response of the physical property dT/dx of glass is observed to correspond with the optical transient response of the switch. The rise time and fall time decrease and increase respectively when the applied heater power is increased. The values for the deflection angle and the response time for the switches as obtained experimentally compare very closely with the calculated ones. The deflection angle and the switch transient response depend not only on the type of glass but also on the heater power density and the

position of the incident beam from the heater surface. The main conclusions from the analysis of the four Schott glasses are summarised as follows:

(1) Under similar heater power applied to the glass surfaces the glass type SF59 shows the maximum deflection angle since it has the largest temperature dependent index change dn/dT and the lowest value of the thermal conductivity k giving rise to the maximum temperature gradient in the direction of the heat flow.

(2) For identical placement of the fibre at the output end of the switch, i.e. for similar $\left.\frac{dT}{dx}\right|_s$ as shown in Figure 4.29, and for similar heater power densities applied to the heater surfaces with equal heater widths and areas, the glass types SF59 and SF13 show the minimum and maximum rise time respectively. SF59, however, has the maximum delay time and fall time. The glass type SF11 is seen to have a rise time only slightly greater than SF59 but its fall time is very much smaller. SF11 is also seen to have a better rise time and fall time than SF57. It is noted that SF13 has a significantly larger relative rise time than SF11 although its fall time is somewhat smaller.

The choice of the glass type depends on the application of the switch. The glass type SF59 should be chosen where large deflection angle and extinction ratio are required such as in 1×3 switch with a single heater. For a constant angle of deflection SF59 will require a lower heater power than all the other glasses but SF11 may still have a better rise time and fall time. The slow switching or

deflection action of the bulk deflector may find application where slow scanning in the form of light is a requirement. This device also has the potential of being used at moderately high optical power levels.

A unique property of the glass TO bulk deflector is its ability to realise a true isotropic 2-dimensional switching action - a form of "optical CRO". Different output switching patterns can be obtained with the appropriate control waveforms applied to the two heater elements of the deflector.

6.2. Suggestions for Future Developments

The following are suggested topics for further research:

(1) Switches optimised in terms of their physical configuration may be fabricated thus improving their dynamic performances. Theoretically, better results are expected.

(2) Other low cost, inexpensively fabricated TO switching materials may be sought.

(3) A 3×3 full-access non-blocking circuit switch as shown in Figure 6.1 may be constructed to verify its effectiveness in applications such as local area networks (LANs). The effectiveness of optical switching in Community Antenna TV (CATV) networks is also a leading candidate for investigation.

(4) By reducing the input beam diameter to that of the fibre diameter, smaller deflectors and 1×6, 1×9 lower power 2-D devices may be fabricated.

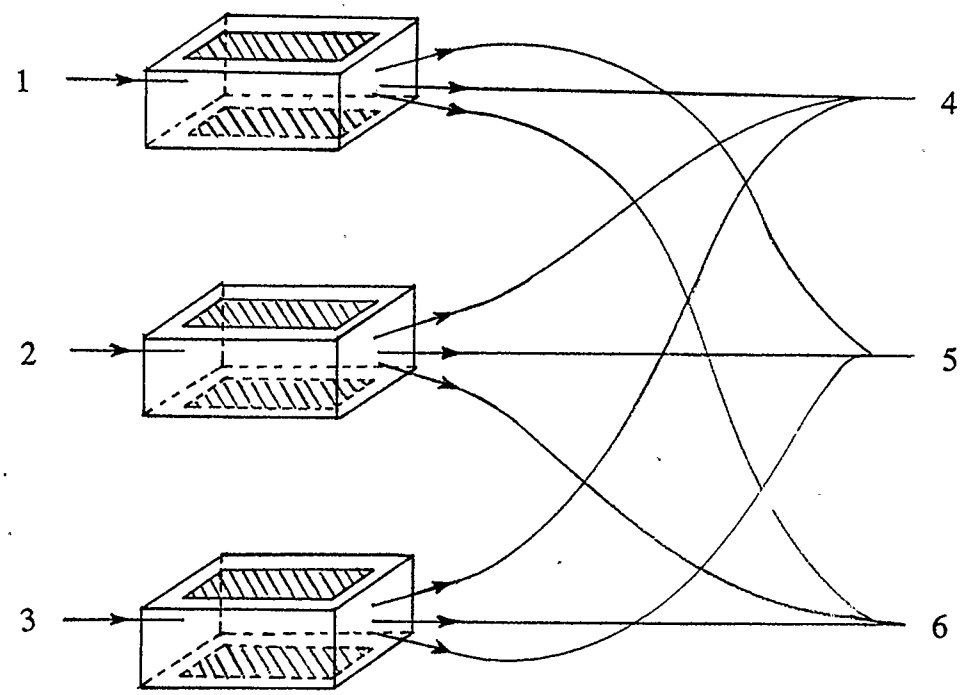

Figure 6.1 Structure of the 3×3 non-blocking TO circuit switch

REFERENCES

(1) H.F. Wolf, *Handbook of Fiber Optics: Theory and Applications,* New York: Garland STPM Press, 1979.

(2) R.A. Soref, D.H. McMahon, and A.R. Nelson, "Multimode achromatic electro-optic waveguide switch for fiber-optic communications," *Applied Physics Letters,* Vol.28, No.12, pp.716-718, June 1976.

(3) J.P. Sheridan, J.M. Schnur, and T.G. Giallorenzi, "Electro-optic switching in low-loss liquid-crystal waveguides," *Applied Physics Letters,* Vol.22, No.11, pp.560-561, June 1973.

(4) M. Haruna and J. Koyama, "Electrooptical Branching Waveguide Switches and their Application to 1 × 4 Optical Switching Networks," *IEEE Journal of Lightwave Technology,* Vol.LT-1, No.1, pp.223-227, March 1983.

(5) T. Aoyama, T. Hibiya, and Y. Ohta, "A New Faraday Rotator Using a Thick Gd:YIG Film Grown by Liquid-Phase Epitaxy and its Applications to an Optical Isolator and Optical Switch," *IEEE Journal of Lightwave Technology,* Vol.LT-1, No.1, pp.280-284, March 1983.

(6) M. Shirasaki, H. Takamatsu, and T. Obokata, "Bistable magnetooptic switch for multimode optical fiber," *Applied Optics,* Vol.21, No.11, pp. 1943-1949, June 1982.

(7) M. Shirasaki, H. Nakajima, T. Obokata, and K. Asama, "Nonmechanical optical switch for single-mode fibers," *Applied Optics,* Vol.21, No.23, pp. 4229-4234, December 1982.

(8) Eddie H. Young, Jr., and Shi-Kay Yao, "Design Considerations for Acousto-Optic Devices," *Proceedings of the IEEE,* Vol.69, No.1, pp.54-64, January 1981.

(9) M. Haruna, and J. Koyama, "Thermo-optic effect in $LiNbO_3$ for Light Deflection and Switching," *Electronics Letters,* Vol.17, No.22, pp.842-844, October 1981.

(10) M. Haruna, and J. Koyama, "Thermooptic deflection and switching in glass," *Applied Optics,* Vol.21, No.19, pp.3461-3465, October 1982.

(11) D. Irvine-Halliday, and A. Agarwal, "Optical Fibre Circuit Switching Using Low Cost Thermo-Optic Bulk Deflector," *Proc. 10th Australian Conference on Optical Fibre Technology,* Perth, pp.119-123, December 1985.

(12) T.S. Narasimhamurty, *Photoelastic & electrooptic properties of crystals,* New York: Plenum Press, 1981.

(13) P.V. Lenzo, E.G. Spencer, and K. Nassau, "Electro-Optic Coefficients in Single-Domain Ferroelectric Lithium Niobate," *Journal of the Optical Society of America,* Vol.56, No.5, pp.633-635, May 1966.

(14) Homer Fay, "Electro-Optic Modulation of Light Propagating near the Optic Axis in $LiNbO_3$," *Journal of the Optical Society of America,* Vol.59, No.11,

pp.1399-1404, November 1969.

(15) R.C. Miller, and A. Savage, "Temperature dependence of the Optical Properties of Ferroelectric $LiNbO_3$ and $LiTaO_3$," *Applied Physics Letters,* Vol.9, No.4, pp.169-171, August 1966.

(16) G.B. Hocker, "Fiber-optic scanning of pressure and temperature," *Applied Optics,* Vol.18, No.9, pp.1455-1448, May 1979.

(17) Optical Glass, *Schott Glass Technologies Inc.,* 1984.

(18) E.M. Slayter, *Optical Methods in Biology,* Wiley-Interscience, N.Y. 1970.

(19) Chi-Sum Lawrence Yu, "The Time-dependent diffusion of CO_2 in normal-hexadecane at Elevated Pressures," *M.Sc Thesis, Department of Chemical and Petroleum Engineering,* The University of Calgary, Alta., 1984.

(20) W.H.A. Fincham, and M.H. Freeman, *Optics,* 9th Edition, U.K.: The University Press, Cambridge, 1980.

(21) J.P. Holman, *Heat Transfer,* 3rd Edition, U.S.A.: McGraw-Hill Book Company, 1972.

(22) G. Siddall, and B.A. Probyn, "Vacuum-deposited metal film resistors," *British Journal of Applied Physics,* Vol.12, pp.668-674, December 1961.

(23) Leon I. Maissel, and Reinhard Glang, *Handbook of Thin Film Technology,* U.S.A.: McGraw-Hill Book Company, 1970.

APPENDIX

DERIVATION OF THE FINITE DIFFERENCE EQUATIONS FOR DIFFERENT GEOMETRIC SHAPES

Using the Fourier's law of heat conduction and assuming unit depth of material the transient energy balance on the node (m,n) is made by setting the sum of the energy conducted and convected into the node equal to the increase in the internal energy of the node for the geometric shapes shown in Figures 2.7b to 2.7j.

For the vertical convection boundary node shown in Figure 2.7b, the transient energy balance on the node (m,n) is

$$-k\Delta x\frac{T^p_{m,n} - T^p_{m-1,n}}{\Delta y} - k\frac{\Delta y}{2}\frac{T^p_{m,n} - T^p_{m,n+1}}{\Delta x} - k\frac{\Delta y}{2}\frac{T^p_{m,n} - T^p_{m,n-1}}{\Delta x}$$

$$= \rho c\frac{\Delta y}{2}\Delta x\frac{T^{p+1}_{m,n} - T^p_{m,n}}{\Delta t} + h_V\Delta x(T^p_{m,n} - T_\infty)$$

If $\Delta x = \Delta y$, the relation for $T^{p+1}_{m,n}$ becomes the same as Equation (2.22).

For the node (m,n) shown in Figure 2.7c, the energy balance equation is the same as the above equation except that the term $T^p_{m+1,n}$ exists instead of $T^p_{m-1,n}$.

For the horizontal convection boundary node as shown in Figure 2.7d, the transient energy balance on the node (m,n) is

$$-k\Delta y\frac{T^p_{m,n}-T^p_{m,n+1}}{\Delta x}-k\frac{\Delta x}{2}\frac{T^p_{m,n}-T^p_{m-1,n}}{\Delta y}-k\frac{\Delta x}{2}\frac{T^p_{m,n}-T^p_{m+1,n}}{\Delta y}$$

$$=\rho c\frac{\Delta x}{2}\Delta y\frac{T^{p+1}_{m,n}-T^p_{m,n}}{\Delta t}+h_H\Delta y(T^p_{m,n}-T_\infty)$$

When $\Delta x = \Delta y$, rearranging for $T^{p+1}_{m,n}$ gives the Equation (2.24).

For the physical situation in Figure 2.7e, the energy balance equation is the same as the above equation except that now the term $T^p_{m,n-1}$ exists instead of $T^p_{m,n+1}$ and h_{Al} is used in place of h_H.

The energy balance equation for the corner with convection boundary as shown in Figure 2.7f is

$$-k\frac{\Delta x}{2}\frac{T^p_{m,n}-T^p_{m-1,n}}{\Delta y}-k\frac{\Delta y}{2}\frac{T^p_{m,n}-T^p_{m,n+1}}{\Delta x}=h_V\frac{\Delta x}{2}(T^p_{m,n}-T_\infty)$$

$$+h_H\frac{\Delta y}{2}(T^p_{m,n}-T_\infty)+\rho c\frac{\Delta x}{2}\frac{\Delta y}{2}\frac{T^{p+1}_{m,n}-T^p_{m,n}}{\Delta t}$$

If $\Delta x = \Delta y$ Equation (2.26) is obtained for $T^{p+1}_{m,n}$.

The energy balance equation for the node (m,n) shown in Figure 2.7g is the same as the above equation except that the terms $T^p_{m+1,n}$ and $T^p_{m+1,n+1}$ exist instead of $T^p_{m-1,n}$ and $T^p_{m-1,n+1}$ respectively. For the Figures 2.7h and 2.7i, the equations can be written similarly.

With the surface heat flux q'' due to the heater element on the surface of the glass block, the energy balance equation for the Figure 2.7j is

$$-k\Delta y\frac{T^p_{m,n} - T^p_{m,n+1}}{\Delta x} - k\frac{\Delta x}{2}\frac{T^p_{m,n} - T^p_{m-1,n}}{\Delta y} - k\frac{\Delta x}{2}\frac{T^p_{m,n} - T^p_{m+1,n}}{\Delta y} + q''\Delta y$$

$$= \rho c\frac{\Delta x}{2}\Delta y\frac{T^{p+1}_{m,n} - T^p_{m,n}}{\Delta t} + h_H\Delta y(T^p_{m,n} - T_\infty)$$

Rearranging for $T^{p+1}_{m,n}$ gives the Equation (2.30) for $\Delta x = \Delta y$. The heat capacity of the heater element is not considered due to its thickness being very much less than Δx.